Development of Metal Organic Vapor Phase Epitaxy for the Growth of Single Crystal NiO and Its Characterization

by
Teuku Muhammad Roffi

A dissertation
submitted to the Graduate School of Informatics and Engineering
The University of Electro-Communications
in partial fulfillment of the requirements
for the degree of
Doctor of Philosophy
in
Engineering

Tokyo, Japan
September 2016

Development of Metal Organic Vapor Phase Epitaxy for the Growth of Single Crystal NiO and Its Characterization

Examining Committee:

Chairman: Associate Professor Kazuo Uchida
Members: Professor Adarsh Sandhu
Professor Shinji Nozaki
Professor Tsuyoshi Okuno
Professor Yoshinao Mizugaki

Copyright © 2016 Teuku Muhammad Roffi
All rights reserved.

Acknowledgement

I express my gratitude to my supervisors: Assoc. Prof. Kazuo Uchida and Prof. Shinji Nozaki. Their guidance, advice, and support are invaluable in finishing this research project. It has been a great learning experience for me. I also thank the faculties in my doctoral examination committee: Professor Adarsh Sandhu, Professor Tsuyoshi Okuno, and Professor Yoshinao Mizugaki.

Special thanks go to the students in Nozaki and Uchida laboratory in the University of Electro-Communications Tokyo. Particularly I would like to thank Zhang and David for the fruitful discussions, the seniors Yoshida-san, Phuc-san, Koike-san, and Nakamura-san for teaching me the know-how in doing experiments. I am also thankful to Anil, Iijima, Kanaya, Ookawa, Kobayashi, Yanagiya, Aihara and Kondou for their helps in experiments and for being good discussion partners. I would like to say thanks to the secretaries in the lab: Ms. Wakai, Ms. Nishiyama, and Sanae. All the conference trip documents would have been a big problem without their support.

I would also like to express my gratitude to my seniors and friends from Indonesia who have helped me adapting to the life in Japan. Also to all Japanese language teachers in UEC, staffs of UEC international student office, MIFO volunteer members, and my host families: the Kimura family, the Akaishi family, and the Iyoda family. I highly appreciate their warm welcome and kind support. Without mentioning any specific names, I would like to thank from the bottom of my heart all my friends, on and off-campus, who have made my stay at Chofu highly memorable.

I owe everything to the love and care of my wife, Alissa who has been the greatest partner in happy and difficult times. I am also grateful with the presence of my son, Azhar. His cries, smiles, and laughter has brighten our life.

I am forever thankful to my father, Teuku Zulkifli and my mother, Susi Sutjihati for their unconditional support. Also to my sisters, Icut and Assa for being the best people to grow up with.

Finally, Alhamdulillah. All praise be for Allah.

論文の和文要旨

単結晶 NiO 薄膜用有機金属気相成長法の開発と結晶評価に関する研究

ニッケル酸化物(NiO)の研究はその幅広い応用用途により盛んに研究が行われている。その中でも、特に深紫外領域をカバーする透明電極用途、可変抵抗メモリー応用がこれら研究の中心である。このような NiO の機能性を高める為には、高品質な NiO 薄膜の成長技術の確立が要求される。一方でキャリア輸送や伝導率の制御もデバイスの性能向上の為に必須である。

これより本研究では、高品質で薄膜成長のコントロール性に優れ、さらに量産性も兼ね備える有機金属気相成長法(MOVPE)に着目し、まず初めに NiO 薄膜成長に適した MOVPE 装置の開発に取り掛かり、そして高結晶性 NiO の成膜、不純物ドーピングの機構やその伝導率への影響、結晶構造、その他、デバイス作成に必要な特性を精査した。

開発し酸化物半導体用 MOVPE 装置は横型常圧リアクターである。また上記様々な特性は成長条件を変化させることでそれら相関を精査した。これら代表的な成長条件は気相 O_2/Ni モル分率、成膜基板の種類、成長温度であり、それぞれが異なる影響を結晶性に示し、最適化により、単結晶 NiO 薄膜の成長に成功した。以下にそれら詳細を記す。

先ず始めに、O_2/Ni モル分率の影響である。O_2/Ni モル分率の増加により、X 線回折の半値幅の減少が確認され、結晶性の向上が確認された。これは成長核の発生とグレイン成長が促進されたためと考えられ、AFM 測定からは、O_2/Ni モル分率の増加による結

晶性向上が平坦な表面形成にも貢献していることが明らかになった。また緻密な結晶性の為に、結晶粒界散乱による抵抗の減少が確認され、その結晶性向上は改善された光の透過性でも確認された。

次に、異なる成長基板としては、Al_2O_3(001)、MgO(100)そして MgO(111)を用いた。結果としては Al_2O_3(001)、MgO(100)基板上では、それぞれ単結晶 NiO(111)と NiO(100)が 500℃で成長され、MgO(111)基板上では単結晶 NiO(111)が 600℃で成長された。またすべての基板において、400℃以上の成長温度で原料の熱分解が完全に行われていることが確認できた。しかしそれぞれの基板では最適な成長温度が存在し、これは結晶性と成長速度のトレードオフであることが明らかになった。そして双晶欠陥の形成が基板の選択で抑制できることも明らかになった。すなわち MgO 基板を用いることで Al_2O_3(001) 基板上の NiO 成長で観察される双晶欠陥の抑制ができる。双晶欠陥の成長温度依存性としては、MgO(111)基板上の NiO(111)において、400℃での成長の時のみ双晶欠陥が確認された。ここで Al_2O_3(001)上と NiO(111)上の双晶欠陥を比べた場合、Al_2O_3(001)の本質的な表面原子配列により、同基板上では成長温度に関わらず、双晶欠陥が発生していると考えられる。また一方で Al_2O_3(001)基板上の成長では、結晶性の向上により、伝導率は結晶性の向上で増大し、逆に MgO 基板上の成長では減少する傾向を示した。成長基板に依存した欠陥がキャリア発生と伝導率に影響を与えていると考えられる。

最後に、不純物ドーピングに関しては、コバルト(Co)、鉄(Fe)をドーパントとして NiO MOVPE 成長と同時に行われた。Ni イオンとは価数の異なる Co^{3+}や Fe^{3+}の導入は電

気特性に大きな影響を与え、キャリアの増加が確認された。このキャリアの増加は価数の異なるイオンの導入により発生する欠陥によるキャリア生成であることで説明できた。また Co 濃度の高いサンプルでは n 型伝導性が確認された。　ドーピング濃度が低い場合は結晶性の劣化は観察されなかったが、濃度上昇に伴い NiO 相と CoNiO 相の混相になる傾向を示した。　一方で Fe ドーピングでは、低い Fe 濃度でも抵抗の増大が確認された。また成長モードでも Fe ドーピングにより、NiO のグレイン成長が促進される傾向であり、これより多結晶の NiO 成長に至った。

これらの結果は、今後の NiO 材料、デバイス開発に重要な知見を与えることが明らかである。

Abstract

The development of nickel oxide (NiO) has drawn interests for a wide range of applications, including diode ultraviolet (UV) detectors, UV light emitting devices, biosensors, and thermoelectric device. Recently, it has also been used in the development of transparent conducting oxide (TCO) and resistive random access memory (ReRAM). In order to achieve a functional NiO, a growth technique for high quality NiO film is required. Furthermore, it is also important to achieve control of the carrier transport and conductivity of NiO. In this study, growth of high quality NiO has been established by metal organic vapor phase epitaxy (MOVPE). Doping of NiO has been carried out in an effort to control the carrier transport and conductivity of the films. Cobalt and iron have been used separately to dope NiO and the effects on the materials properties, including the transparency and conductivity have been investigated.

NiO has been grown by a horizontal-reactor MOVPE at atmospheric pressure. The correlation between the growth parameters, structure of materials, and properties has been investigated by modifying the growth parameters, including the precursor ratio (O_2/Ni), type of substrate, and growth temperature. The reactor has been modified accordingly in order to reduce gas phase reaction because of the use of O_2 and to improve the deposition coverage. Optimization of the growth parameters has allowed the growth of single crystalline NiO film.

Doping of NiO by cobalt and iron has been investigated independently. The growth, optical and electrical properties of the film were affected by dopant incorporation. Defect-controlled carrier generation in NiO has been used to explain the difference in film resistivity upon doping by considering the role of heterovalent Co^{3+} and Fe^{3+} ions.

The demonstrated capability of growing a high quality NiO film by MOVPE and attempts to elucidate understanding of doping mechanism and conductivity in NiO in this study should serve as an important base for further development of NiO material and related applications.

Table of Contents

List of Tables

List of Figures

CHAPTER 1

Introduction

1. 1 Background

NiO is a potential material for many applications such as diode ultraviolet detectors pairing with zinc oxide[1], blue-UV light emitting devices[2,3], biosensors [4] and thermoelectric device[5]. Stoichiometric nickel oxide is known to be insulator with resistivity around 10^{11}~10^{13} Ωcm.[6,7] However, nickel oxide normally contains nickel deficient sites in which holes are formed to maintain charge neutrality.[8] Therefore NiO is known to be p-type, wide band-gap semiconducting material with band-gap energy of 3.6 to 4eV.[9]

NiO has been reported as a promising material for resistance random access memory (ReRAM).[10–13] ReRAM is considered to be one of the alternative replacement of the contemporary Flash memory to obtain faster and larger-capacity memory.[14] The mechanism in ReRAM is still an active research topic with the majority proposes the formation of conductive filament as the cause for switching resistance.[10,14] Diffusion of trapped charge carrier[12] and heat generation and dissipation[13] are some of the proposed mechanisms, among others. The conduction mechanism in NiO needs to be further investigated to elucidate its functionality in ReRAM.

The combination of optical transparency and electrical conductivity of NiO has drawn interests for development of transparent conducting oxides (TCO).[15] TCO is widely used in energy-conserving windows, the front electrodes of solar cells and flat panel displays, among other applications. Indium tin oxide (ITO) is currently the most widely used material for TCO

market which is growing rapidly.[16] However, further expansion is prevented by limited availability of indium. The abundance of NiO in the earth crust together with the aforementioned optical transparency and electrical conductivity makes NiO a promising material for TCO application. Furthermore, as most oxides exhibit n-type conductivity, the development NiO as a p-type oxide will be advantageous for transparent electronics applications i.e. transparent oxide semiconductors.

1. 2 Objectives and overview of thesis

In order to achieve a functional NiO, a growth technique for high quality NiO film is required. Metal organic vapor phase epitaxy (MOVPE) is considered to be one of the best techniques for this purpose mainly due to the capability of growing high quality films and abrupt interface as proven in the optoelectronics industry. It has the advantages of epitaxy of mismatched materials and heterostructures along with high scalability into high throughput industrial level production. Compared to other conventional growth methods such as sputtering and pulsed laser deposition, films grown by MOVPE achieve better crystallinity because no defects are introduced by high energy plasma or laser. In comparison to MBE which often yield similar crystal quality, MOVPE is simpler and more cost efficient. One of the main objective in this study is to establish the growth of NiO by MOVPE. The correlation of growth parameters, structure of materials, and properties is investigated. Chapter 4 focuses on the effects of the precursor ratio (O_2/Ni) during the growth to the films' properties. Experimental result of growth and characterization is presented to describe the correlation between precursor ratio to the conductivity and optical transparency. It is especially important since point defects is an important factor in NiO. In chapter 5, NiO growth on various substrates in different temperature is presented. Single crystalline NiO is obtained by careful selection of substrate and optimization of growth temperature. The characterization of the obtained film correlates the effects of type of substrate and growth temperature to the structure and properties of the film.

It is also important to be able to control the carrier transport and conductivity of the films. This could be achieved by doping. Lithium is a well-known dopant for p-type NiO. Nickel substitution of lithium requires generation of holes for charge neutrality. Other than lithium, suitable dopant for NiO is not well studied. The objective of this study includes the attempt of

NiO doping by cobalt and iron. Cobalt and iron both can be ionized as 2+ and 3+ ions. It is expected that the heterovalent ion can affect carrier generation in NiO and alter the electrical property of the film. Chapter 6 describes the doping and alloying of NiO by cobalt. Experimental results on the growth and characterization are presented. It is found that cobalt doping decreases resistivity of NiO and films with high cobalt concentration possess n-type conductivity. Chapter 7 presents iron doping of NiO. The results show that iron inhibits growth of single crystalline NiO and increases the film resistivity. Here, the effects of different substrate materials are also discussed.

Following this introduction is chapter 2, which consists of background knowledge related to thin film growth by MOVPE and the formation and properties of NiO. Chapter 3 contains brief description on the MOVPE system and some XRD techniques employed in this study. Chapter 4 presents the effects of O_2/Ni ratio on the film properties. MOVPE growth and characterization of single-crystalline NiO are presented in chapter 5. Chapter 6 and 7 contains experimental result on the growth and characterization of NiO doping by cobalt and iron, respectively. Final summary and the scope of future work are presented in chapter 8.

References

[1] H. Ohta, M. Hirano, K. Nakahara, H. Maruta, T. Tanabe, M. Kamiya, T. Kamiya, and H. Hosono, Applied Physics Letters **83**, 1029 (2003).

[2] Y. Xi, Y. Hsu, A. Djuri\vsi'c, A. Ng, W. Chan, H. Tam, and K. Cheah, Applied Physics Letters **92**, 113505 (2008).

[3] B.O. Jung, Y.H. Kwon, D.J. Seo, D.S. Lee, and H.K. Cho, J. Cryst. Growth **370**, 314 (2013).

[4] M. Tyagi, M. Tomar, and V. Gupta, Anal. Chim. Acta **726**, 93 (2012).

[5] S. Liu, J. Jia, J. Wang, S. Liu, X. Wang, H. Song, and X. Hu, Journal of Magnetism and Magnetic Materials **324**, 2070 (2012).

[6] T. Dutta, P. Gupta, A. Gupta, and J. Narayan, J. Phys. D. Appl. Phys. **43**, 105301 (2010).

[7] M. Tyagi, M. Tomar, and V. Gupta, Journal of Materials Research **28**, 723 (2013).

[8] H. Rooksby and M. Vernon, British Journal of Applied Physics **17**, 1227 (1966).

[9] F. Parmigiani and L. Sangaletti, J. Electron Spectros. Relat. Phenomena **98**, 287 (1999).

[10] U. Russo, D. Ielmini, C. Cagli, and A.L. Lacaita, Electron Devices, IEEE Transactions on **56**, 186 (2009).

[11] C. Lee, B. Kang, A. Benayad, M. Lee, S.-E. Ahn, K. Kim, G. Stefanovich, Y. Park, and I. Yoo, Applied Physics Letters **93**, 042115 (2008).

[12] S. Das, S. Majumdar, and S. Giri, Physics Letters A **374**, 4559 (2010).

[13] H. Wu, K. Cai, J. Zhou, B. Li, and L. Li, PLoS One **8**, e79832 (2013).

[14] A. Sawa, Materials Today **11**, 28 (2008).

[15] H. Sato, T. Minami, S. Takata, and T. Yamada, Thin Solid Films **236**, 27 (1993).

[16] D.S. Ginley and C. Bright, Mrs Bulletin **25**, 15 (2000).

CHAPTER 2

Related background knowledge

2. 1 Crystal growth

2. 1. 1 Thin film epitaxy

The epitaxy of thin films consists of several growth stages, namely nucleation, grain growth, coalescence, and thickness growth.[1] The nucleation is a process by which a seed crystal is born and grows into a nucleus. This is a comparatively slower process as the atoms need to impinge on each other in the right orientation. Considering the particles involved in the process, nucleation can be classified as homogeneous and heterogeneous nucleation. In homogeneous nucleation, no foreign particle is involved and therefore it needs to create its own surface and meet the required surface energy. In heterogeneous nucleation, foreign particles act as scaffold for crystal to grow on. The nucleation is followed by grain growth: an outward spread growth of crystal from the nucleating point. These grains impinge on each other and coalesce to form a larger grain. This type of coalescence is due to the size increase of the grains and is known as the growth coalescence. Coalescence can also be caused by mobility of nuclei which is known as mobility coalescence.[2] Figure 2.1 illustrates the process of crystal growth.

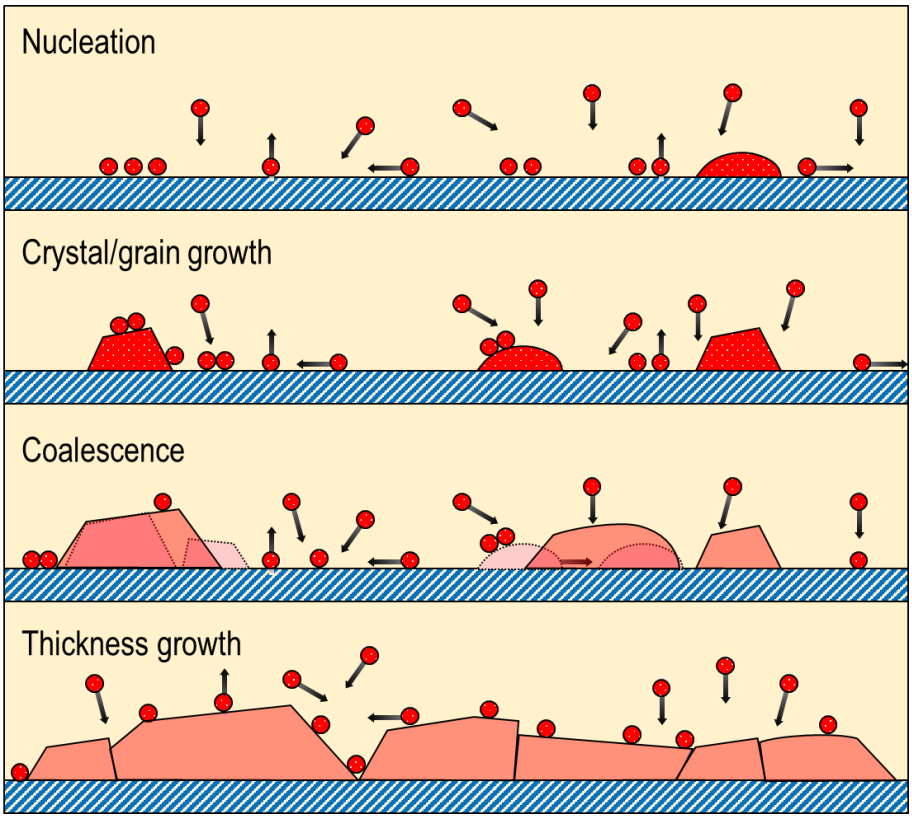

Figure 2.1 Schematic illustration of the steps in crystal growth. Dotted line indicates the grain prior to coalescence.

2. 1. 2 Growth modes

Heteroepitaxy is the term used for epitaxy in which the material of the crystalline film differs to that of the substrate. There are three growth modes commonly used to describe the growth in heteroepitaxy.[1,3] The Frank-van der Merwe (FM) is a layer by layer growth mode which results in the smoothest surface as each new monolayer starts growing only after the previous monolayer is completed. The Volmer-Weber (VW) is a growth of crystalline film by formation of three-dimensional islands which then nucleates all over the substrate. The Stranski-Krastanov (SK) is a growth mode in which monolayers are initially formed, followed by formation of three-dimensional clusters. The three growth modes are illustrated in Figure 2.2.

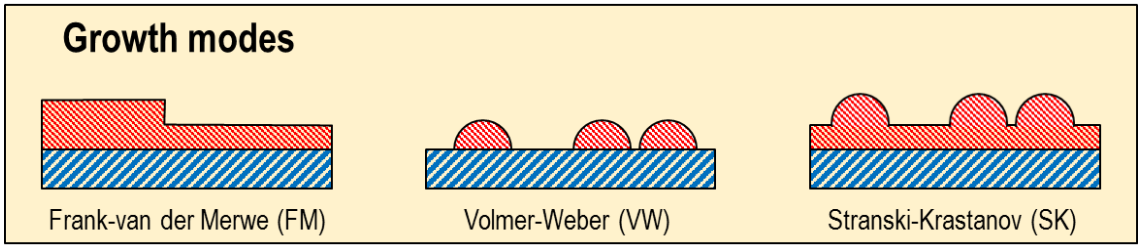

Figure 2.2 Schematic illustration of the growth modes in heteroepitaxy.

The FM mode is expected when the film to substrate interaction is stronger than the film to film interaction. Conversely, VW mode is expected when the film to substrate interaction is weaker than the film to film interaction. The SK mode is highly related to the presence of misfit. In SK mode, the stronger film to substrate interaction compared to film to film interaction dominates the initial growth. With the growth of successive monolayer, the strain energy due to mismatch is accumulated. It then provides the driving energy for nucleation of three-dimensional islands.

2. 1. 3 Growth rate in MOVPE

Details of the growth in MOVPE is given in Section 1 of Chapter 2. Here, description of the limiting factors of the growth rate in MOVPE is given. Growth rate in MOVPE can be limited by the mass transfer or by the reaction rate.

In order to understand the limiting factors of the growth rate by MOVPE, the diffusion of reactant and the surface reaction are considered.[4] First, the reactant flows from the gas-phase into the substrate. The flux of which is represented by F_1 (molecules cm^{-2} s^{-1}). F_1 depends on the mass transfer coefficient and the difference in reactant concentration as shown in the following equation.

$$F_1 = h_G(C_G - C_S)$$

h_G denotes the mass transfer coefficient (cm s^{-1}) while C_G and C_S denote the reactants concentration at gas flow and substrate surface (molecule cm^{-3}), respectively.

Second, on the surface of the substrate, the reactant is consumed by the surface reaction. The flux of which is represented by F_2. It depends on the chemical surface reaction rate, with k_S denoting the chemical surface reaction rate (cm/s) as follows.

$$F_2 = k_S C_S$$

Assuming a steady state condition, the flux of reactant coming from gas-phase to the substrate surface is the same as the flux of reactant consumed by the surface reaction.

$$F = F_1 = F_2$$

$$h_G(C_G - C_S) = k_S C_S$$

$$C_S = \frac{h_G C_G}{h_G + k_S}$$

Substituting C_S in F_2:

$$F = \frac{k_S h_G}{h_G + k_S} C_G$$

We obtain the deposition rate, v (cm s^{-1}), which is defined as:

$$v = \frac{F}{N} = \frac{k_S h_G}{h_G + k_S} \frac{C_G}{N}$$

N is the number of atoms incorporated per unit volume in the film, film density (molecules cm^{-3}).

Using Y as fraction of incorporating species in gas phase and C_T as concentration of all molecules in gas phase:

$$Y \equiv \frac{C_G}{C_T}$$

$$v = \frac{k_S h_G}{h_G + k_S} \frac{Y C_T}{N}$$

In the case where $k_S \ll h_G$, the reaction rate is slow with a fast mass transfer. The growth rate is determined by the chemical reaction rate:

$$v \cong k_S \frac{Y C_T}{N}$$

This is commonly referred to as a reaction controlled or kinetically limited growth.

In the case where $k_S \gg h_G$, the reaction rate is fast with a slow mass transfer. The growth rate is determined by the mass transfer rate:

$$v \cong h_G \frac{Y C_T}{N}$$

This is commonly referred to as a diffusion controlled or transport limited growth. The two conditions of the kinetically limited and the transport limited growth rate is depicted in Figure 2.3.

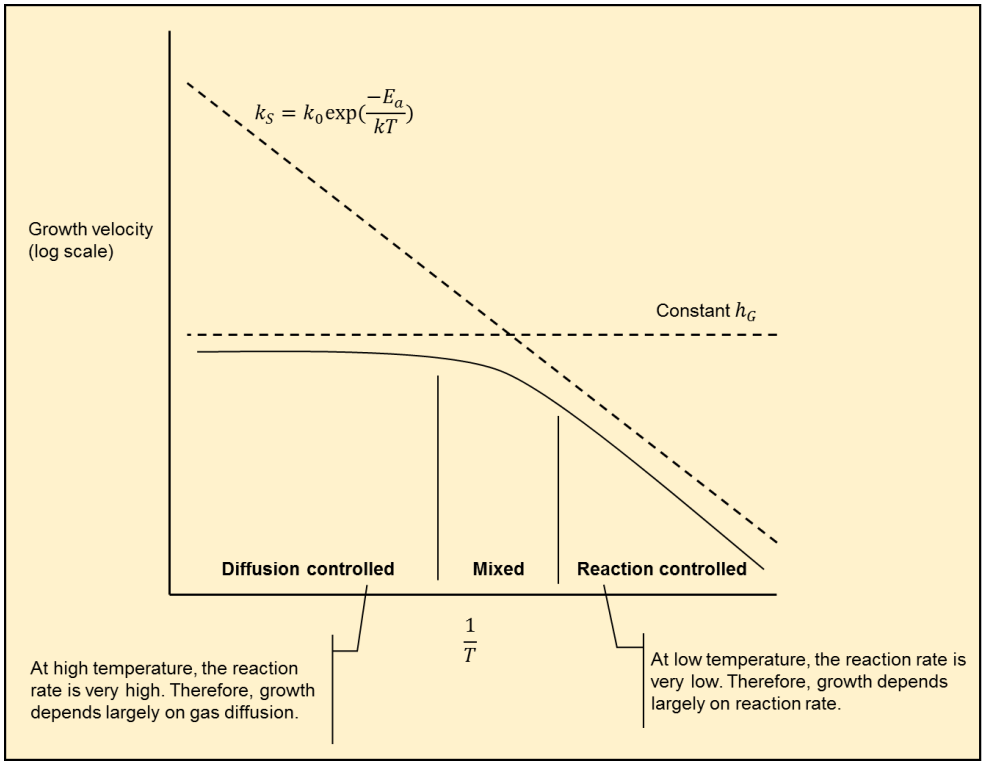

Figure 2.3 Deposition rate dependence on surface reaction and gas diffusion

In MOVPE, the growth rate falls with the length of substrate. In other words, the farther the substrate from gas flow source, the lower the growth rate. This is caused by gas velocity/boundary layer and source gas depletion variation on substrate position.

Remind the amount of gas flux flowing from main gas flow to substrate surface through boundary layer:

$$F_1 = h_G(C_G - C_S)$$

Now, from Fick's 1st law of diffusion which postulates that the flux goes from regions of high concentration to regions of low concentration, with a magnitude that is proportional to the concentration gradient (spatial derivative).

$$F_1 = -D_G \frac{\partial C}{\partial x} = \frac{D_G}{\delta S}(C_G - C_S)$$

From above two equations we get

$$h_G = \frac{D_G}{\delta S}$$

where h_G is the mass transfer coefficient in cm s^{-1}, D_G is the diffusion coefficient of the reacting species across the boundary layer in the gas phase in cm^2 s^{-1}, and δS is the boundary layer in cm.

The boundary layer δS depends on gas velocity and substrate length. This is shown according to Newton's 2nd law.

$$\delta S(x) = \left(\frac{\mu x}{\rho u}\right)^{1/2}$$

Where μ is the gas viscosity in kg m^{-1} s^{-1}, x is the substrate length from initial gas flow in cm, ρ is the gas density in kg m^{-3} and u is the gas flow velocity in cm s^{-1}. As illustrated in Figure 2.4, as the substrate gets farther from gas source, the gas velocity near the substrate drops thus increasing the boundary layer. The increase of boundary layer decreases h_G. Therefore the deposition rate at front side is higher than in back side (farther side).

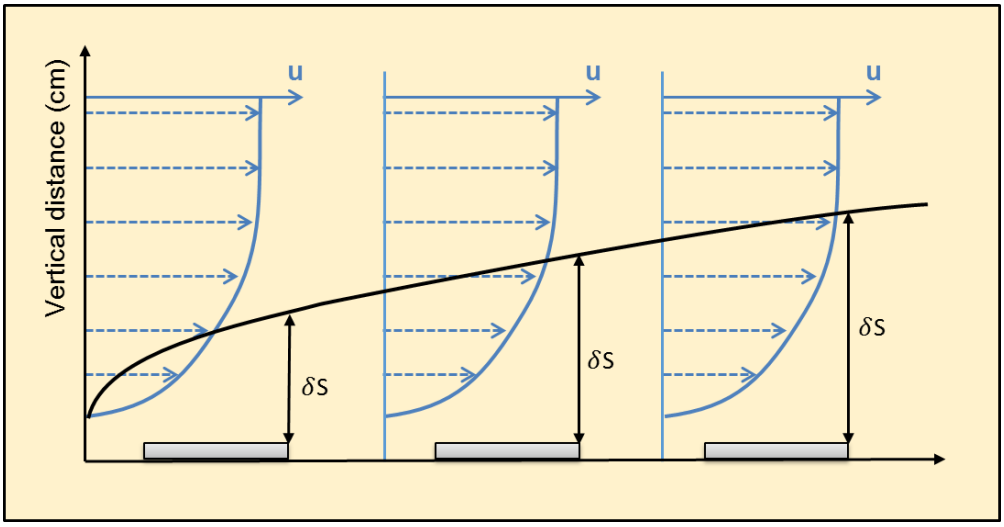

Figure 2.4 Boundary layer velocities along susceptor. The boundary layer increases with distance.

Additionally, the source gas depletion occurs along the length of substrate because they are consumed along the substrate, therefore the concentration, Y, decreases and so does the deposition rate.

$$\mathrm{v} = \frac{k_S h_G}{h_G + k_S} \frac{Y C_T}{N}$$

Several strategies may be used to minimize the non-uniformity of the growth:

- Tilting the substrate. This will decrease cross sectional area of substrate, increase gas flow rate, and decrease boundary layer.
- Put higher temperature in the farther part of substrate. This can compensate the decrease of concentration in the farther part of the substrate.
- Downward gas flow with substrate rotated horizontally. This will provide uniform gas velocity and concentration throughout the substrate.

2. 1. 4 Domain matching epitaxy (DME)

In the conventional lattice-matching epitaxy, films grow pseudomorphically up to a certain critical thickness where film-substrate lattice constants misfits are small (7%-8%). It involves

matching of the same planes between the film and the substrate. The misfit strain is relaxed with the introduction of dislocations beyond the critical thickness during film growth.

$$\varepsilon = \frac{a_f}{a_s} - 1 \qquad | \qquad a_{f,s}: lattice\ constant\ of\ the\ film, subtrate$$

The DME is a framework which allows epitaxy by matching of integral multiples of lattice constants at the film-substrate interface.[5] The film and substrate planes could be very different as long as they satisfy the crystal symmetry. The initial misfit strain is given by

$$\varepsilon = \frac{d_f}{d_s} - 1 \qquad | \qquad d_{f,s}: interplanar\ spacing\ of\ the\ film, subtrate$$

The DME framework allows large initial misfit strain which then can be relaxed by matching of m planes of the film with n planes of the substrate. This matching of planes results in the residual strain ε_r.

$$\varepsilon_r = \frac{md_f}{nd_s} - 1 \qquad | \qquad m, n: integers$$

In the ideal case where m planes of the film match exactly to n planes of substrate, the residual strain is zero. If otherwise, the residual strain is finite, then two domains alternate with a certain frequency for a perfect matching according to

$$(m + \alpha)d_f = (n + \alpha)d_s \qquad | \qquad \alpha: frequency\ factor$$

For example if $\alpha = 0.5$ then m/n and (m+1)/(n+1) domains alternate with an equal frequency.

For $d_f > d_s$, $m < n$ so that the difference between m and n could be 1 or a function of m.

$$n - m = 1\ or\ n - m = f(m)$$

The derivation of relation between m and ε is as follows.

$$(m+\alpha)d_f = (n+\alpha)d_s$$

Substituting $n\ for\ m+1\ or\ n\ for\ m+f(m)$, we obtain

$$(m+\alpha)d_f = (m+1+\alpha)d_s$$
$$(m+\alpha)(\varepsilon+1) = (m+1+\alpha)$$
$$(m+\alpha)\varepsilon + (m+\alpha) = (m+1+\alpha)$$
$$(m+\alpha)\ \varepsilon = 1\ for\ n = m+1\ or$$
$$(m+\alpha)\ \varepsilon = f(m)\ for\ n = m+f(m)$$

Accordingly for $d_f < d_s$, $m > n$ so that the difference between m and n could be 1 or a function of m.

$$n - m = -1\ or\ n - m = -f(m)$$
$$(m+\alpha)\ \varepsilon = -1\ and\ n = m-1\ or$$
$$(m+\alpha)\ \varepsilon = -f(m)\ and\ n = m - f(m)$$

2. 2 Nickel oxide

2. 2. 1 Film formation and structure

At ambient temperature and pressure, nickel oxide is stable as nickel oxide (NiO) in the cubic rock salt structure with lattice parameter a=4.1771Å (PDF #47-1049). An atomic model of the cubic NiO generated by using Vesta[6] is shown in Figure 2.5. Other form of nickel oxide, dinickel trioxide (Ni_2O_3) is rarely reported[7–9] and not established. Besides the cubic structure, rhombohedral structure of NiO were also reported.[10,11] However, because the interplanar spacing of the rhombohedral NiO (PDF #44-1159) is highly similar to that of the cubic NiO, it is not distinguishable by XRD measurement. The existence of rhombohedral NiO is also argued as formation of twin structure of the cubic NiO, which is frequently reported, may exhibit a similar structure to that of the rhombohedral.[12,13]

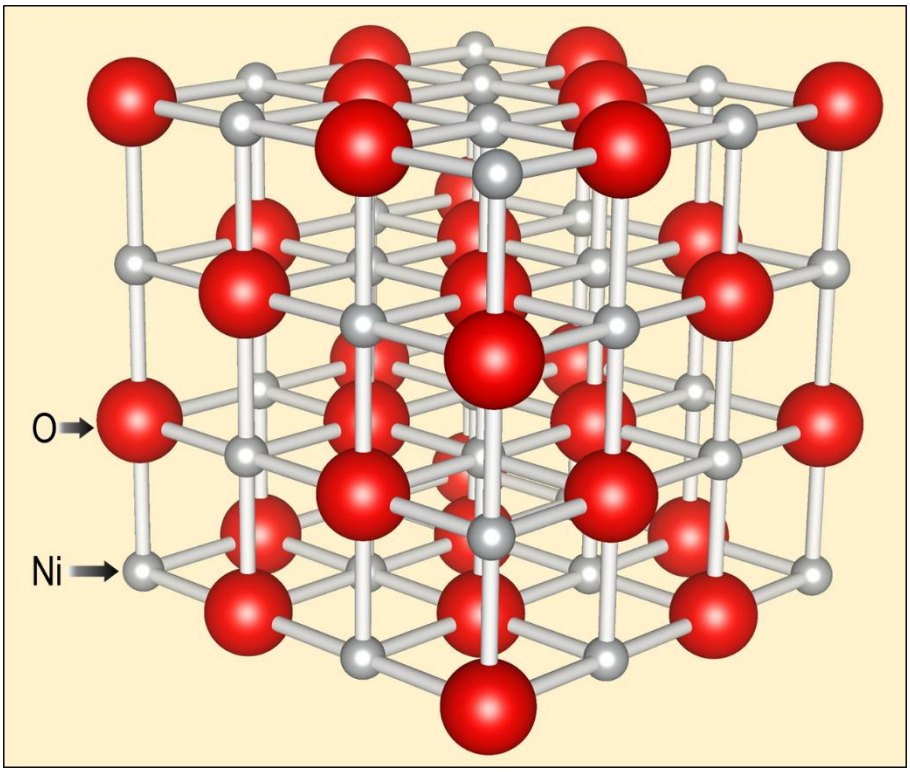

Figure 2.5 Schematic illustration of cubic NiO

NiO has been grown using various methods on many substrates. It has been grown by sputtering,[14–20] pulsed laser deposition,[13,21–23] MOVPE,[24–28] sol-gel,[29] molecular beam epitaxy,[30] atomic layer deposition,[31] and UV-oxidation.[32] Glass, Al_2O_3, and MgO were the most commonly used substrates in the growth of NiO. The growth of NiO has been limited to the formation of polycrystalline NiO on glass substrates[15,16,24,33] and single-crystalline NiO with twin defects on Al_2O_3 substrates.[24,27,34] Few studies have reported the growth of single-crystalline NiO[35] or described the effects of the crystal structure on the film properties.[22]

2. 2. 2 Properties

The electrical and optical properties of NiO has been investigated for more than half a century. The bandgap of NiO was optically determined to be 4 eV based on the absorption spectrum[36] and photo emission and inverse photo emission spectrum.[37] The bandgap of around 3.7 eV has been confirmed by recent reports based on the transmittance spectra.[14,15,25,28,38] It is noted that information of the crystal structure was not included in the early works of NiO and thus correlation between the crystal structure and film properties was not established.

Although stoichiometric NiO is an insulator (10^{13} Ωcm), [39,40] Ni deficiency is commonly found in the grown films. The nickel vacancy is compensated by generation of electron holes for charge neutrality and therefore results in p-type conductivity.[41] In Kröger-Vink Notation, oxidized p-type and cation deficiency on lattice sites i.e. Oxygen (gas) comes creating oxygen atom in lattice sites with Ni vacancy and 2 holes.

$$\frac{1}{2}O_2\ (g) \Leftrightarrow v''_{Ni} + O_o^{\mathrm{X}} + 2h^{\cdot}$$

The transport mechanism in NiO, however, is still an active research topic. It is commonly accepted that the conduction is based on the polaron transport. Polaron is phenomenological model, electron-phonon interaction in which the electron polarizes the medium. The medium then deforms and trap the electrons.[42] It is the case for ionic or highly polar crystals due to the existence of coulomb interaction between conduction electron and the lattice ions causing strong electron-phonon coupling. In covalently bonded semiconductors (group IV or III-V) atoms in the lattice are considered frozen. Discussion on the polaron conduction in NiO is divided into large and small polaron hopping. In large polaron hopping, the mobility is large and decreases with temperature while in small polaron hopping the mobility is small and shows activated temperature dependence.[43] Reported mobility values for large polaron hopping were 35 $cm^2V^{-1}s^{-1}$ (RT) and 15 $cm^2V^{-1}s^{-1}$ (172K),[44] and less than 10 $cm^2V^{-1}s^{-1}$ in lithium doped NiO.[45] For small polaron hopping, the reported values were 10^{-5} $cm^2V^{-1}s^{-1}$ (1000K) and 10^{-8} $cm^2V^{-1}s^{-1}$ (300K).[46] More recently published reports tend to agree to the small polaron hopping theory with mobility values in the range of 0.03 to 7.4 $cm^2V^{-1}s^{-1}$ depending on the material preparation.[11,14,34,47–50] The type of conductivity is, however, differs as n-type conductivity was also reported for NiO.[47,51,52]

2. 3 Kröger-Vink Notation

The Kröger-Vink notation is used to describe the defect reaction in a compound, i.e. the metal oxides including the electric charge and lattice position of point defects.[53] The notation becomes important since the property of metal oxides is often controlled by the defect structure. The basic construction of the Kröger-Vink notation is shown in Table 2.1.

Table 2.1 Basic structure in the Kröger-Vink notation

M_S^C	
M	Represents the species It can be one of the following: - Atom (by the element name) - Vacancies (v) - Interstitials (i) - Electrons (e) - Electron holes (h)
S	Represents the site of the lattice It can be one of the following: - Atom (by the element name) - Interstice (i) - Cation (C) or metal (M) → ion with positive charge - Anion (A) or (X) → negatively charged ion
C :	Represent the effective charge: Electronic charge of the species relative to the site it occupies. Effective charge = current species charge-original species charge The symbols used is as follows: - Null is represented by X - Positive charge is represented by: · - Negative charge is represented by: ′
Example Provided $Ni^{2+}, Cu^{2+}, Cl^{1-}, O^{2-}$ Ni_{Cu}^{x} represents nickel on copper site with neutral charge V_{Cl}' represents chlorine vacancy with single positive charge O_i'' represents oxygen interstitial with double negative charge	

There are three principles in constructing a defect reactions.[53] Analogous to reactions in aqueous solutions, charge and mass conservation is required. Additionally for defect reactions in crystalline compounds, it is required to conserve the ratio of structure sites. Conservation of mass

or the mass balance states that the number and types of atoms involved before and after the reaction must be the same. Vacancies and electronic charges are not considered in the mass balance. Conservation of charge or electroneutrality states that the total (effective) charges must be the same before and after reactions. Conservation of ratio of structure sites states that the ratio of number of anion and cation sites in a crystalline compound is constant. There may be a change in the total number of structure sites due to formation or annihilation but the ratio must always be equal to the ideal structure.

For instance, in the creation of Nickel vacancy commonly found in NiO, reaction with oxygen gas creates a new oxygen structure in the lattice with zero effective charge. To conserve ratio of structure sites, additional nickel sites with two negative charges are formed. In order to conserve electroneutrality, two electron holes are generated. The notation is as follows.

$$\frac{1}{2}O_2\ (g) \Leftrightarrow v''_{Ni} + O_o^{\mathrm{X}} + 2h^{\cdot}$$

Here, the total number of O atoms both before and after the reaction are the same: 1 atom. The total charge before the reaction is 0, the same as that after the reaction. The -2 of the nickel vacancy is compensated by +2 from the electron holes. The site ratio of ideal NiO is 1 Ni to 1 O, here the site of Ni is 1 (v''_{Ni}) and O is also 1 (O_o^{X}).

Defects can be found in either stoichiometric compounds or the nonstoichiometric compounds. Schottky and Frenkel defects are defect structures in a stoichiometric compounds. Schottky defect is point defect in a crystal where the same amount of cation and anion are missing from the lattice as shown in Figure 2.6. The electrical and stoichiometry composition is maintained. It occurs only when there is a small difference in size of cations and anions. Since

there are cations and anions missing (in the same amount), the density is less than that of the normal crystal. It is represented in Kröger-Vink notation as follows.

$$A_A^X + C_C^X \Leftrightarrow v_A^{'} + v_C^{\cdot} + A_A^X + C_C^X$$

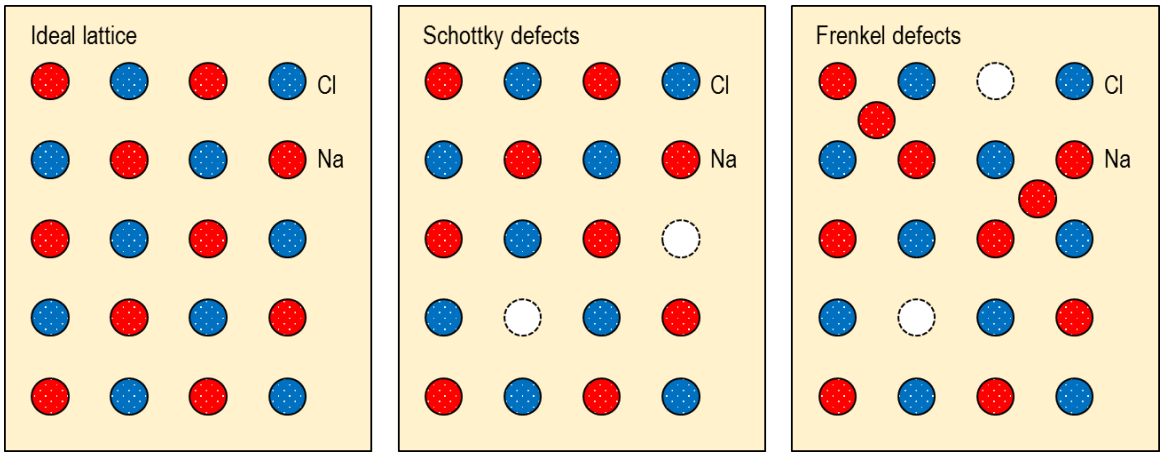

Figure 2.6 Illustration of an ideal lattice, lattice with Schottky defects, and lattice with Frenkel defects.

Frenkel defect is a type of defect in which an atom is displaced from its lattice to interstitial site, creating a vacancy at original site and an interstitial defect in the new location. It usually occurs in compound with large size difference between anion and cation (cation usually smaller). Since it involves only migration of atoms in the crystal, there is no effect on density. It is represented in Kröger-Vink notation as follows.

Cation Frenkel defect

$$C_C^X + v_i^X \Leftrightarrow v_C^{'} + C_i^{\cdot}$$

Anion Frenkel defect

$$A_A^X + v_i^X \Leftrightarrow v_A^{\cdot} + A_i^{'}$$

Many of the oxides, however, deviates from stoichiometry. It is common to find oxides with metal deficiency, such as the NiO and FeO. The defect structures involving point defects in nonstoichiometric oxides can be divided into four groups as shown in Table 2.2. It includes the

case of excess or deficit in either cations or anions. If the predominating defect is charged, electronic defect of the opposite effective charge is created in order to conserve electrical neutrality. The cases of oxygen deficient, metal excess, oxygen excess, and metal deficient oxides are explained as follows.

Table 2.2 Defect formation in nonstoichiometric oxides

<table>
<tr><td rowspan="2">Donor (n-type)</td><td>Oxygen deficient oxide (MO_{1-y})
Oxygen vacancy is formed by transfer of oxygen atom of a normal site to the gaseous state (no change in number of structure site). Assuming the oxygen vacancy is neutral (two electrons left by O^{2-} ion stayed in the vacancy site), the defect reaction is as follows.
$$O_0^{\mathrm{X}} \Leftrightarrow v_0^{\mathrm{x}} + \frac{1}{2}O_2\ (g)$$
The two electrons may be excited and transferred away as such the vacancy acts as donor and may become singly or doubly charged depending on temperature and vacancy concentration. However in high temperature the ionization is usually complete.
$$O_0^{\mathrm{X}} \Leftrightarrow v_0^{\cdot\cdot} + 2e' + \frac{1}{2}O_2\ (g)$$
In the case of electrons localized at a metal ion on a normal structure site instead of at the conduction band, the reaction can be reformulated as follows.
$$O_0^{\mathrm{X}} + M_M^{\mathrm{X}} \Leftrightarrow v_0^{\cdot\cdot} + M_M'' + \frac{1}{2}O_2\ (g)$$</td></tr>
<tr><td>Metal excess oxides ($M_{1+x}O$)
This may alternatively equivalent to oxygen deficient oxides, but the predominant defects constitute of interstitial atoms. As a metal site is annihilated, an oxygen site must also be annihilated by transferring two oxygen atoms to the gas phase.
$$O_0^{\mathrm{X}} + M_M^{\mathrm{X}} + v_i^{\mathrm{X}} \Leftrightarrow M_i^{\cdot\cdot} + 2e' + \frac{1}{2}O_2\ (g)$$
Besides oxygen exchange to surrounding environment, metal interstitials can also be formed in equilibrium with the metal vapor.
$$M(g) + v_i^{\mathrm{X}} \Leftrightarrow M_i^{\cdot\cdot} + 2e'$$</td></tr>
</table>

Acceptor (p-type)	Oxygen excess oxides (MO_{1+y}) The predominating point defects are interstitial oxygen atoms or ions through reaction with oxygen. (no new structure sites are formed). $$\frac{1}{2}O_2\ (g) + v_i^X \Leftrightarrow O_i'' + 2h^{\cdot}$$
	Metal deficient oxides ($M_{1-x}O$) The predominating point defects are metal vacancies through reaction with oxygen gas. This creates new structure sites of oxygen and vacant metal sites. $$\frac{1}{2}O_2\ (g) \Leftrightarrow v_M'' + O_0^X + 2h^{\cdot}$$ The electron holes can also be expressed as a valence defect in which M+2 becomes M+3. $$\frac{1}{2}O_2\ (g) \Leftrightarrow v_M'' + O_0^X + 2M_M^{\cdot}$$

When a reaction involves foreign elements such as in the case of doping, different types of defect structures may occur depending on the valency of impurity species. Some cases of dissolution of foreign elements in given below:

1. Aliovalent oxides in metal deficient oxide $M_{1-x}O$ (p-type)
   Predominating defects are charged metal vacancies compensated by electrons holes→ p-type

Additional oxide	Compensating methods
Higher valency oxides (Mh_2O_3) Mh^{3+} will occupy M sites with 1 positive effective charge: $Mh_M^{\cdot}$	Formation of negatively charged metal vacancy $$Mh_2O_3 \Leftrightarrow 2Mh_M^{\cdot} + v_M'' + 3O_0^X$$
	Annihilation of existing holes $$Mh_2O_3 + 2h^{\cdot} \Leftrightarrow 2Mh_M^{\cdot} + 2O_0^X + \frac{1}{2}O_2\ (g)$$
	Result: Dissolution of Mh_2O_3 increases the concentration of metal vacancies in the parent oxide and decreases the concentration of electron holes
	Formation of holes $$Ml_2\ O + \frac{1}{2}O_2\ (g) \Leftrightarrow 2Ml_M' + 2O_0^X + 2h^{\cdot}$$

Lower valency oxides (Ml_2O) Ml^{1+} will occupy M sites with 1 negative effective charge: Ml'_M	Annihilation of negatively charged metal vacancy $$Ml_2\ O + v''_M \Leftrightarrow 2Ml'_M + O_0^X$$
	Result: Dissolution of Ml_2O decreases the concentration of metal vacancies in the parent oxide and increases the concentration of electron holes

2. Aliovalent oxides in oxygen deficient oxide MO_{2-y} (n-type)

Predominating defects are oxygen vacancies compensated by defect electrons → n-type

Additional oxide	Compensating methods
Higher valency oxides (Mh_2O_5) Mh^{5+} will occupy M sites with 1 positive effective charge: $Mh^{\cdot}_M$	Formation of electrons $$Mh_2O_5 \Leftrightarrow 2Mh^{\cdot}_M + 2e' + 4O_0^X + \frac{1}{2}O_2\ (g)$$
	Annihilation of positive effective charges (oxygen vacancies) $$Mh_2O_5 + v_0^{\cdot\cdot} \Leftrightarrow 2Mh^{\cdot}_M + 5O_0^X$$
	Result: Dissolution of Mh_2O_5 increases the concentration of electrons and decreases the concentration of oxygen vacancies
Lower valency oxides (Ml_2O_3) Ml^{3+} will occupy M sites with 1 negative effective charge: Ml'_M	Formation of positive effective charges (oxygen vacancies) $$Ml_2O_3 \Leftrightarrow 2Ml'_M + v_0^{\cdot\cdot} + 3O_0^X$$
	Annihilation of electrons $$Ml_2O_3 + 2e' + \frac{1}{2}O_2\ (g) \Leftrightarrow 2Ml'_M + 4O_0^X$$
	Result: Dissolution of Ml_2O_3 decreases the concentration of electrons and increases the concentration of oxygen vacancies

References

[1] P.B. Barna and M. Adamik, Science and Technology of Thin Films 1 (1995).

[2] J. Robins, Thin Solid Films **32**, 151 (1976).

[3] J. Venables, *Introduction to Surface and Thin Film Processes* (Cambridge University Press, 2000).

[4] J. Plummer, M. Deal, and P. Griffin, *Silicon VLSI Technology* (Prentice Hall, 2000).

[5] J. Narayan and B. Larson, Journal of Applied Physics **93**, 278 (2003).

[6] K. Momma and F. Izumi, Journal of Applied Crystallography **44**, 1272 (2011).

[7] P. Aggarwal and A. Goswami, The Journal of Physical Chemistry **65**, 2105 (1961).

[8] B. Sasi, K. Gopchandran, P. Manoj, P. Koshy, P.P. Rao, and V. Vaidyan, Vacuum **68**, 149 (2002).

[9] L. Li, K.S. Hui, K. Hui, H. Park, D. Hwang, S. Cho, S. Lee, P. Song, Y. Cho, H. Lee, and others, Materials Letters **68**, 283 (2012).

[10] S.Z. Khan, Y. Yuan, A. Abdolvand, M. Schmidt, P. Crouse, L. Li, Z. Liu, M. Sharp, and K. Watkins, Journal of Nanoparticle Research **11**, 1421 (2009).

[11] J.H. Lee, Y.H. Kwon, B.H. Kong, J.Y. Lee, and H.K. Cho, Cryst. Growth Des. **12**, 2495 (2012).

[12] K. Uchida, K. Yoshida, D. Zhang, A. Koizumi, and S. Nozaki, AIP Advances **2**, 042154 (2012).

[13] R. Yamauchi, Y. Hamasaki, T. Shibuya, A. Saito, N. Tsuchimine, K. Koyama, A. Matsuda, and M. Yoshimoto, Sci. Rep. **5**, (2015).

[14] J.-H. Oh, S.Y. Hwang, Y.D. Kim, J.-H. Song, and T.-Y. Seong, Materials Science in Semiconductor Processing **16**, 1346 (2013).

[15] B. Subramanian, M.M. Ibrahim, V. Senthilkumar, K. Murali, V. Vidhya, C. Sanjeeviraja, and M. Jayachandran, Physica B: Condensed Matter **403**, 4104 (2008).

[16] M. Tyagi, M. Tomar, and V. Gupta, Materials Research Bulletin **66**, 123 (2015).

[17] H. Ryu, G. Choi, W. Lee, and J. Park, Journal of Materials Science **39**, 4375 (2004).

[18] H.-L. Chen, Y.-M. Lu, J.-Y. Wu, and W.-S. Hwang, Materials Transactions **46**, 2530 (2005).

[19] B. Warot, E. Snoeck, P. Baulès, J. Ousset, M. Casanove, S. Dubourg, and J. Bobo, Applied Surface Science **177**, 287 (2001).

[20] G.H. Aydogdu, D. Ruzmetov, and S. Ramanathan, Journal of Applied Physics **108**, 113702 (2010).

[21] R. Molaei, M. Bayati, H. Alipour, S. Nori, and J. Narayan, Journal of Applied Physics **113**, 233708 (2013).

[22] K. Oka, T. Yanagida, K. Nagashima, H. Tanaka, and T. Kawai, Journal of Applied Physics **104**, 013711 (2008).

[23] Y. Kakehi, S. Nakao, K. Satoh, and T. Kusaka, J. Cryst. Growth **237**, 591 (2002).

[24] E. Fujii, A. Tomozawa, H. Torii, and R. Takayama, Jpn. J. Appl. Phys. **35**, L328 (1996).

[25] H. Wang, Y. Zhao, C. Wu, G. Wu, B. Zhang, and G. Du, Optik-International Journal for Light and Electron Optics (2015).

[26] K.-C. Min, M. Kim, Y.-H. You, S. Lee, Y. Lee, T.-M. Chung, C. Kim, J.-H. Hwang, K.-S. An, N.-S. Lee, and others, Surface and Coatings Technology **201**, 9252 (2007).

[27] A. Wang, J.A. Belot, and T.J. Marks, Journal of Materials Research **14**, 1132 (1999).

[28] T.M. Roffi, K. Uchida, and S. Nozaki, J. Cryst. Growth **414**, 123 (2015).

[29] Y. Kokubun, Y. Amano, Y. Meguro, and S. Nakagomi, Thin Solid Films (2015).

[30] C. Mocuta, A. Barbier, G. Renaud, Y. Samson, and M. Noblet, Journal of Magnetism and Magnetic Materials **211**, 283 (2000).

[31] E. Lindahl, J. Lu, M. Ottosson, and J.-O. Carlsson, J. Cryst. Growth **311**, 4082 (2009).

[32] D. Zhang, S. Nozaki, and K. Uchida, Journal of Vacuum Science & Technology B **32**, 031202 (2014).

[33] H.-L. Chen and Y.-S. Yang, Thin Solid Films **516**, 5590 (2008).

[34] H. Wang, G. Wu, X. Cai, Y. Zhao, Z. Shi, J. Wang, X. Xia, X. Dong, B. Zhang, Y. Ma, and others, Vacuum **86**, 2044 (2012).

[35] B. Warot, E. Snoeck, P. Baulès, J. Ousset, M. Casanove, S. Dubourg, and J. Bobo, J. Cryst. Growth **234**, 704 (2002).

[36] R. Powell and W. Spicer, Physical Review B **2**, 2182 (1970).

[37] G. Sawatzky and J. Allen, Physical Review Letters **53**, 2339 (1984).

[38] T. Dutta, P. Gupta, A. Gupta, and J. Narayan, Journal of Applied Physics **108**, 083715 (2010).

[39] M. Tyagi, M. Tomar, and V. Gupta, Journal of Materials Research **28**, 723 (2013).

[40] T. Dutta, P. Gupta, A. Gupta, and J. Narayan, J. Phys. D. Appl. Phys. **43**, 105301 (2010).

[41] H. Rooksby and M. Vernon, British Journal of Applied Physics **17**, 1227 (1966).

[42] S.J. Byrnes, *Basic Theory and Phenomenology of Polarons* (Department of Physics, University of California at Berkeley, Berkeley, CA, 2008).

[43] N. Tsuda, K. Nasu, A. Fujimori, and K. Siratori, *Electronic Conduction in Oxides* (Springer Science & Business Media, 2013), p. 210.

[44] W. Spear and D. Tannhauser, Physical Review B **7**, 831 (1973).

[45] A. Bosman and C. Crevecoeur, Physical Review **144**, 763 (1966).

[46] J. Keem, J. Honig, and L. Van Zandt, Philosophical Magazine B **37**, 537 (1978).

[47] M. Tyagi, M. Tomar, and V. Gupta, Anal. Chim. Acta **726**, 93 (2012).

[48] H. Sato, T. Minami, S. Takata, and T. Yamada, Thin Solid Films **236**, 27 (1993).

[49] H.-L. Chen, Y.-M. Lu, and W.-S. Hwang, Surface and Coatings Technology **198**, 138 (2005).

[50] M. Guziewicz, J. Grochowski, M. Borysiewicz, E. Kaminska, J.Z. Domagala, W. Rzodkiewicz, B.S. Witkowski, K. Golaszewska, R. Kruszka, M. Ekielski, and others, Optica Applicata 431 (2011).

[51] R. Molaei, R. Bayati, and J. Narayan, Cryst. Growth Des. **13**, 5459 (2013).

[52] P. Gupta, T. Dutta, S. Mal, and J. Narayan, Journal of Applied Physics **111**, 013706 (2012).

[53] P. Kofstad and T. Norby, *Defects and Transport in Crystalline Solids* (University of Oslo, Norwegia, 2007).

CHAPTER 3

MOVPE growth and crystal structure analysis by XRD

3. 1 Thin film growth by MOVPE

All the films in this study were grown by metal organic vapor phase epitaxy (MOVPE). Some common names for MOVPE are OMVPE (organometallic vapor phase epitaxy) and MOCVD (metal organic chemical vapor deposition). MOVPE is a chemical vapor deposition method commonly used to produce single or polycrystalline films. The advantage of MOVPE lies in the fact that readily transportable, high purity organometallic compounds can be flown for the epitaxial deposition of doped and undoped semiconductors. It is the most versatile growth technique covering all III/V and II/VI compounds and it also has demonstrated suitability for large-scale production.[1]

An MOVPE system is constructed of several subsystems such as reactant storage, gas handling, reaction chamber, and pump/exhaust.[2] Figure 3.1 represents the MOVPE system that is used in this study which was designed specifically for the growth of oxide thin films. This MOVPE system uses atmospheric pressure with a horizontal type reactor.

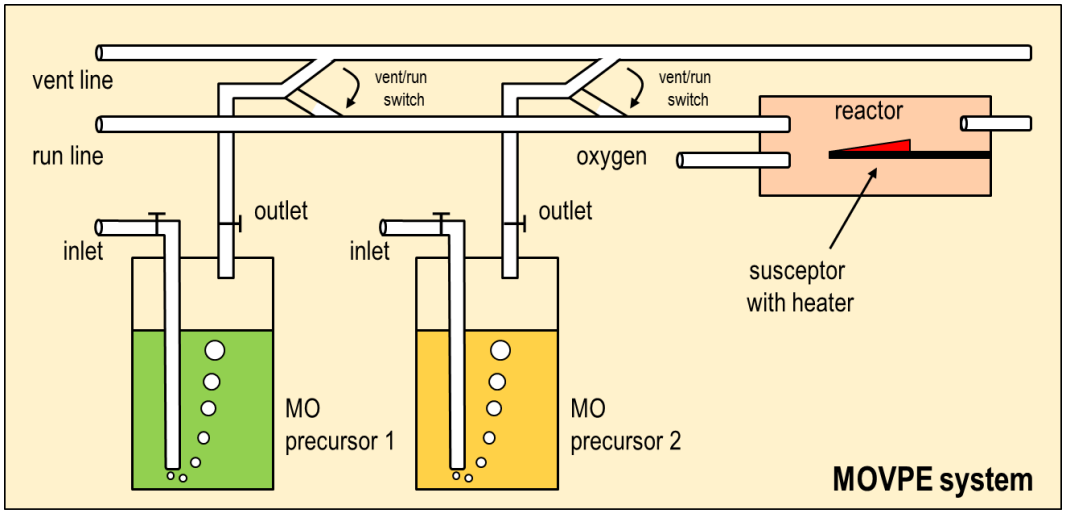

Figure 3.1 Main parts of the MOVPE system used to grow oxide thin films in this study

A metallo-organic precursor for the deposition is stored inside a bubbler. In the bubbler, a precursor is heated to the desired vapor pressure. The carrier gas (N_2) is flown into the bubbler to carry the vapor phase precursor to the vent lines. The vent and run line switching mechanism is employed to let the flow of gases stabilize in the vent line then switch into the run line for growth. In the reactor chamber, a substrate is placed on a susceptor and heated to the desired growth temperature. The precursor is then carried to reactor chamber by switching from the vent to the run line. It is thermally decomposed by a heated substrate and introduced to oxygen to form the desired oxide thin films.

The process inside the reactor is summed up as follows.[3]

1. Transport of reactants
    a. by forced convection to deposition region
    b. by diffusion from main gas flow to substrate through boundary layer
2. Adsorption of reactants on the substrate surface
3. Surface processes:
    a. Chemical decomposition/reaction
    b. Surface migration
    c. Site incorporation
    d. Redesorption of precursors
    e. Desorption of surface reactions products

4. Byproducts desorption from surface
5. Transport of byproducts
    a. by diffusion to main gas flow through boundary layer
    b. by forced convection

Figure 3.2 illustrates some of the process which leads to nucleation of reactants and growth of film on the surface of the substrate.

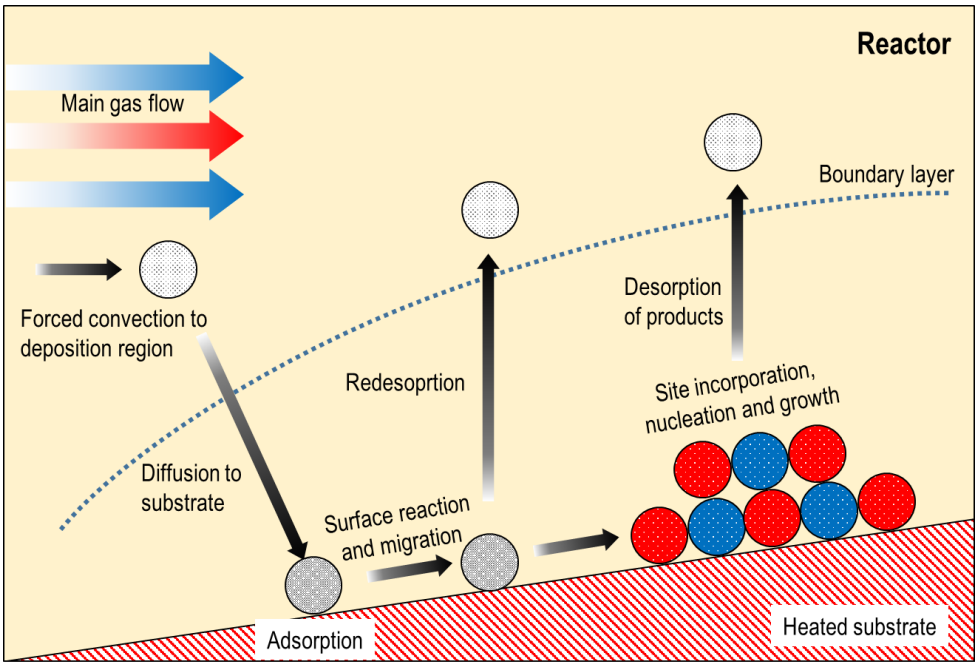

Figure 3.2 Some of the processes inside an MOVPE reactor

The following calculation is carried out in order to estimate the actual amount of reactants flown in the gases. The ideal gas law states that the amount of gas is determined by its pressure, volume, and temperature.

$$PV = nRT \ldots (1)$$

P: Gas pressure (Pa),
V: Volume of gas (m^3),
n: Amount of substance (mol),
R: Ideal gas constant (8.314 $JK^{-1}mol^{-1}$),
T: Temperature (K)

For precursor and carrier flowing in the line, the equation (1) becomes

$$(P_{car} + P_{prec})V_{in} = (n_{car} + n_{prec})RT$$

P_{car}, P_{prec}: Carrier, Precursor gas pressures (Pa),
V_{in}: Volume of gas in the line (m^3),
n_{car}, n_{prec}: Amount of substance of carrier, precursor gas (mol),

the partial pressure for the carrier gas is

$$P_{car}V_{in} = n_{car}RT$$

and the partial pressure for the precursor is

$$P_{prec}V_{in} = n_{prec}RT$$

$$\frac{P_{car}}{P_{prec}} = \frac{n_{car}}{n_{prec}}$$

The precursor mole fraction is

$$n_{prec} = n_{car}\frac{P_{prec}}{P_{car}}$$

$$n_{prec} = n_{car}\frac{P_{prec}}{P_{total} - P_{prec}} \ldots (2)$$

Since the gas flow meter in our system is in sccm, unit conversion into umol/min is necessary. F represents the flux of gas in sccm. Dividing all sides in the ideal gas law with time in minute, t, gives

$$\frac{n}{t} = \frac{P}{RT}\frac{V}{t}$$

By replacing the unit of volume/time in m^3/minute to cm^3/minute which is represented by F, we obtain

$$\frac{n}{t} = \frac{P}{RT} F . 10^6$$

In umol STP (P=101325 Pa, R=8.314 Pa.m^{3}K^{-1}, T=273.15K),

$$\frac{n}{t}\left[\frac{umol}{min}\right] = 44.618F \ldots (3)$$

P_{prec} in equation (2) is the partial pressure of the precursor. It can be obtained by fitting the temperature to vapor pressure plot (supplied by the manufacturer) with the following equation

$$P_{Ni}[torr] = 10^{A-\frac{B}{T}} \ldots (4)$$

Using equation (2) to calculate amount of precursor to be deposited, and substituting from equation (3) and (4) we obtain the following formula for the precursor molar fraction.

$$n_{prec} = n_{car} \frac{P_{prec}}{P_{total} - P_{prec}}$$

$$n_{prec}\left[\frac{umol}{min}\right] = 44.618 . F \frac{10^{A-\frac{B}{T}}}{760 - 10^{A-\frac{B}{T}}} \ldots (5)$$

3. 2 MOVPE challenges and key improvements for the growth of oxides

MOVPE are commonly employed in the growth of III-V materials but not oxides. The growth of oxides by MOVPE is not common. It has its own challenges and difficulties. In the early days of growth there was a major problem with quality of thin film deposition. By using a conventional horizontal reactor, depicted in Figure 3.3 (a), growth resulted in films with unwanted deposits as seen in Figure 3.3 (b).

It was found that the deposit was produced by parasitic gas phase reaction occurred due to the use of oxygen, which is easily reactive. Reaction between O_2 and metal precursor started as soon as they were released from each pipes and were mixed in the reactor. The reaction which occurred in the distance far enough from the substrate produce unwanted deposits which were be transported onto the substrate and disturbed the epitaxy of oxide thin films.

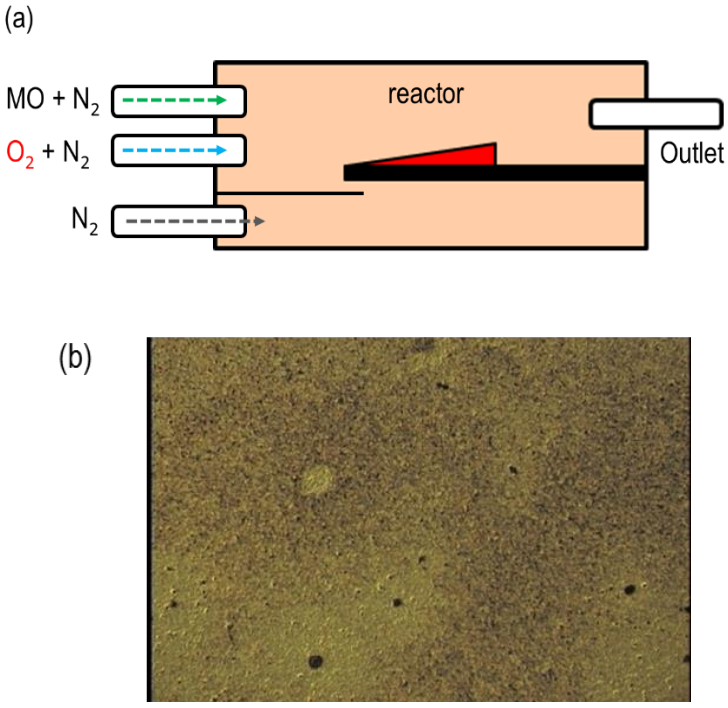

Figure 3.3 (a) Schematic of a conventional MOVPE reactor. (b) Film surface exhibiting unwanted deposits as a result of parasitic gas phase reaction

In order to overcome this challenge, the reactor was modified such that gas phase reaction between O_2 and metal precursor is suppressed. A separator was installed in between the O_2 and metal precursor flows as schematically drawn in Figure 3.4 (a). This has effectively separated the gases of O_2 and metal precursor until in the area very close to the substrate. This was confirmed by the shades formed in the reactor after growths as shown in Figure 3.4 (b). The separator worked well to suppress the parasitic gas phase reaction which resulted in growth of films with clean surface as shown in Figure 3.4 (c).

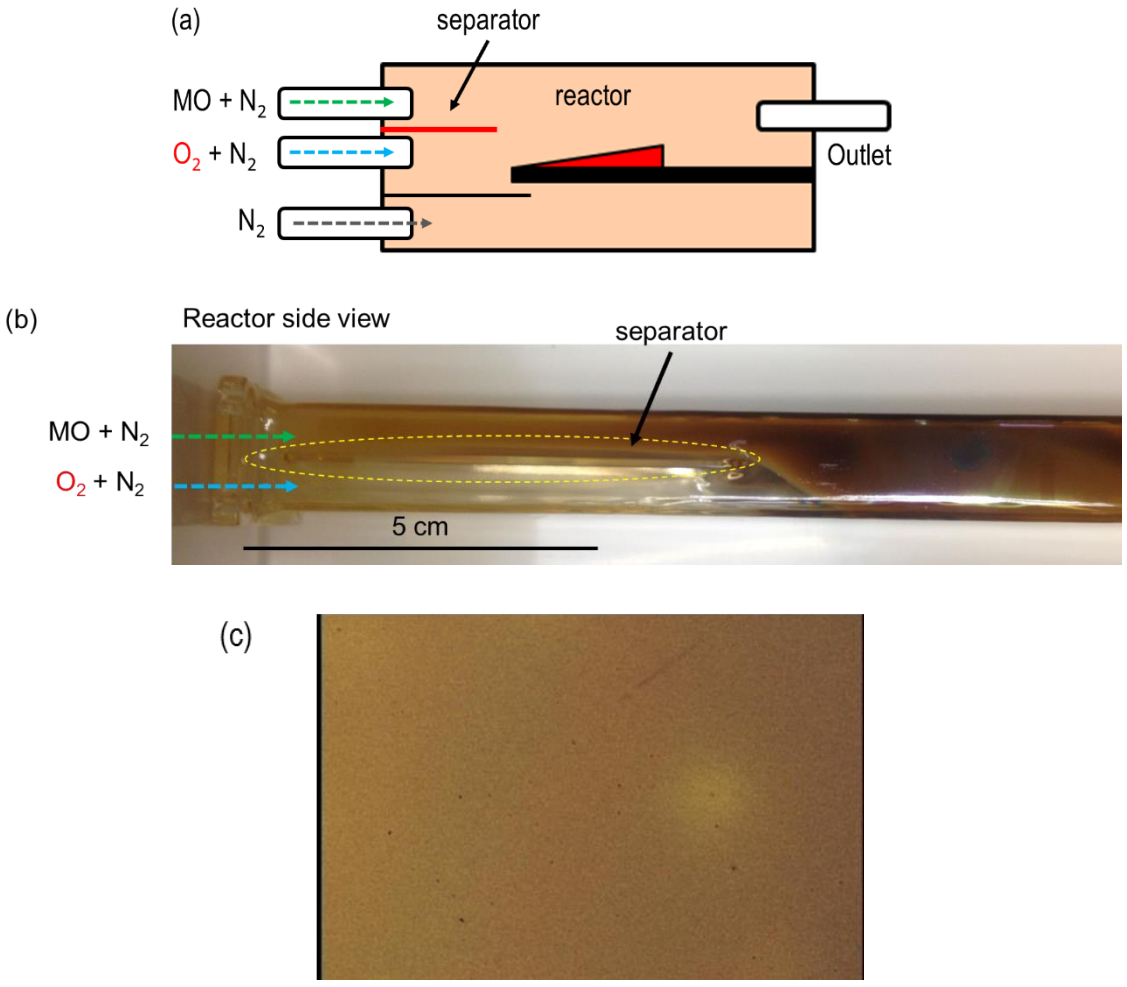

Figure 3.4 (a) schematic of the modified MOVPE reactor. (b) picture of the real reactor after growth. It can be observed that the separator has prevented the mixing of O_2 and Ni precursor. (c) the resulting film after separator installation.

The next challenge in the early growth of oxides was poor deposition coverage and uniformity. Some of the deposited films are shown in Figure 3.5 (a). The substrate was a quarter of a 2″ wafer. The use of conventional nozzle, ordinary hole nozzle was found to be the problem. From the top view, it is envisaged that an ordinary hole nozzle can cause a flow of materials only in a narrow region through the substrate as depicted in Figure 3.5 (b).

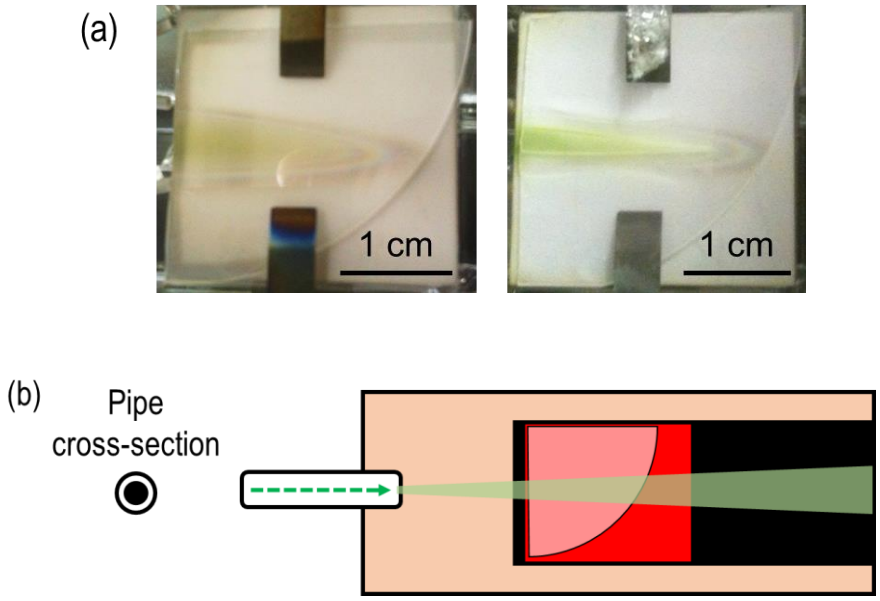

Figure 3.5 (a) Poor deposition coverage and uniformity found in the early samples. (b) Schematic illustrations of the gas flow in growths using ordinary hole nozzles.

In order to increase the spread of gas flow and improve the deposition coverage, a specially made shower nozzle was used. The nozzle does not only have a single hole in the end, but several smaller holes and several holes around the sides as depicted in Figure 3.6 (a). The resulting film, shown in Figure 3.6 (b), indicates the improved deposition coverage and uniformity.

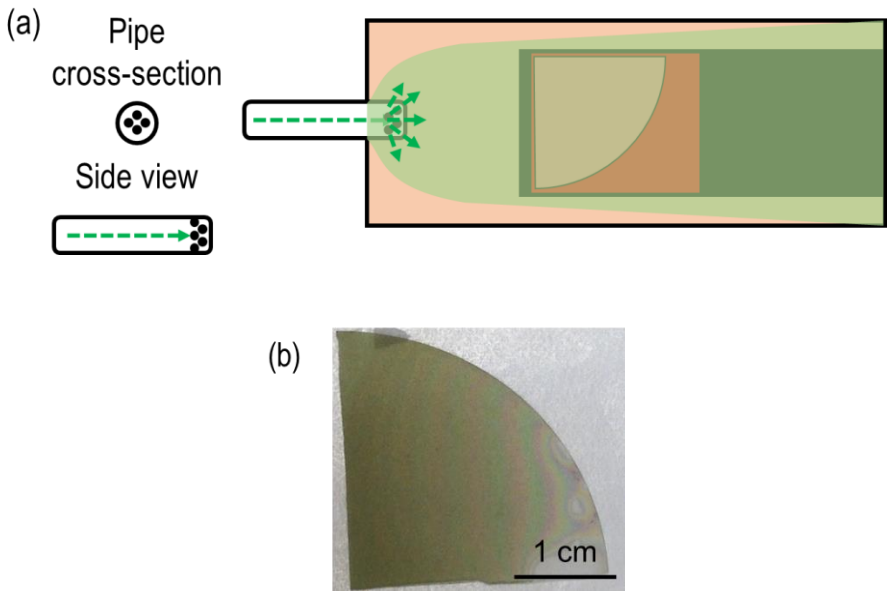

Figure 3.6 (a) Schematic illustrations of the gas flow in growths using shower nozzles. (b) A typical film grown by using shower nozzle showing improved deposition coverage and uniformity.

The two improvements made in the design of MOVPE reactor in this study is found to be crucial for the growth of oxides. The addition of separator helped suppressed parasitic gas phase reaction caused by the easily reactive O_2 and the use of shower nozzle improved the deposition coverage which could not be achieved by using ordinary hole nozzle.

3. 3 X-ray diffraction

X-ray diffraction (XRD) is used to determine the crystal structure, orientation, and other structural properties of the grown films. XRD is based on the X-ray scattering phenomena in crystal lattice which is described by the Bragg's law.[4] The law explains that constructive interference is observed when the length of scattering is equal to integer multiplication of the wavelength.

$$2d \sin\theta = n\lambda$$

d : interplanar distance
θ : diffraction angle
n : integer number
λ : X − ray wavelength

The following diagram in Figure 3.7 represents concept of Bragg's law. Beams with identical wavelength and phase are scattered off atoms within crystalline solid. The lower beam travels an extra length of $2d \sin\theta$.

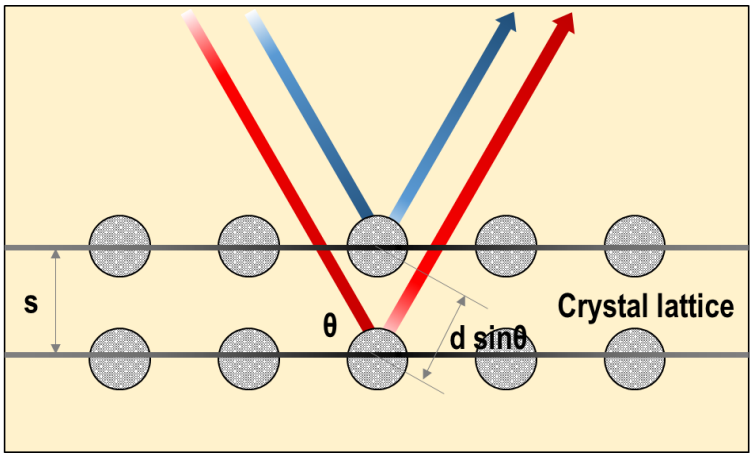

Figure 3.7 Concept of Bragg Law

Several XRD scan modes were employed in this study, namely the, θ-2θ, grazing incident angle (GI-XRD), φ, and rocking curve (RC) scans. Each of these has a different objective and

configuration. Presented in Figure 3.8 is the basic configuration and term of reference for XRD system used in this work.

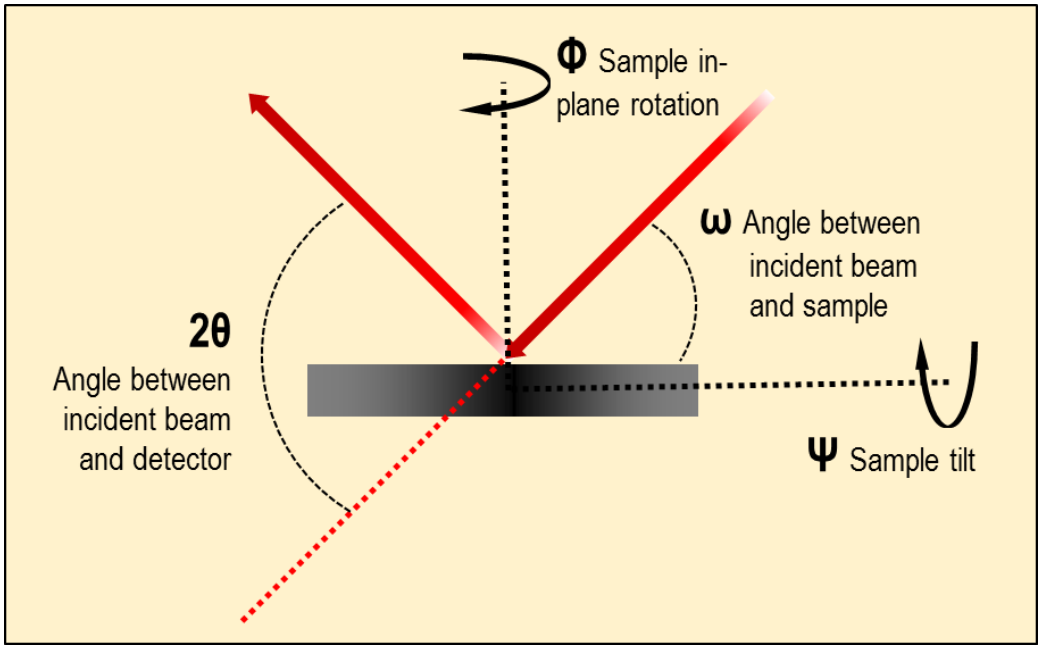

Figure 3.8 Basic configuration in XRD

The θ-2θ scan works based on the Bragg diffraction angles. The incident X-ray and the detector moves in a coupled manner such that ω is always half of the 2θ, fulfilling the condition of Bragg diffraction. The existence of diffraction peak, its shape and intensity can be used to determine whether the film is amorphous, polycrystalline or single. When peaks are detected, its position provides the information of interplanar spacing of the crystal based on the Bragg's law. In this study, diffraction patterns from the θ-2θ scan is used to identify phase and crystal structure based on the comparison with the powder diffraction file (PDF) of the International Centre for Diffraction Data (ICDD).[5]

Patterns from θ-2θ scan are also used in determination of the crystallographic orientation relationship (COR) in the out-of-plane direction. This COR correlate the crystallographic plane

of substrate to that of film in the out-of-plane direction or the growth direction. Besides, the FWHM of diffraction peak in the θ-2θ scan may be used to estimate the crystallite size according to the Scherrer Equation.[4]

$$L_{hkl} = \frac{\lambda}{\beta \cos \theta}$$

L : crystallite size (nm)
λ : X-ray wavelength (nm)
β : peak width (radian)
θ : peak position (°)

The GI-XRD allows detection of the less dominant planes which are not parallel to the sample surface. In this setup, the incident X-ray is fixed at a very small ω angle slightly larger than the critical angle of total internal reflection. Only the detector is moved, scanning any scattered X-rays. This setup allows penetration of X-ray in an almost parallel direction throughout the sample resulting in a higher sensitivity compared to θ-2θ scan in which X-ray penetrates only along the thickness of the sample. In this study, existence of diffraction peaks in GI-XRD scan is used to confirm the polycrystalline nature of the film. In other words, the absence of peak in GI-XRD confirms that the grown film is single crystal.

The RC scan is employed to investigate the crystal quality of the film, in terms of crystal orientation distribution (mosaic structure) and variation in interplanar spacing based on its peak width (FWHM). In this setup, the film is first aligned to yield the maximum peak intensity of a plane of interest. The incident X-ray and the detector is then fixed according to the Bragg's angle of the plane. The sample is then rocked within a few degree of ω with a detector slit wide opened. A higher degree of mosaicity (distribution of crystal orientation) will result in a wider diffraction peak.[6] In this study, the FWHM value in the RC scan is used as a measure of crystal quality. The values are used to compare crystal quality of samples grown by MOVPE and by other deposition methods.

In the φ scan, X-ray source and detector were fixed into a Bragg's angle of a target plane. The sample is then rotated in a predetermined axis. Diffraction peaks of the target plane which appear during the rotation indicates its rotational symmetry characteristics. This setting can be repeated for planes of the substrate and the film. In this study, the φ scan is used in determination of in-plane COR by using the growth direction as the rotation axis. The in-plane COR correlate the plane of film and that of substrate in the asymmetric direction (non-parallel to the growth direction).

References

[1] G.B. Stringfellow, *Organometallic Vapor-Phase Epitaxy: Theory and Practice* (Academic Press, 1999).

[2] A. Rockett, *The Materials Science of Semiconductors* (Springer Science & Business Media, 2008).

[3] J. Plummer, M. Deal, and P. Griffin, *Silicon VLSI Technology* (Prentice Hall, 2000).

[4] C. Hammond, *The Basics of Crystallography and Diffraction* (Oxford University Press, 2001).

[5] Y. Waseda, E. Matsubara, and K. Shinoda, *X-Ray Diffraction Crystallography: Introduction, Examples and Solved Problems* (Springer Science \& Business Media, 2011).

[6] D.K. Bowen and B.K. Tanner, *X-Ray Metrology in Semiconductor Manufacturing* (CRC Press, 2006).

CHAPTER 4

Effect of O_2/Ni precursor ratio

This chapter comprises the growth of NiO films on sapphire substrates with emphasis on the effect of oxygen to nickel ratio on the structure, morphology, optical, and electrical properties of the MOVPE grown films. Optimization of the oxygen to nickel precursor ratio has been carried out by varying the O_2/Ni molar ratio. The flow of O_2 and Ni have been adjusted in order to obtain molar ratios in the range of 542:1 to 5641:1.

4. 1 Experimental details

NiO was grown on sapphire substrates by atmospheric-pressure MOVPE at 500°C for 5 hours. Ni precursor flow of 80 sccm and 100 sccm were used, while that of oxygen was varied from 60 sccm to 500 sccm. By adjusting the flow rates, films with oxygen to nickel precursor ratio of 542:1, 1354:1, 2617:1 and 5641:1 were obtained. The obtained samples are referred to as 0.5k, 1k, 2k, and 5k respectively. Allyl(cyclopentadienyl)nickel ($C_8H_{10}Ni$) was used as nickel precursor and was kept at 30°C to obtain vapor pressure of 0.84 torr. Pure O_2 gas was used as an oxygen source and N_2 was used as a carrier gas.

XRD scans of grazing incident angle, θ-2θ, ϕ and rocking curve were used to determine the crystal structure, phase, lattice parameters, and quality. The surface morphology was evaluated based on the FE-SEM and AFM images. To investigate the electrical property of the films, resistivity measurements were carried out by using four-point probe and the van der Pauw measurement techniques. The optical transparency dependence of the growth atmosphere was analyzed based on the transmittance measurement by UV-vis spectroscopy.

4. 2 Results and discussions

4. 2. 1 Structural characterization

The result of XRD θ-2θ scan is shown in Figure 4.1 (a). The lowermost graph is the diffraction pattern of the Al_2O_3 substrate alone. The peaks at 41° and 90° have been associated with the Al_2O_3 substrate which is consistent to the PDF #46-1212. In all NiO samples, two additional diffraction peaks can be observed at 37° and 79°. These two peaks correspond to cubic NiO of (111) and (222) planes respectively based on the PDF #47-1049. The exclusive presence of these peaks indicates that the samples are highly oriented along [111] direction.

A ϕ scan was also conducted for the (200) plane. It was carried out by inclining the sample 54.73° from the (111) plane with Bragg condition for (200) plane θ and 2θ of 21.64° and 43.28°, respectively. Six diffraction peaks of (200) plane were observed every 60° as shown in Figure 4.1 (b). This six fold symmetry of (200) reflection from the film normal to [111] indicates the existence of two-phase domains around the [111] axis rotated 60° with respect to each other as denoted by close-diamond and open-circle peaks. This result is similar to our previously grown film[1]. Two-phase domain formation of NiO films was also reported for pulsed laser deposition and molecular beam epitaxy.[2,3] The unequal intensities of the peaks in the ϕ scan was probably a result of the unequal domain sizes of the twinned and non-twinned structure. Besides, lattice mismatch can also cause a variation of lattice relaxation in lateral direction which were also found in NiO grown by PLD.[2] Further analysis on the domain formation is given in chapter 5, section 2.2 of the thesis.

The result of grazing incident angle scan further confirms that all samples possess well oriented crystal structure as shown in Figure 4.2. It is clearly seen in this figure that no

significant diffraction peaks are observed. This indicates that all the samples are well oriented only along the growth direction similar to that of the sapphire substrate.

Figure 4.3 presents the full width at half maximum (FWHM) of (111) peak in this θ-2θ scan as well as its rocking curve scan. Both measurements showed decreasing tendency of FWHM as oxygen increases and clarified the improvement in crystal quality i.e. interplanar spacing distribution and orientation distribution. FWHM in rocking curve measurement of as low as 0.106° was obtained.

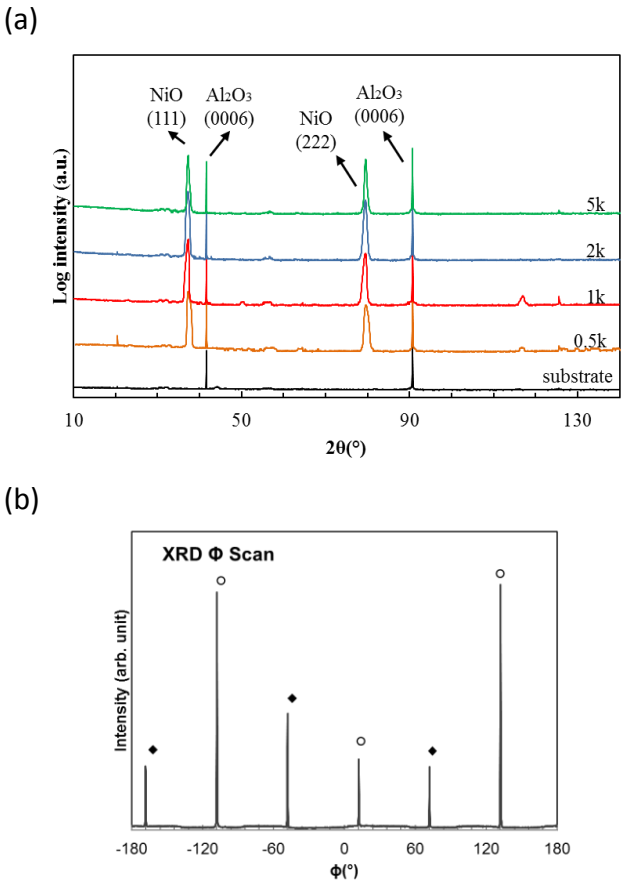

Figure 4.1 (a) XRD θ-2θ scan of sapphire substrate and the varied O_2/Ni ratio samples. (b) XRD ϕ scan of 5k sample for (200) plane which is inclined 54.73° from the (111) plane with Bragg condition θ-2θ for (200) plane of 21.64° and 43.28°

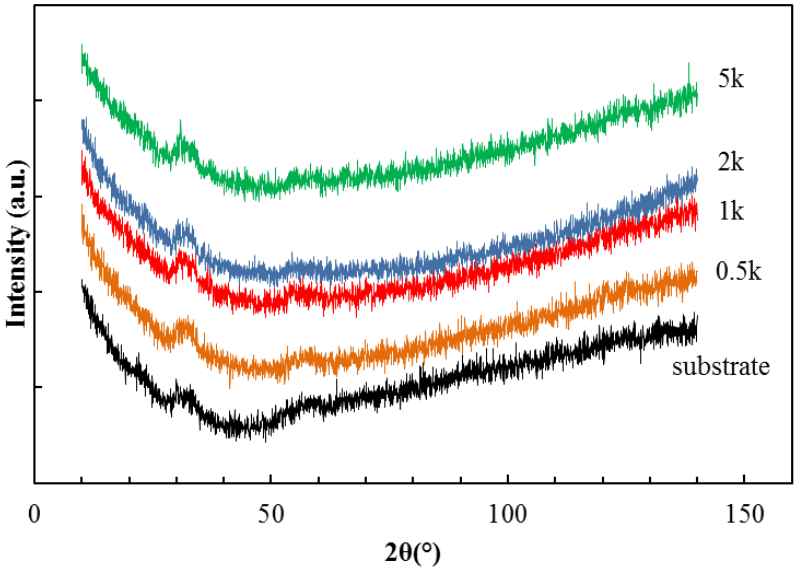

Figure 4.2 Grazing incident angle XRD of sapphire substrate and the varied O_2/Ni ratio samples at θ of 0.6°

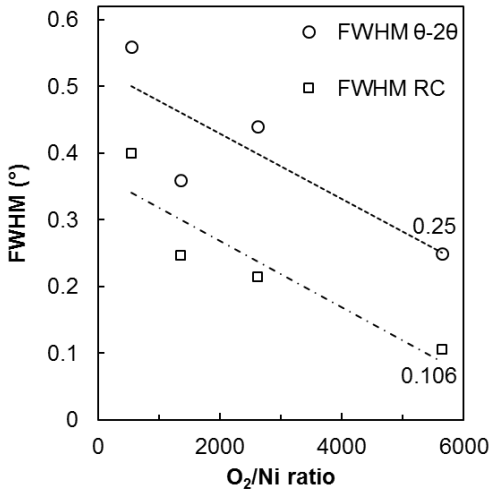

Figure 4.3 FWHM of (111) peak in θ-2θ and rocking curve (RC) scans plotted as a function of O_2/Ni ratio

4. 2. 2 Surface morphology

The surface morphology of the samples, as evaluated based on the AFM images, is presented in Figure 4.4. The 0.5k sample exhibited rough surface with average roughness of 68.9 nm, while higher O_2/Ni ratio sample i.e. 5k sample exhibited smoother surface with average roughness of

9.12 nm. For comparison, an average roughness of 1 nm was reported for NiO grown on Al_2O_3 by ALD but only for 45 nm thick film.[4] The introduction of higher oxygen concentration in the growth may have caused supersaturation of oxygen adatoms on a growing surface that resulted in improved surface morphology. It has also improved the crystallization process in terms of preventing excess desorption of Ni adatoms and increasing the lateral growth rate. It can be inferred from the smooth surface of the 5k sample that a more uniform nucleation occurred. Indications of improved nucleation and coalescence of islands can be clearly seen in rather macro scale images of an optical microscope with 100x magnification in Figure 4.5. Bubbles can be observed in film grown with low O_2/Ni ratio. The bubbles shrank as the O_2/Ni ratio increased. Films grown with higher O_2/Ni ratio showed smooth surface, in agreement with the AFM results.

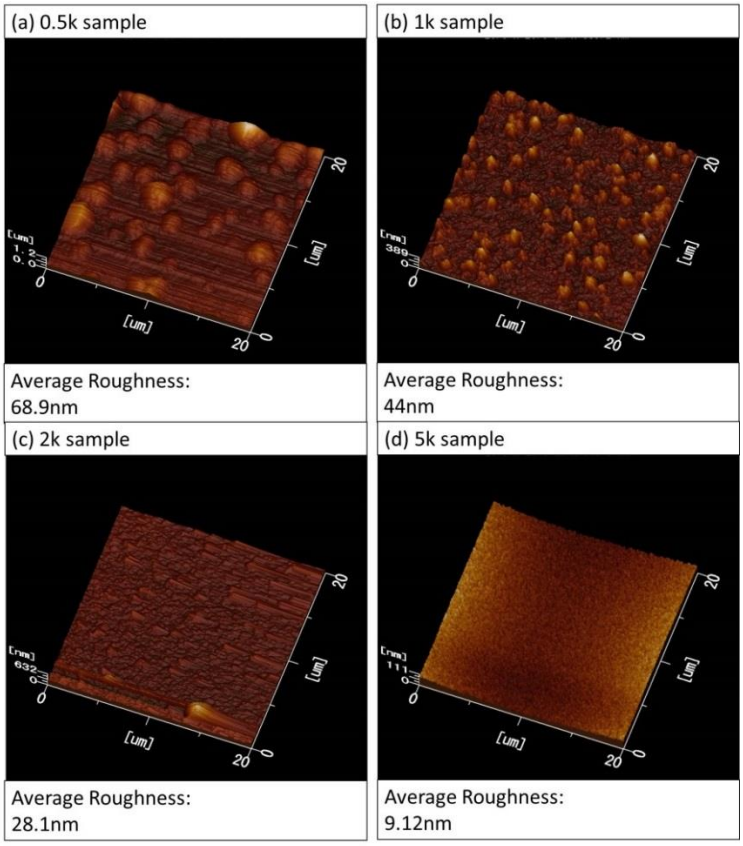

Figure 4.4 AFM Images and average roughness values of (a) 0.5k sample, (b) 1k sample, (c) 2k sample, (d) 5k sample

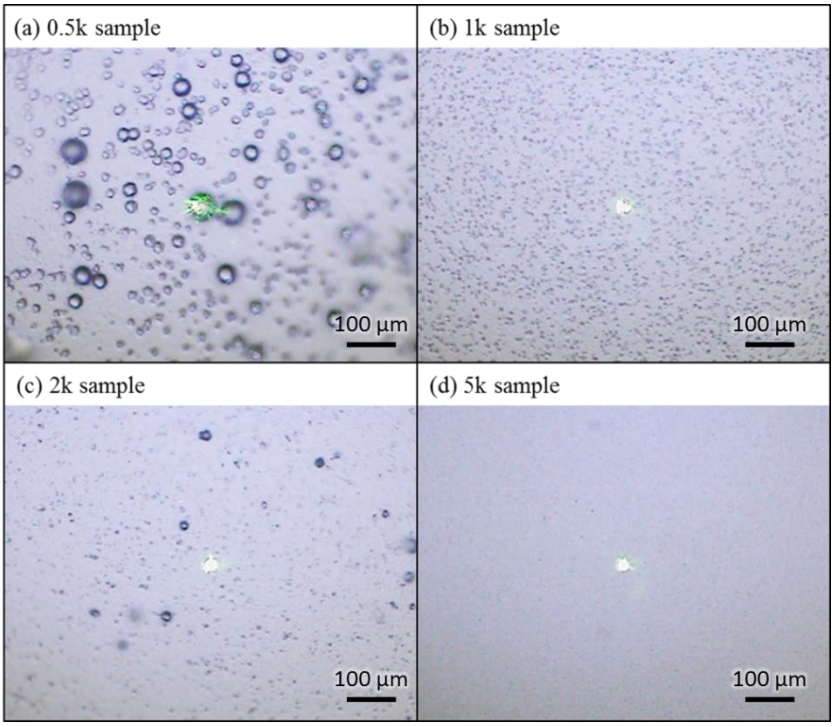

Figure 4.5 Surface morphology of varied O_2/Ni films at 100 times magnification by optical microscope

Similar results were also obtained in the FE-SEM images as shown in Figure 4.6. The surface of the sample with the lowest O_2/Ni ratio appears granular, with non-uniform islands. Islands were formed because the oxygen required for reaction with nickel was lacking. Indeed, it was confirmed by wavelength dispersive spectroscopy (WDS) mapping (Figure 4.7) that these islands lacked oxygen. The islands and voids diminished with the increased O_2/Ni ratio. The surface of the sample with the highest O_2/Ni ratio was smooth and compact, with coalesced tetrahedrons. The results further confirms that the increased availability of O_2 led to a more uniform growth throughout the films, which resulted in a smoother surface.

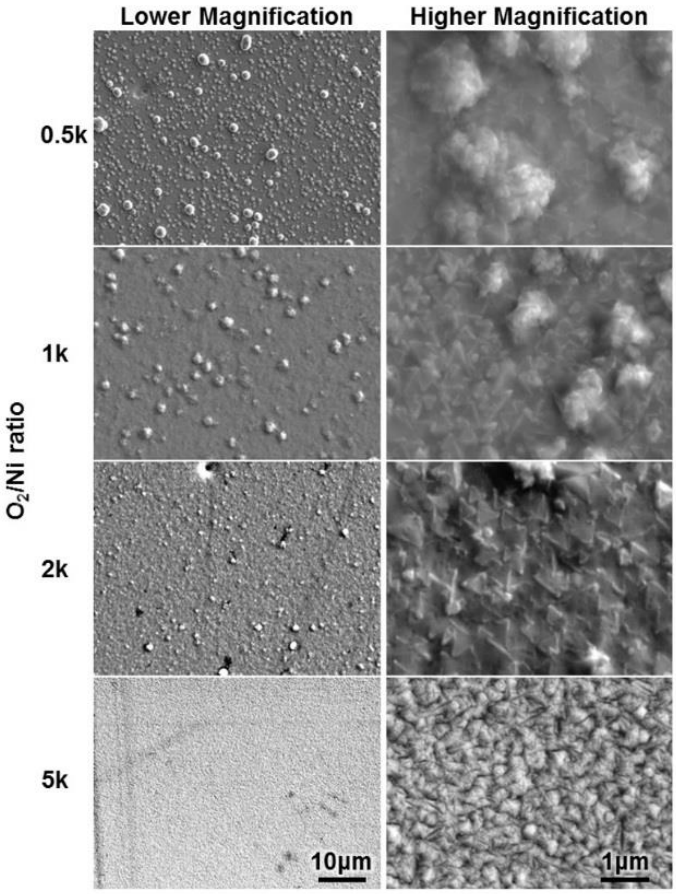

Figure 4.6 SEM micrographs of NiO samples with various O_2/Ni ratios. Lower and higher magnifications are shown on the left and right panels, respectively.

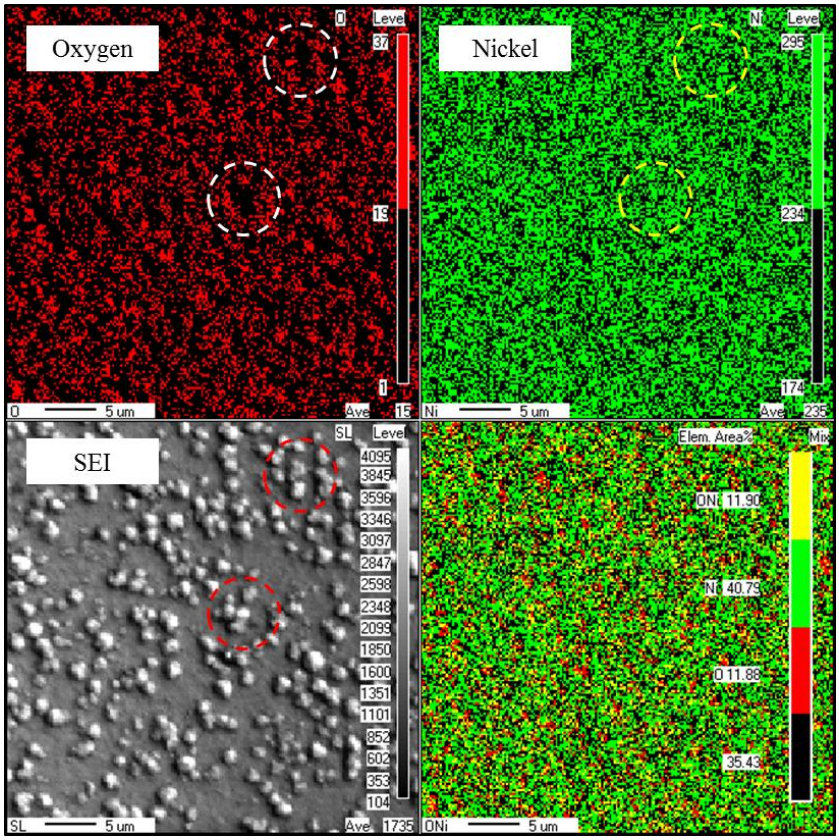

Figure 4.7 WDS element mapping of oxygen and nickel in the 0.5k sample

4. 2. 3 Electrical characterization

Four-point-probe measurement shows that the resistivity decreased by an order of magnitude with increasing O_2/Ni ratio. The decreased resistivity can be attributed to a better crystallinity in films grown at higher O_2/Ni ratios which results in increased carrier mobility. Furthermore, NiO films grown on Al_2O_3 may generate more Ni vacancies with improving crystallinity due to the compressive stress. It should be noted that introduction of more O_2 during growth at a higher O_2/Ni ratio may influence the stoichiometry, but an oxygen richness should cause a shift in the XRD reflection peak. Since the XRD peak does not show a significant shift, the O_2/Ni ratio's effect on stoichiometry is not significant enough to affect the carrier concentration. Although a possibility of the increased carrier concentration with the increased O_2/Ni ratio was not excluded,

it was concluded that the decreased resistivity was more likely due to the increased mobility resulting from the improved crystallinity.

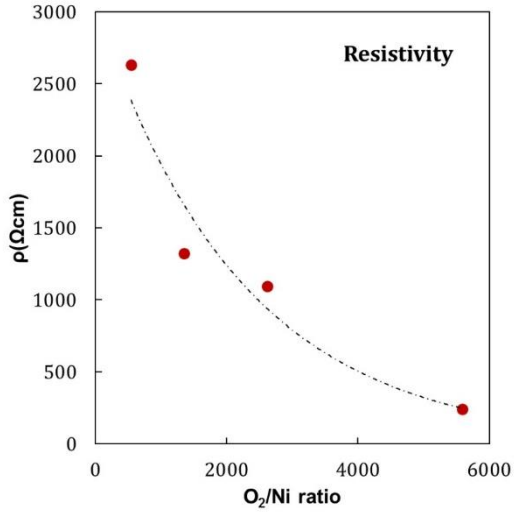

Figure 4.8 Resistivity of samples as a function of increasing oxygen to nickel ratio

4. 2. 4 Optical characterization

As shown in Figure 4.9, the transmittance in the visible range (390 nm-700 nm) increased with increasing O_2/Ni ratio. The average transmittances for 0.5k, 1k, 2k, and 5k films were 22%, 44%, 56%, and 71%, respectively. The decreased transmittance at lower O_2/Ni ratio can be attributed to the rougher surface and formation of structural defects in the films, which scatter light incident on the samples. The plots of $(\alpha h\nu)^2$ to $(h\nu)$ are shown in the inset of Figure 4.9. The direct nature of transition is assumed since the plots are almost in linear trend. Extrapolation of these curves to photon energy axis gives an estimate of the band gaps. The fundamental absorption edge shifted toward higher photon energy with increasing O_2/Ni ratio, which indicates a bandgap increase. As the crystal quality improves with higher O_2/Ni ratio, the formation of defect-related recombination centers is suppressed, allowing a more pronounced band-to-band transition.

Table 4.1 Comparison of transparent conductor's Figure of Merits (FoM) for films grown in this study with other works of NiO.

Deposition	Transmittance (% at 550 nm)	Thickness (μm)	Sheet Resistance (MΩ/□)	FoM (Ω-1)	Bandgap (eV)
This work (0.5k)	25	0.9	29. 3	$3.4x10^{-14}$	3.4
This work (1k)	50	1.3	10.2	$1.0x10^{-10}$	3.55
This work (2k)	63	1.5	7.29	$1.4x10^{-9}$	3.6
This work (5k)	76	0.9	3.61	$1.8x10^{-8}$	3.6
Sputter[6]	40	0.11	0.018	$5.8x10^{-9}$	3.8
Sputter[7]	60	0.11	0.805	$7.5x10^{-9}$	3.65
Sputter[8]	58.4	0.09	0.30	$1.5x10^{-8}$	3.5
Plasma MOCVD[9]	95	0.2	23.1	$2.6x10^{-8}$	3.93
Sputter[10]	55	0.035	0.036	$7.0x10^{-8}$	NA

In order to evaluate the properties of the films with respect to transparent conductor application, a figure of merit (FoM) widely used for transparent conductor was employed. The FoM was proposed by Haacke[11] and was defined as follows with T the transmittance at 550 nm and R_s the sheet resistance.

$$\Phi_{TC} = \frac{T^{10}}{R_S}$$

Comparison of the electrical and optical properties of the obtained films with other works of NiO is given in Table 4.1. The best result of this study was obtained at O_2/Ni ratio of 5k. Its FoM value is comparable to other works of NiO except for the sputter deposited film in reference 10. It is important to note that the material performance can further be improved by optimizing the

thickness of the films. Nevertheless, the transparency of the currently obtained film is superior to all the sputter-grown NiO.

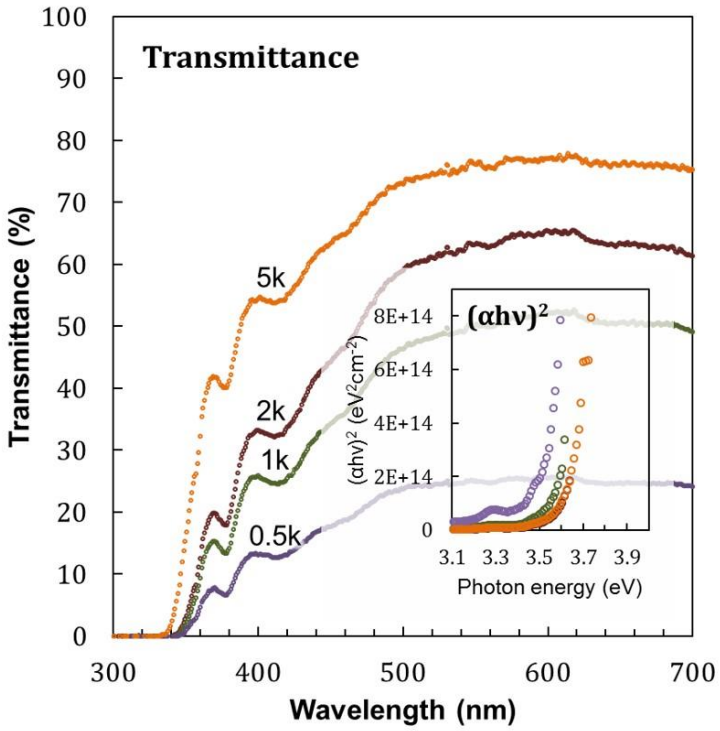

Figure 4.9 Transmittance plot of varied O_2/Ni ratio NiO thin films. Inset is band-gap approximation plot of $(\alpha h\nu)^2$ to $(h\nu)$

4. 3 Conclusions

It can be concluded that the increase of O_2/Ni ratio has improved the nucleation and crystallization process as indicated by smoother surface confirmed through AFM, SEM, and optical measurements. FWHM values also indicated that the growth with higher O_2/Ni ratio led to the formation of highly oriented structure with less variation in the interplanar spacing. The increase of O_2/Ni ratio also suppresses the void formation and decreases the resistivity by means of reduced grain-boundary scattering. The formation of a non-stoichiometric film due to higher O_2/Ni ratio was also considered as a reason for the decreased resistivity. It has been shown that

the O_2/Ni ratio in the growth of NiO has significant effects on the film structure and its electrical and optical properties.

References

[1] K. Uchida, K. Yoshida, D. Zhang, A. Koizumi, and S. Nozaki, AIP Advances **2**, 042154 (2012).

[2] P. Gupta, T. Dutta, S. Mal, and J. Narayan, Journal of Applied Physics **111**, 013706 (2012).

[3] C. Mocuta, A. Barbier, G. Renaud, Y. Samson, and M. Noblet, Journal of Magnetism and Magnetic Materials **211**, 283 (2000).

[4] E. Lindahl, J. Lu, M. Ottosson, and J.-O. Carlsson, J. Cryst. Growth **311**, 4082 (2009).

[5] C. Hammond, *The Basics of Crystallography and Diffraction* (Oxford University Press, 2001).

[6] H. Sato, T. Minami, S. Takata, and T. Yamada, Thin Solid Films **236**, 27 (1993).

[7] M. Tyagi, M. Tomar, and V. Gupta, Materials Research Bulletin **66**, 123 (2015).

[8] J.-H. Oh, S.Y. Hwang, Y.D. Kim, J.-H. Song, and T.-Y. Seong, Materials Science in Semiconductor Processing **16**, 1346 (2013).

[9] H. Wang, G. Wu, X. Cai, Y. Zhao, Z. Shi, J. Wang, X. Xia, X. Dong, B. Zhang, Y. Ma, and others, Vacuum **86**, 2044 (2012).

[10] M. Grilli, F. Menchini, T. Dikonimos, P. Nunziante, L. Pilloni, M. Yilmaz, A. Piegari, and A. Mittiga, Semiconductor Science and Technology **31**, 055016 (2016).

[11] G. Haacke, Journal of Applied Physics **47**, 4086 (1976).

CHAPTER 5

MOVPE growth and characterization of single crystal NiO

To realize a functional NiO material, synthesis of high-quality NiO and understanding of its fundamental characteristics are very important. However, growth of NiO has been limited to the formation of polycrystalline NiO on glass substrates[1–4] and single-crystalline NiO with two domains (twin) on Al_2O_3 substrates[1,5,6]. Very few studies have reported the growth of single-crystalline NiO[7] or described the effects of the crystal structure on the film properties[8]. Thus, a study on the effects of various growth parameters followed by characterization of the NiO properties is of significant interest. The capability of growing single-crystalline NiO and its characterization will improve understanding of the fundamental characteristics of NiO.

This chapter comprises MOVPE growth of NiO thin films with various growth parameters, i.e., the growth temperature, the precursor material ratio, and the substrate material. Characterization was then carried out on the obtained samples to correlate the effects of the various growth parameters to the film properties, including the crystal structure, resistivity, and optical transmittance.

5. 1 Experimental details

Single-crystalline Al_2O_3(001), MgO(100), and MgO(111) were used as substrates for the growth. Prior to growth, the substrates were degreased in an ultrasonic bath of acetone, ethanol, and deionized water for 10 minutes each. Allyl(cyclopentadienyl)nickel ($C_8H_{10}Ni$) was used as the nickel precursor and was kept at 30 °C to obtain a vapor pressure of 0.84 torr. Pure O_2 gas was used as an oxygen source, and N_2 was used as a carrier gas. Substrates were placed on the

susceptor inside the reaction chamber and heated to the desired growth temperature with a constant flow of N_2. The growth temperature was measured using a thermocouple inserted into the susceptor.

To investigate the effects of growth temperature on the properties of NiO, growth temperatures of 300 °C, 400 °C, 500 °C, and 600 °C were employed, with a typical growth time of 5 hours. The flows of precursors were fixed to ensure that the same amounts of materials were flown onto the substrate in all growth processes. The obtained films were subjected to structural characterization and electrical resistivity measurements.

To investigate the structural properties of the samples, various configurations of X-ray diffraction (XRD) measurements with Cu Kα radiation (λ = 1.54 Å) were performed. The crystal quality and orientation were investigated by grazing incidence X-ray diffraction (GI-XRD) and θ-2θ scans. Incident angle of 0.6° was used for GI-XRD measurements. Rocking curves and ϕ scans were performed to analyze the crystal quality and the crystallographic orientation relationship (COR) between the film and the substrate. In samples grown on Al_2O_3 substrates, the ϕ scan was performed at a tilt of 54.73° from the NiO(111)/Al_2O_3(001) plane with the Bragg condition satisfying the orientation of the NiO(200) plane (θ and 2θ of 21.64° and 43.28°, respectively). Then, another ϕ scan was performed at a tilt of 42.31° from the NiO(111)/Al_2O_3(001) plane with the Bragg condition satisfying the orientation of the Al_2O_3(116) plane (θ and 2θ of 28.75° and 57.50°, respectively). In samples grown on MgO(100) substrates, ϕ scans were performed on the NiO sample at a tilt of 45.00° from the NiO(100)/MgO(100) plane with the Bragg condition satisfying the orientation of the NiO(220) and MgO(220) planes (θ-2θ of 31.44°–62.88°and 31.15°–62.30°, respectively). Finally, in samples grown on MgO(111) substrates, ϕ scans were performed on the NiO sample at a tilt of 35.26° from the

NiO(111)/MgO(111) plane with the Bragg condition satisfying the orientation of the NiO(220) and MgO(220) planes. The resistivity of all samples was measured by the four-point-probe and van der Pauw method. All of the measurements were carried out at room temperature.

5. 2 Results and discussions

5. 2. 1 Crystal structure and epitaxial relationship

The XRD θ-2θ scan of NiO grown on the Al_2O_3 substrate in Figure 5.2 (a) indicates that NiO was grown in the NiO[111] direction. Peaks of NiO(111) and Al_2O_3(006) were determined based on the powder diffraction files (PDF) from the International Centre for Diffraction Data (ICDD #47-1049 and #46-1212 for NiO and Al_2O_3, respectively). The stronger NiO(111) peak intensity at higher growth temperatures indicates that the films are better crystallized. Although the XRD θ-2θ showed only the NiO[111] peak, the GI-XRD pattern Figure 5.2 (d) reveals that films grown at 300 °C and 400 °C were polycrystalline, with the presence of peaks from NiO(200) and NiO(220), and single crystalline films were obtained at 500 °C and 600 °C.

The XRD ϕ scans were carried out to evaluate the in-plane COR as shown in Figure 5.1. In all samples, six NiO(200) peaks appeared at the same ϕ angle as the Al_2O_3(116) peaks, indicative of a twinned structure. As previously reported[9,10], the CORs for NiO grown on an Al_2O_3 substrate are $[111]_{NiO}||[006]_{Al2O3}$ (out-of-plane) and $[\bar{1}\bar{1}2]_{NiO}||[\bar{1}\bar{1}0]_{Al2O3}$ & $[2\bar{1}\bar{1}]_{twinned\text{-}NiO}||[110]_{Al2O3}$ (in-plane). Twinned NiO on sapphire substrates has also been reported using other deposition methods, such as PLD[11], ALD[12], and RF sputtering[13].

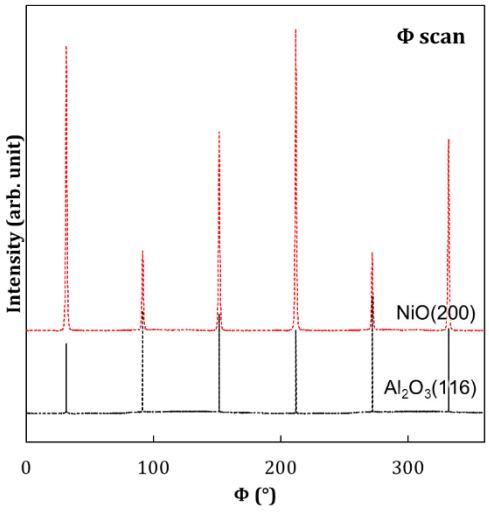

Figure 5.1 XRD patterns (ϕ scan) of thin NiO film grown on Al_2O_3 at 500 °C for 5 hours. The six diffraction peaks of NiO (200) at the same ϕ angle as the Al_2O_3(116) indicate the formation of twin structure in the NiO film. Similar pattern were obtained for other growth temperatures.

Epitaxial growth of NiO on an Al_2O_3 substrate can be explained by using the domain matching epitaxy (DME) framework, which employs matching of domains rather than lattice parameters[11,13,14]. In the current system, a 7% mismatch between the in-plane spacings of $\sqrt{2}.d_{NiO(200)}.\sin 60°$ and $d_{Al2O3(110)}$ would occur based on the bulk parameters. However, the NiO(200) peak position obtained from the XRD rocking curve scan indicates that the film was not fully relaxed to its bulk parameters, such that the misfit strain between NiO and Al_2O_3 was 6.2% ($\varepsilon = \frac{2.526}{2.379} - 1$). The DME framework suggests that this mismatch can be accommodated by matching of 16/17 and 17/18 NiO to Al_2O_3 domains, which alternates with a frequency factor of 0.13.

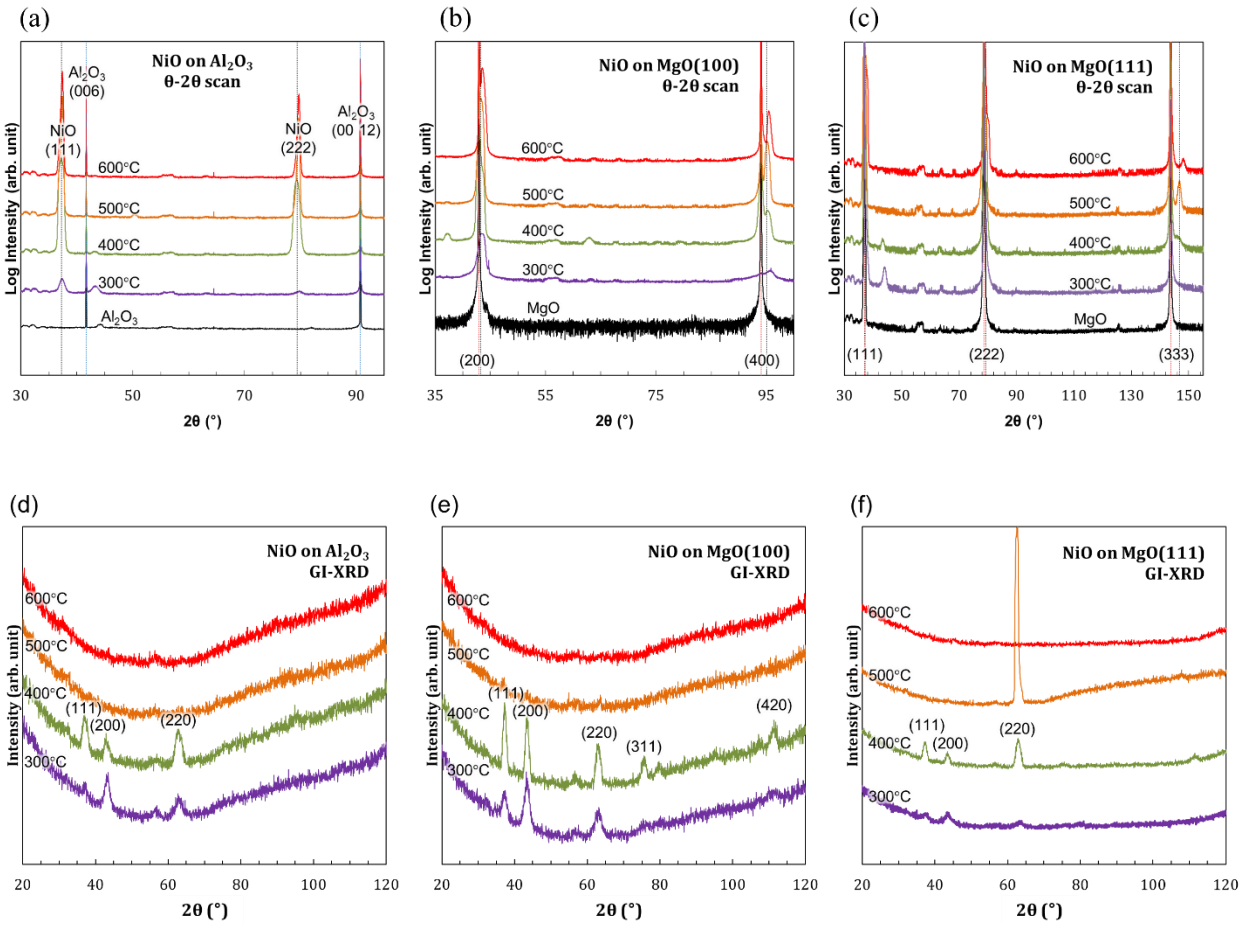

Figure 5.2 XRD θ-2θ patterns of the NiO films grown at various growth temperatures. (a) On Al_2O_3 substrates, the peaks at 37° and 79° for NiO(111) and NiO(222), respectively, indicate epitaxial growth toward NiO[111]; (b) On MgO(100), the peaks near 43° and 94° for NiO(100) and NiO(200), respectively, indicate cube-on-cube orientation relationship; (c) On MgO(111), overlaps of NiO and MgO diffraction peaks were observed near 37° and 79°, which belong to NiO(111) and NiO(222), respectively. The diffraction peaks of MgO(333) and NiO(333) were more widely separated and can be observed at 144° and 147°, respectively. At lower growth temperature, polycrystalline phases can be clearly observed in the GI-XRD patterns of (d) NiO films grown on Al_2O_3, (e) NiO films grown on MgO(100), and (f) NiO films grown on MgO(111).

The XRD θ-2θ patterns of NiO on the MgO(100) substrate are shown in Figure 5.2 (b). The diffraction patterns indicate that NiO was grown along NiO[100] direction on the MgO(100) substrate. Using the PDF from ICDD #45-946 and #47-1049 for MgO and NiO, respectively, peaks near 42°, 43°, 94°, and 95° were assigned to MgO(200), NiO(200), MgO(400), and NiO(400), respectively. Based on the evolution of peak intensity with increasing growth

temperature, in general, higher growth temperatures result in better-crystallized films. Although no peaks from other phases are evident in the θ-2θ pattern, the GI-XRD Figure 5.2 (e) reveals the presence of diffraction peaks from other NiO planes. The samples grown at 300 °C and 400 °C were polycrystalline, with diffractions from NiO(111), NiO(200), NiO(220), NiO(311), and NiO(420). No peaks were observed for samples grown at 500 °C and 600 °C. This indicates the formation of single-crystalline NiO at these temperatures. Cube-on-cube orientation relationship is expected in the growth of NiO on a MgO substrate, as they have similar crystal structures and lattice constants. Based on the PDF documents, the lattice constants of NiO and MgO are 4.1771 Å and 4.2112 Å, respectively, which results in a lattice mismatch of < 1%.

Observation of four diffraction peaks from NiO(220) in the XRD ϕ scans (Figure 5.3) further confirms that the films were grown in the cube-on-cube orientation relationship and without the formation of any twin defects. In this setup, because of the high similarity in the lattice constants, peaks from MgO(220) were simultaneously measured.

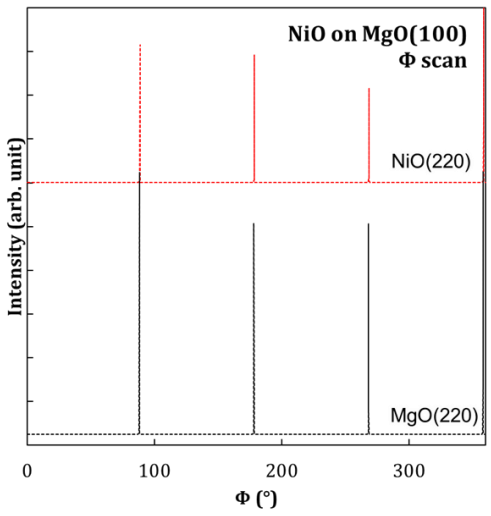

Figure 5.3 Typical XRD patterns (ϕ scan) of thin NiO film grown on MgO(220). Four diffraction peaks indicate that the film was grown without any twin defects.

Figure 5.2 (c) shows the XRD θ-2θ patterns of NiO on the MgO(111) substrate. Some of the MgO peaks overlap with the NiO peaks because of the similarities in the crystal structure and lattice constant, especially for the peak at 37°, which can be assigned to both MgO(111) and NiO(111). Nevertheless, the diffraction patterns of higher-angle planes were more widely separated and were used in analysis. Observation of these planes, i.e., NiO(222) and NiO(333) at 79° and 147°, respectively, confirms that NiO was grown in the NiO[111] direction on the MgO(111) substrate. Small-intensity peaks at 42° were visible in samples grown at 300 °C and 400 °C, and indicated the formation of polycrystalline films. Indeed, the GI-XRD patterns in Figure 5.2 (f) confirm that samples grown at 300 °C, 400 °C, and 500 °C were polycrystalline, with diffraction peaks from the NiO(111), NiO(200), and NiO(220) planes.

Single-crystalline NiO on MgO(111) was obtained only at 600 °C, based on the absence of diffraction peaks in the GI-XRD scan. The NiO(333) diffraction peak in film grown at 600 °C shifted toward a higher angle, compared with the film grown at 500 °C. This may be caused by lattice relaxation in thicker films. The thickness is 0.2 μm for the film grown at 600 °C, thinner than 0.7 μm for film grown at 500 °C. The thinner film (grown at 600 °C) grew pseudomorphically on an MgO substrate with a lateral tensile strain or vertical compressive strain, which results in a peak at a higher angle in the XRD pattern. In a thicker film (grown at 500 °C), lattice relaxation may have occurred, causing an increased interplanar spacing in the vertical direction and a peak shift toward a lower angle in the XRD pattern. A similar trend was also observed in the case of NiO films grown on MgO(100) substrates.

The ϕ scan, which was set to obtain diffractions from NiO(220), is shown in Figure 5.4 (a). Peaks from MgO(220) were simultaneously measured because of the high similarity in the lattice parameters. The samples grown at 300 °C, 500 °C, and 600 °C exhibit three peaks of NiO(220) that exactly match the three peaks of MgO(220), suggesting that the NiO were grown without the formation of any twin defects. However, the sample grown at 400 °C showed six diffraction peaks, suggesting the formation of twin structure.

5. 2. 2 Effects of the growth parameters on the formation of twin defects

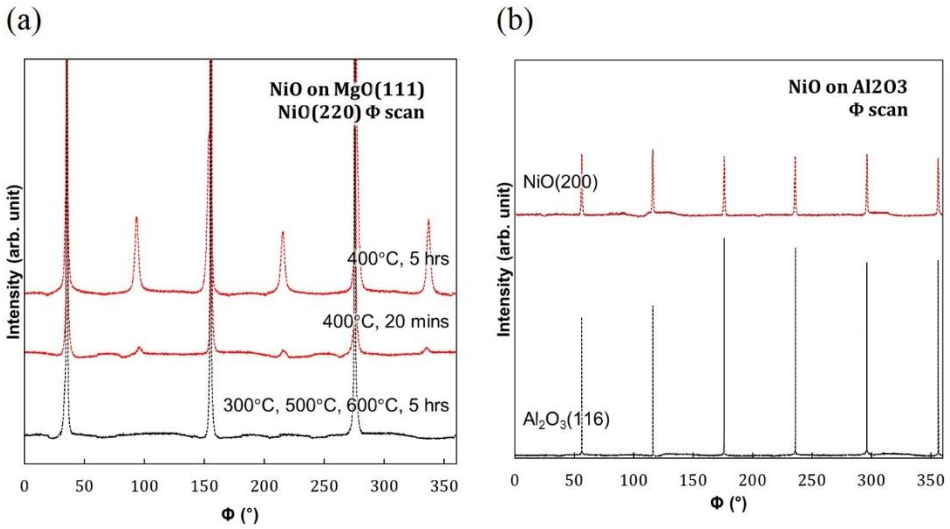

Figure 5.4 (a) XRD patterns (ϕ scan) of NiO film grown on MgO(111) at various growth temperatures. Both patterns of NiO grown at 400 °C for 5 hours and 20 minutes showed six peaks, which indicates the formation of twin defects; (b) XRD patterns (ϕ scan) of thin NiO film grown on Al_2O_3 at 500 °C for 20 minutes. Six diffraction peaks indicate the presence of twin defects in the thin NiO film.

The XRD analysis given above shows that there are two trends in twin defect formation, based on the choice of substrate material. On the Al_2O_3 substrates, the twin defects were not sensitive to the growth temperature and were observed in all of the samples (Figure 5.1). On the contrary, on the MgO(111) substrates, the twin defects were found only in samples grown at 400 °C. It is important to note that the film grown at this temperature was 1.4 μm thick, thicker than films grown at other growth temperatures (0.4 μm, 0.7 μm, and 0.2 μm thick for NiO grown

at 300 °C, 500 °C, and 600 °C, respectively). Considering the difference in film thickness, it is important to investigate the effect of film thickness in the formation of the twin structure as twin defects may be formed due to accumulated stress with increasing thickness.

To investigate whether the formation of twin defects is related to the thickness of the films, thin layers of NiO were grown on MgO(111) at 400 °C and on Al_2O_3 at 500 °C, both for 20 minutes. The thicknesses were estimated to be 90 nm and 44 nm on the MgO(111) and Al_2O_3 substrates, respectively. Figure 5.4 (a) and (b) show the XRD ϕ scan patterns of the thin NiO films grown on MgO(111) and Al_2O_3 substrates, respectively. Six diffraction peaks obtained in the pattern indicate presence of twin defects in both films. This result also suggests that the formation of twin defects was not affected by the film thickness in either of the substrates. It is then surmised that the twin defects may originate from the initial stacking of adatoms at the beginning of the growth.

To investigate whether the formation of twin defects may occur at the initial growth steps, models of the atomic structure for NiO films grown on Al_2O_3 and MgO(111) substrates were built based on the Vesta software[15], as shown in Figure 5.5. The orientations of each phase were aligned according to the COR obtained from the XRD analysis (Appendix B). By examining the arrangement of each metal to oxygen layer in the substrates, differences in the atomic arrangement between the cubic MgO and the rhombohedral Al_2O_3 can be observed. For the MgO substrate, only one kind of metal to oxygen arrangement can be observed, while in the Al_2O_3 substrate, two kinds of arrangements can be observed, as depicted in Figure 5.5 (a) and (b), respectively. One of the arrangements in the Al_2O_3 substrate has a similar construction to that of NiO (blue shade, dotted line), while the other arrangement has similar construction to that of twinned NiO (yellow shade, solid line). This alternating atomic arrangement may contribute to

the formation of twin defects at the initial growth step in the following manner. Assuming that the Al_2O_3 substrate has an oxygen-terminated surface, the arrangement of the first following metal and oxygen layers will follow the native sequence of the substrate. A layer of Al_2O_3 substrate would promote the growth of non-twinned NiO, while the subsequent layer would promote the growth of a twinned NiO film. By modeling a monolayer step on the surface of the substrate, as shown in Figure 5.5 (b), it is clear that the formation of twin defects may be promoted on the Al_2O_3 substrate. Moreover, it has been reported that island-type growth occurs in NiO grown on Al_2O_3[12]. On a surface with a monolayer step, some of these islands may grow in one lateral direction, while the others may grow in a different lateral direction, resulting in a pattern of twin defects in the XRD ϕ scan. Therefore, the formation of twin defects at the initial growth step may occur in NiO grown on an Al_2O_3 substrate because of the native atomic arrangement of the Al_2O_3 substrate. This is consistent with most works on NiO growth on Al_2O_3 substrates, which report the formation of twin-defect NiO[5,11–13,16,17].

An alternating arrangement of atoms does not exist in the MgO substrates, as shown in Figure 5.5 (a). Surface non-uniformity in the case of MgO may cause defects in the crystal but does not necessarily promote the formation of a twin structure, as in Al_2O_3. Instead, the formation of twin defects in NiO grown on a MgO substrate is strongly related to the growth temperature, possibly in the sense that growth at 400 °C would provide the appropriate amount of energy preferable for the crystal to form a specific defect, i.e., twin defects.

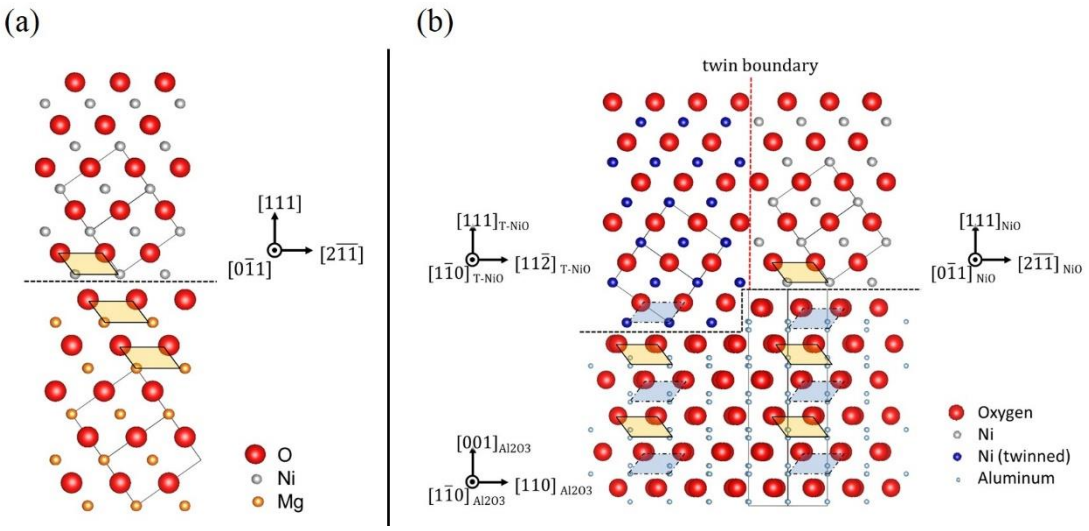

Figure 5.5 Visual model for formation of twin defects: (a) NiO(111) on MgO(111) substrate; (b) NiO(111) with twin defects on a monolayer step surface of an Al_2O_3 substrate.

5. 2. 3 Growth rate on various substrates

As shown in Figure 5.6, for all the substrates employed, the growth rate increased with increasing growth temperature, reaching a maximum at 400 °C, then decreasing with further increases in the growth temperature. The low growth rate at 300 °C indicates that the precursor was not fully decomposed at this temperature and the growth was kinetically limited. The precursors were fully decomposed at 400 °C, as indicated by the maxima in the growth rate, and the growth was probably diffusion-limited. However, at this temperature, adatoms did not have the energy required to move to energetically favorable sites, which results in the formation of polycrystalline NiO. As previously shown in the XRD results, at the lowest temperature (300 °C), no films on any of the substrates were well crystallized. With increasing growth temperature, adatoms have additional energy which is required to move to a more favorable site, enabling the formation of polycrystalline films and furthermore forming single-crystalline films at a specific substrate-dependent growth temperature. For films grown on Al_2O_3 and MgO(100), single crystals were formed at 500 °C and 600 °C, while on MgO(111), formation of single-

crystalline NiO took place only at 600 °C. The growth rate at the highest growth temperature, however, decreased because of the increased desorption of adatoms. The flat region, commonly observed in MOVPE growth, was not evident in the current growth. This is probably due to limited number of data and the high reactivity of oxygen. Nevertheless, these results suggest that the growth temperature is an important factor for optimizing the trade-off between the growth rate and the crystal quality.

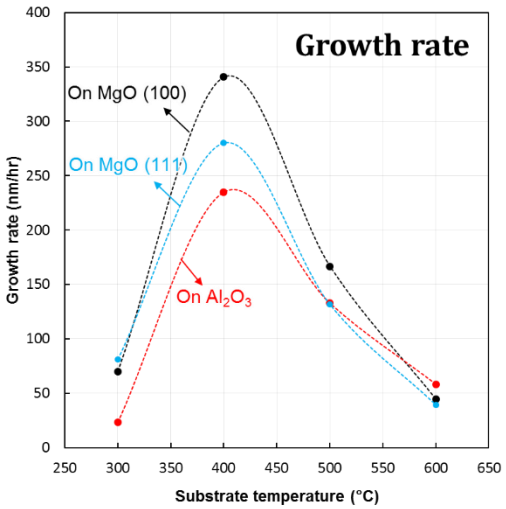

Figure 5.6 Growth rate of NiO films grown on different substrates at with respect to the growth temperature

5. 2. 4 Evolution of crystal quality with growth temperature

The evolution of crystal quality with increasing growth temperature was investigated by XRD rocking curve scans on the out-of-plane and asymmetric directions. The out-of-plane direction is perpendicular to the substrate (growth direction) while the asymmetric direction is not perpendicular to the substrate. Table 5.1 shows the planes that were used to evaluate the NiO crystal quality for each substrate. The full width at half maximum (FWHM) values of XRD out-of-plane rocking curve scans for films grown on Al_2O_3 are shown in Figure 5.7 (a). The FWHM

slightly decreased with increasing growth temperature up to 400 °C, then abruptly decreased at 500 °C. For the out-of-plane direction, the smallest FWHM was 0.099°, which was obtained from the 0.3-μm -thick film grown at 600 °C. Similar trend was found in the asymmetric direction. The obtained FWHM is larger than that of a 5-nm-thick NiO film deposited by ALD[12], but comparable to that grown by PA-MOVPE[6] and smaller than those deposited by PLD[16] and MOVPE[5]. For the asymmetric direction, the FWHM was 0.225°.

Table 5.1 The crystallographic planes used in the evaluation of NiO crystal quality with respect to the out-of-plane and asymmetric directions for each substrate.

Substrate	Out-of-plane	Asymmetric
Al_2O_3	NiO(111)	NiO(200)
MgO(100)	NiO(400)	NiO(420)
MgO(111)	NiO(222)	NiO(420)

For samples grown on MgO, planes of higher diffraction angles, i.e., NiO(222), NiO(400), and NiO(420), were particularly chosen because their peaks are better separated than those of MgO. Figure 5.7 (b) shows the trend of crystal quality for NiO grown on MgO(100) with respect to growth temperature. The out-of-plane FWHM slightly decreased from 300 °C to 400 °C, then abruptly decreased at 500 °C, in which single crystals were formed. In the out-of-plane direction, the smallest FWHM was 0.318°, which was obtained from the 0.8-μm-thick film grown at 500 °C. The obtained FWHM is comparable to those reported for NiO on MgO(100) deposited by ALD[12] and MOVPE[5]. In the asymmetric direction, the FWHM was 0.370°.

Figure 5.7 (c) shows the correlation between the out-of-plane FWHM and the growth temperature for NiO grown on MgO(111) substrates. In general, the FWHM increased with increasing growth temperature, indicating a degradation of crystal quality. In the out-of-plane direction, the smallest FWHM was 0.612°. In the asymmetric direction, the FWHM was 1.098°.

The dependences of the rocking curve's FWHM on the growth temperature for MgO(100) and MgO(111) substrates seem to be opposite. This may be related to a difference in the crystallinity of these NiO films. As previously discussed, the NiO films on MgO(111) which were grown at low temperature exhibit not only polycrystal structure but also twin structure, while those grown on MgO(100) at low temperature were polycrystal without any twin structures. Furthermore, due to higher surface energy of the NiO(111), the 3D growth is preferred in the NiO films grown on MgO(111) substrates, while the 2D growth is more dominant in the NiO films grown on MgO(100) substrates.[7]

5. 2. 5 Resistivity dependence on crystal quality

The effects of growth temperature and type of substrate material on the NiO film resistivity are shown in Figure 5.7. The resistivity and the FWHM of the XRD rocking curve scans (out-of-plane) were simultaneously plotted with respect to the growth temperature. Two trends of the resistivity dependence on the crystal quality can be observed based on the substrate used in the growth. For the samples grown on Al_2O_3, the resistivity was proportional to the out-of-plane FWHM (Figure 5.7 (a)). Conversely, for samples grown on MgO(100) and MgO(111) substrates, the resistivity was inversely proportional to the out-of-plane FWHM values (Figure 5.7 (b)). A similar yet weaker trend was observed in samples grown on MgO(111), as shown in Figure 5.7 (c).

It is well accepted that the conductivity in NiO is related to the presence of defects, i.e., the metal deficiency[6,11]. Ni vacancies in NiO have been reported to be doubly ionized, generating electron holes[18]. The NiO samples grown on Al_2O_3, experience a compressive stress because the coincident lattice parameter of the Al_2O_3 substrate is smaller. Epitaxy of these stressed films has

the tendency to form vacancies to accommodate the mismatch. Indeed, the asymmetric lattice parameters obtained by the XRD indicate that films are not fully relaxed. Therefore, the improved crystallinity promotes more vacancies, generates more carriers, and decreases the resistivity. Conversely, the NiO samples grown on MgO were under tensile strain because of a larger MgO lattice constant. Epitaxy of these strained films requires annihilation of vacancies to accommodate the mismatch. Therefore, the improved crystallinity promotes fewer vacancies, fewer carriers, and increases the resistivity.

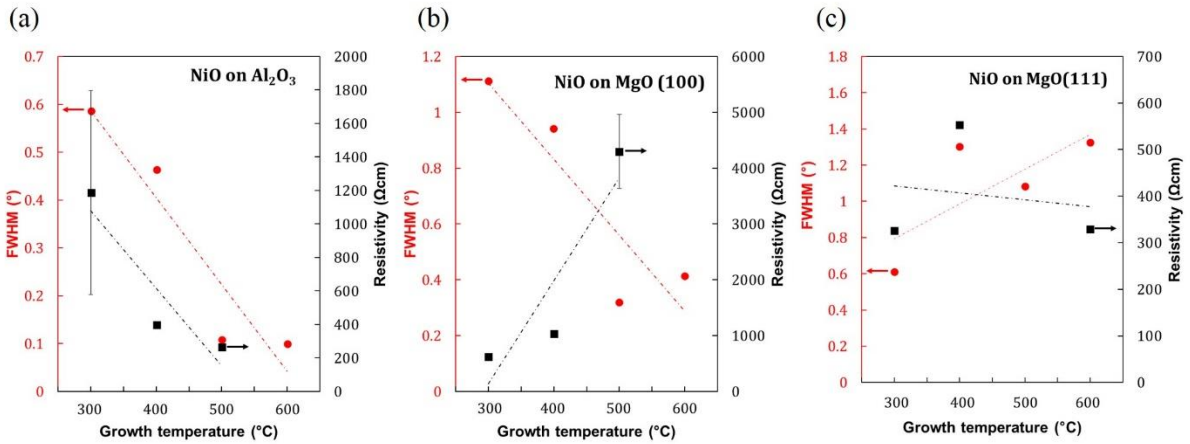

Figure 5.7 Resistivity and FWHM of the out-of-plane XRD rocking curve with respect to the growth temperature of NiO grown (a) on Al_2O_3, (b) on MgO(100), and (c) on MgO(111). The dash-dotted lines represent the linear trend line for each parameter and are intended as visual guides.

5. 3 Conclusions

Epitaxial NiO films have been grown by APMOVPE. Epitaxial NiO(111) films were grown on Al_2O_3(001) and MgO(111) substrates, while NiO(100) films were grown on MgO(100) substrates. For all of the substrates employed, the growth rate of the films was optimized at 400 °C, which can be accounted for by the full decomposition of the precursor. On MgO(100) and Al_2O_3 substrates, single-crystalline NiO(100) and NiO(111) were obtained at 500 °C, while on MgO(111) substrates, single-crystalline NiO(111) was obtained at 600 °C. For each substrate, selection of the growth temperature is important for optimizing the trade-off between growth rate and crystal quality. Substrate dependent characteristics were observed in the formation of twin structure. The native atomic arrangement of the Al_2O_3 surface was considered to be the cause for the formation NiO thin films with twin structure.

References

[1] E. Fujii, A. Tomozawa, H. Torii, and R. Takayama, Jpn. J. Appl. Phys. **35**, L328 (1996).

[2] B. Subramanian, M.M. Ibrahim, V. Senthilkumar, K. Murali, V. Vidhya, C. Sanjeeviraja, and M. Jayachandran, Physica B: Condensed Matter **403**, 4104 (2008).

[3] H.-L. Chen and Y.-S. Yang, Thin Solid Films **516**, 5590 (2008).

[4] M. Tyagi, M. Tomar, and V. Gupta, Materials Research Bulletin **66**, 123 (2015).

[5] A. Wang, J.A. Belot, and T.J. Marks, Journal of Materials Research **14**, 1132 (1999).

[6] H. Wang, G. Wu, X. Cai, Y. Zhao, Z. Shi, J. Wang, X. Xia, X. Dong, B. Zhang, Y. Ma, and others, Vacuum **86**, 2044 (2012).

[7] B. Warot, E. Snoeck, P. Baulès, J. Ousset, M. Casanove, S. Dubourg, and J. Bobo, J. Cryst. Growth **234**, 704 (2002).

[8] K. Oka, T. Yanagida, K. Nagashima, H. Tanaka, and T. Kawai, Journal of Applied Physics **104**, 013711 (2008).

[9] K. Uchida, K. Yoshida, D. Zhang, A. Koizumi, and S. Nozaki, AIP Advances **2**, 042154 (2012).

[10] T.M. Roffi, K. Uchida, and S. Nozaki, J. Cryst. Growth **414**, 123 (2015).

[11] T. Dutta, P. Gupta, A. Gupta, and J. Narayan, Journal of Applied Physics **108**, 083715 (2010).

[12] E. Lindahl, J. Lu, M. Ottosson, and J.-O. Carlsson, J. Cryst. Growth **311**, 4082 (2009).

[13] J.H. Lee, Y.H. Kwon, B.H. Kong, J.Y. Lee, and H.K. Cho, Cryst. Growth Des. **12**, 2495 (2012).

[14] J. Narayan and B. Larson, Journal of Applied Physics **93**, 278 (2003).

[15] K. Momma and F. Izumi, Journal of Applied Crystallography **44**, 1272 (2011).

[16] Y. Kakehi, S. Nakao, K. Satoh, and T. Kusaka, J. Cryst. Growth **237**, 591 (2002).

[17] C. Mocuta, A. Barbier, G. Renaud, Y. Samson, and M. Noblet, Journal of Magnetism and Magnetic Materials **211**, 283 (2000).

[18] C. Osburn and R. Vest, Journal of Physics and Chemistry of Solids **32**, 1331 (1971).

CHAPTER 6

MOVPE growth and characterization of cobalt doped NiO

Attempts to improve the p-type conductivity of NiO, especially by lithium doping, have been reported in the literature.[1,2] Substitution of nickel by monovalent atoms such as lithium enables the generation of uncompensated holes, thereby improving the p-type conductivity. Other methods of modifying the conductivity of NiO have also been reported, such as the post deposition annealing of sputter grown NiO[3] and ultraviolet laser irradiation of PLD grown NiO.[4] However, doping to produce n-type NiO is not yet well studied. We have attempted to produce n-type conductivity in NiO by incorporating cobalt to form $Co_xNi_{1-x}O$.

The effect of cobalt incorporation on the structural, electrical, and optical properties of $Co_xNi_{1-x}O$ films is of significant interest. The possibility of engineering the bandgap of $Co_xNi_{1-x}O$ films is also important, especially for the fabrication of devices with selective response in the UV region. $Co_xNi_{1-x}O$ films with cobalt composition ranging from x=0.01 to x=0.72 were grown on Al_2O_3 substrates at 500 °C in an atmospheric pressure metal organic vapor phase epitaxy (APMOVPE). The cobalt compositions of the obtained films were determined by energy dispersive X-ray spectroscopy (EDS). X-ray diffraction analysis (XRD) in $\theta 2\theta$ and ϕ scan modes and Raman spectroscopy were employed to determine the crystal structure of the films. Scanning electron microscopy (SEM) was used to analyze the surface morphology of the films. Bandgap energies were approximated from optical transmittance data measured by UV-vis-NIR transmittance spectroscopy. The resistivity of the films was measured by using the four point probe method, while their mobility and carrier concentration were investigated by using Hall effect measurements.

6. 1 Experimental details

Single crystalline $(001)_{Al_2O_3}$ substrates were used. Prior to growth, the substrates were degreased in an ultrasonic bath using acetone, ethanol, and deionized water for 10 min each. $Co_xNi_{1-x}O$ films were grown on the substrates by APMOVPE at 500 °C. Similar to the preceding chapters, Allyl(cyclopentadienyl) nickel ($C_8H_{10}Ni$) was used as the nickel precursor and was kept at 30 °C to obtain a vapor pressure of 0.84 torr. Bis(methylcyclopentadienyl) cobalt ($Co(CH_3C_5H_4)_2$) was used as cobalt precursor and was kept at 50 °C to obtain a vapor pressure of 0.3 torr. Pure O_2 gas was used as an oxygen source and N_2 was used as the carrier gas. The bubbling flow rates of each metal precursor were adjusted to obtain the desired cobalt composition. Growth times were adjusted to maintain the same total amount of precursors transported throughout all of the reactions. The resulting samples were $Co_xNi_{1-x}O$ with x of 0, 0.01, 0.02, 0.08, 0.17, 0.22, 0.35, 0.56, 0.72, and 1, as determined by EDS analysis. The thicknesses of the films varied from around 500 nm to 1300 nm as observed in the cross section images of the field emission scanning electron microscopy (FESEM).

The obtained samples were subjected to various analyses, including structural, optical, and electrical. The crystal structure and crystallographic orientation relationship between the $Co_xNi_{1-x}O$ film and the Al_2O_3 substrate were analyzed by XRD in θ-2θ, rocking curve, and ϕ configurations with Cu Kα radiation (λ=1.54 Å). Further structure and compositional analyses were performed by Raman spectroscopy. The optical transmittance of the films was measured using UV-vis-NIR spectroscopy. The resistivity of the samples was mainly measured by the four-point probe method and further confirmed with van der Pauw configuration Hall effect measurements. For Hall measurements, 500-nm-thick metal contacts consisting of Pt (100 nm), Ti (300 nm), and Au (100 nm) with an area of ~1 mm^2 were deposited on each corner of the

square sample. The conductivity type, carrier concentration, and mobility of the films were then investigated. All measurements were performed at room temperature.

6. 2 Results and discussions

6. 2. 1 Structural characterization

XRD analyses in θ-2θ scanning mode were conducted to determine the structure and phase of the samples. Consistent with discussion in the previous section, the NiO sample was grown towards the $[111]_{NiO}$ direction. The out-of-plane epitaxial relationship between the NiO film and the Al_2O_3 substrate is $[111]_{NiO}||[006]_{Al_2O_3}$ and the in-plane relationships are $[\bar{1}\bar{1}2]_{NiO}||[\bar{1}\bar{1}0]_{Al_2O_3}$ and $[2\bar{1}\bar{1}]_{Twinned\text{-}NiO}||[110]_{Al_2O_3}$.

Figure 6.1 shows that all the samples containing nickel (x=0 to x=0.72) exhibited peaks at 37° and 79°, indicating the existence of cubic phase NiO oriented towards $[111]_{NiO}$. The films also exhibit twinned structure oriented along the growth direction as indicated by the presence of six-fold symmetry in XRD ϕ scans (Figure 6.2). The NiO structure remained dominant in the samples with x=0 to x=0.08, as indicated by the narrow FWHM in Figure 6.3 and strong peaks. However, the structure of NiO was weakened at higher cobalt incorporation in the film, as indicated by peak broadening and intensity decrease. The effect of cobalt became greater in films with x=0.17 and x=0.22, the patterns of which exhibited a shift towards higher angle as well as FWHM broadening of the $(111)_{NiO}$ peak. The existence of additional 2θ peaks at about 38° and 82° and the series of 2θ peaks at 18°, 59°, and 110° observed for the samples with higher cobalt composition (x≥0.35) is indicative of phase separation. These peaks were attributed to either $NiCo_2O_4$ (ICDD #20-781) or Co_3O_4 (ICDD #42-1467). Further phase characterization could not be accomplished through XRD analysis owing to the similarity between the structural parameters

of $NiCo_2O_4$ and Co_3O_4. Hence, Raman scattering analysis was carried out to complement the XRD data, as described later.

High resolution ω-2θ scans normalized to the Al_2O_3 peak were carried out to investigate any peak shift caused by cobalt incorporation. As shown in Figure 6.4, the peak positions of the $Co_xNi_{1-x}O$ samples slightly shifted to lower values for cobalt compositions between x=0 and x=0.08, then shifted to higher values for higher cobalt compositions. The reason for this is as follows. The observed peak positions of the x=0 (NiO) sample were higher than those of the PDF data, indicating a smaller interplanar spacing than that expected for stoichiometric NiO. It is well known that as-deposited NiO may possess intrinsic defects comprising excess oxygen (nickel vacancies) allowing for p-type conductivity. Cobalt may have been incorporated in these nickel-vacant sites, resulting in a larger unit cell volume compared with that of as-deposited NiO that appeared as a slight peak shift towards lower angle in the XRD pattern. Both divalent and trivalent cobalt may exist in cases of nickel substitution,[6,7] and this may have caused the observed slight shift towards higher angle owing to their smaller ionic radii (0.69 Å, 0.65 Å, and 0.55 Å for Ni^{2+}, Co^{2+}, and Co^{3+}, respectively.[8] Films grown without any nickel exhibited peaks matching those of Co_3O_4 (PDF #42-1467).

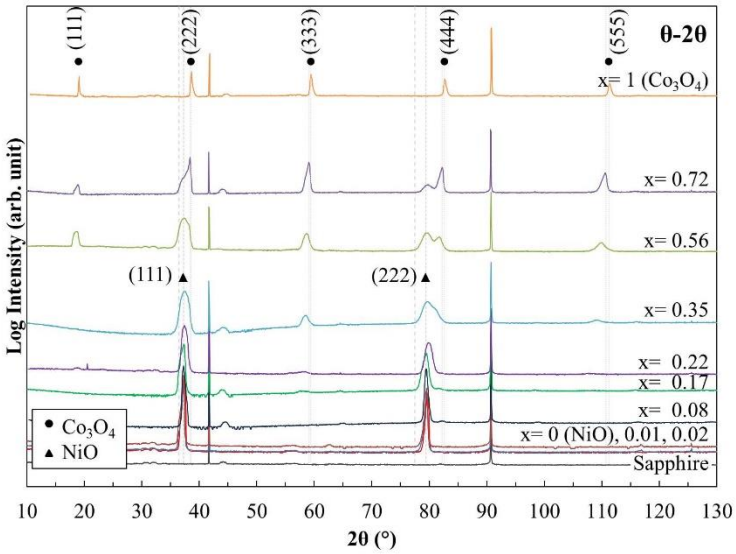

Figure 6.1 XRD θ-2θ scans of $Co_xNi_{1-x}O$ films. Samples with x=0 to x=0.72 showed peaks at 37° and 79°, which weakened with increasing cobalt composition. The additional peaks at about 38°, 82° and the series of peaks at 18°, 59°, and 110° observed at higher cobalt compositions (x≥0.35) are indicative of phase separation.

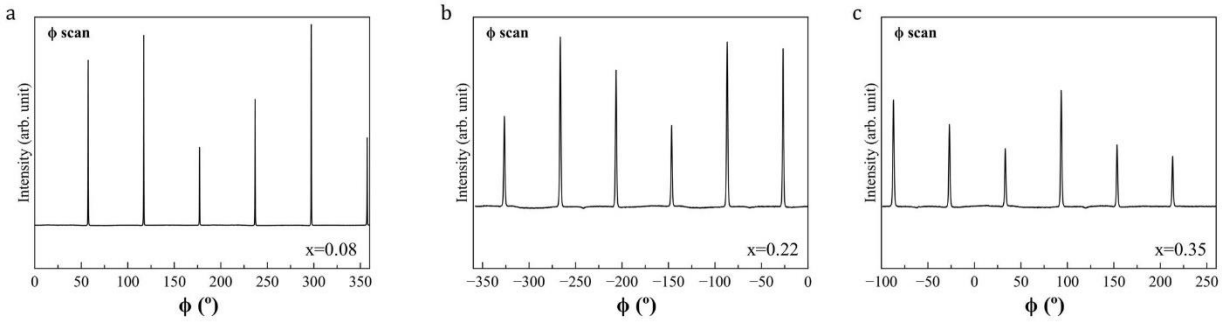

Figure 6.2 XRD ϕ scans of the $Co_xNi_{1-x}O$ samples of x=0.08 (a), x=0.22 (b), and x=0.35 (c) tilted 54.73° from the $(111)_{NiO}$ plane, satisfying the Bragg condition for the $(200)_{NiO}$ plane. All samples exhibited six-fold symmetry, indicative of a twinned structure oriented along the growth direction.

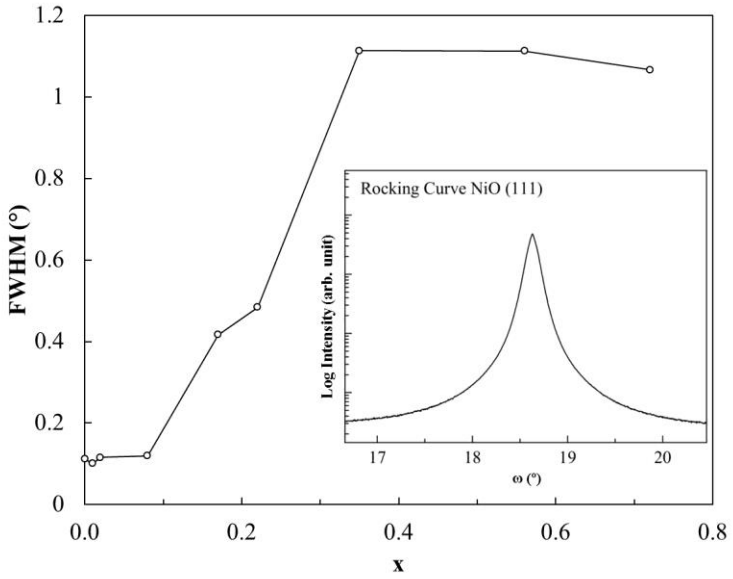

Figure 6.3 FWHM of $(111)_{NiO}$ obtained from rocking curve scan data. The FWHM of $(111)_{NiO}$ became broader as cobalt composition increased. Inset shows ω scan result for the x=0 (NiO) sample, showing a FWHM of 0.112°.

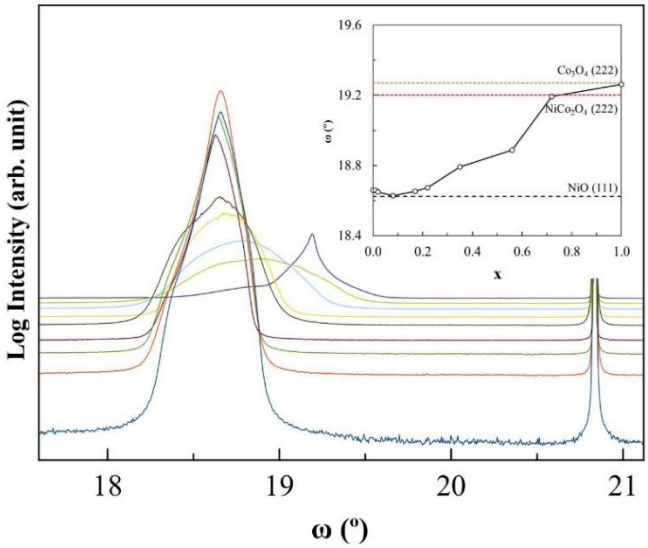

Figure 6.4 High resolution ω-2θ scan normalized to the Al_2O_3 peaks. The NiO peak position slightly shifted to lower value for x=0 to x=0.08, then shifted to higher value for higher cobalt compositions. The inset presents the trend in peak position with cobalt composition.

Raman scattering spectra of the samples are shown in Figure 6.5. The lowermost plot is the Raman spectra of Al_2O_3, which exhibits peaks at 400, 560, and 740 cm^{-1}. The peaks overlapping these Al_2O_3 peaks were not considered in further analysis. The peaks observed for the x=0 (NiO) film at about 560, 925, 1100, and 1500 cm^{-1} match those of the literature[9] representing the LO,

TO+LO, 2LO, and 2M modes. The TO and 2TO modes expected at about 440 and 740 cm^{-1} could not be observed owing to the presence of overlapping Al_2O_3 peaks.

At low cobalt composition (x=0.01), no significant change in Raman spectra was observable. At x=0.02, two effects could be observed. First, the magnon excitation mode of NiO (2M) weakened and shifted towards lower wavenumbers. Second, additional Raman peaks appeared at about 520 and 620 cm^{-1}, which could be addressed to CoO phase.[10] The existence of Co-O bonding is expected when cobalt enters the NiO lattice, in agreement with the XRD analysis. Thus, although the coexistence of NiO and CoO structures (for low cobalt concentrations) could not be determined from the XRD data, their different vibrational modes made it possible to observe them by Raman spectroscopy, as explained above.

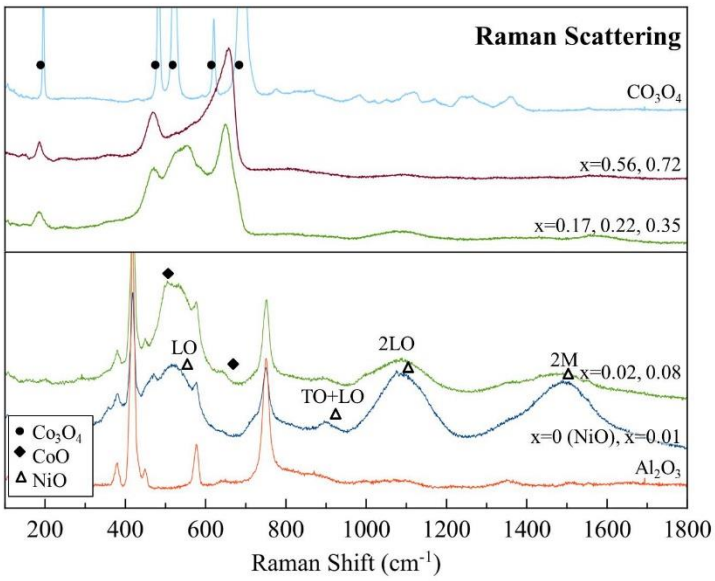

Figure 6.5 Raman Scattering of $Co_xNi_{1-x}O$ films. The spectrum obtained for the x=0.02 sample was assigned to NiO and CoO, while the spectra of higher cobalt compositions (x=0.17 to x=0.72) were attributed to nickel-cobalt oxides.

The Raman spectra of samples with x=0.17 to x=0.72 were identical to those reported in the literature for nickel-cobalt oxide series,[11,12] with two major Raman peaks at about 465 and 655 cm^{-1} and a minor one at about 551 cm^{-1}. The peak at about 550 cm^{-1} in our samples, however,

appeared to be sensitive towards the cobalt composition. The peak at about 650 cm^{-1} has previously been attributed to a vibrational mode involving oxygen atom in octahedral sites in the spinel lattice.[13] Thus, it is suggested that the slight shift of this peak towards higher frequency in samples of higher cobalt composition was caused by Co^{3+} substitution of Ni^{2+} in the octahedral sites of the spinel structure. Co^{3+} substitution of Ni^{2+} at spinel octahedral sites would cause structural distortion owing to the smaller ionic radius of Co^{3+} and shorter bond length, thus causing a shift of the Raman band to higher frequency. With the XRD results, it can be confirmed that the phases present in this sample were NiO and the series of nickel-cobalt oxides ($NiCo_2O_4$), not Co_3O_4. Consistent with the XRD results, the Raman peaks of samples grown without any nickel, at 480, 519, 617, and 689 cm^{-1}, match those reported for Co_3O_4 in the literature.[14,15]

Table 6.1 Observed phases in relation to cobalt composition of the films.

Cobalt Composition x	Phases			
	NiO	CoO	$Co_xNi_{1-x}O$	$NiCo_2O_4$
0	v			
0.01	v	v		
0.02	v	v		
0.08	v	v		
0.17			v	
0.22			v	
0.35	v			v
0.56	v			v
0.72	v			v

As summarized in Table 6.1, cobalt was incorporated in the NiO lattice for $Co_xNi_{1-x}O$ samples with $x \leq 0.08$. Formation of $Co_xNi_{1-x}O$ alloy occurred at x=0.17 and x=0.22. Attempts to incorporate a greater proportion of cobalt resulted in phase separation into NiO and $NiCo_2O_4$ phases, as evidenced for the samples with x=0.35–0.72. The $NiCo_2O_4$ phase became dominant when x=0.72, while samples grown without nickel were found to be Co_3O_4.

6. 2. 2 Appearance and surface morphology

The x=0 (NiO) film was optically clear and grayish green in color. The films darkened with increasing cobalt composition up to x=0.22; beyond this, the films were black. The film grown without any nickel (Co_3O_4) was slightly lighter in color, dark brown, and was optically clear.

The surface morphology of the $Co_xNi_{1-x}O$ films differed depending on their cobalt composition, as observed from the SEM images presented in Figure 6.6. Coalesced tetrahedrons with poorly-defined boundaries were found in the x=0 (NiO) and x=0.08 films. This result supports the structural analysis by XRD and Raman spectroscopy, which found that the NiO phase remains with cobalt incorporation at low x. The films with higher cobalt composition exhibited segregated grains with more distinct boundaries. Segregation of the grains was most likely introduced by the phase separation of NiO and $NiCo_2O_4$. It was also evident that some of the pyramids were rotated by 60°, indicative of twinned $(111)_{NiO}$ in the films.

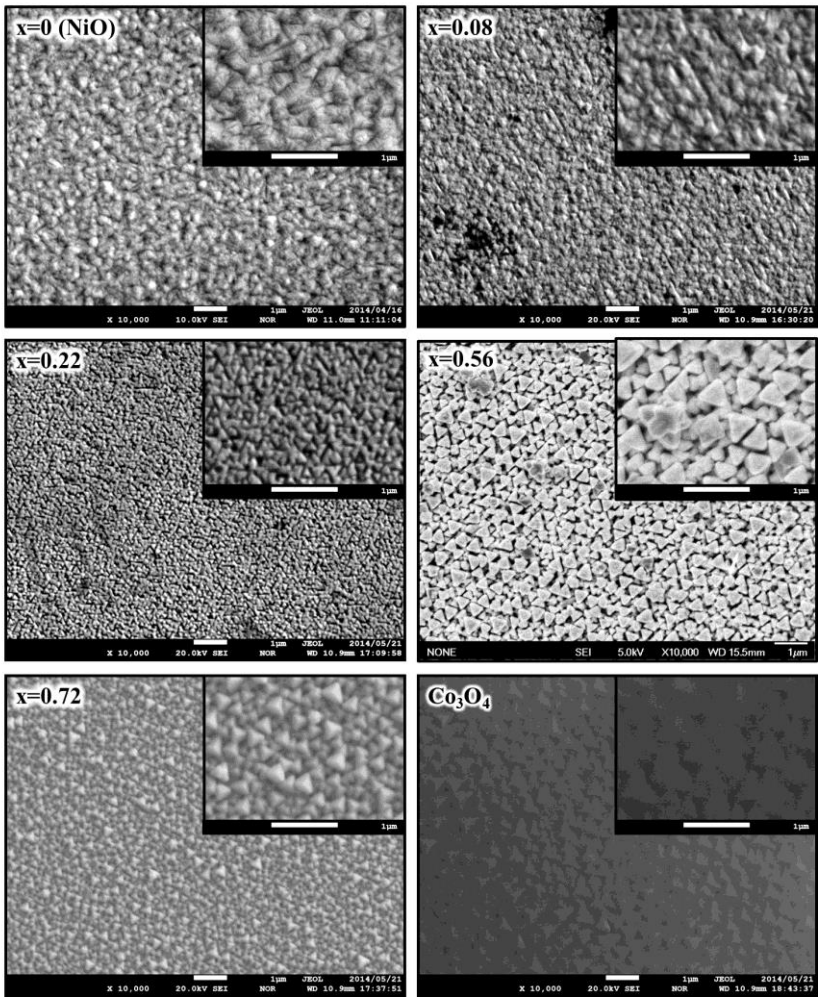

Figure 6.6 SEM micrographs of $Co_xNi_{1-x}O$ samples taken at 10 000× magnification. Coalesced tetrahedrons with poorly-defined boundaries were found in x=0 (NiO) and x=0.08 films, while films with higher cobalt composition exhibited segregated grains with more distinct boundaries. Insets show micrographs taken at 20 000x magnification. All white bars represent 1μm length.

6. 2. 3 Optical transmittance

UV-vis-NIR transmittance spectroscopy measurements were performed to investigate the optical characteristics and approximate the bandgap of the films. The optical transmittance spectra of the $Co_xNi_{1-x}O$ samples in the wavelength range 200–800 nm at room temperature are given in Figure 6.7. As shown in the inset, the x=0 (NiO) film showed high transparency in the visible region, indicated by an 88% average transmittance for the 800-nm-thick film. Although the transmittance decreased with increasing cobalt composition, it was maintained at a relatively

high percentage up to x=0.17, i.e., 71% average transmittance for a 700-nm-thick film. These transmittance results agree well with the XRD analysis of the films; incorporation of cobalt at this level introduced defect sites, indicated by the slight change in structural parameters, which scatter incident light. More significant deterioration in the transparency of NiO films was observed in the case of lithium doping[16] owing to its larger difference in ionic radius. Beyond x=0.17, transmittance in the visible region dropped as a result of enhanced alloy formation.

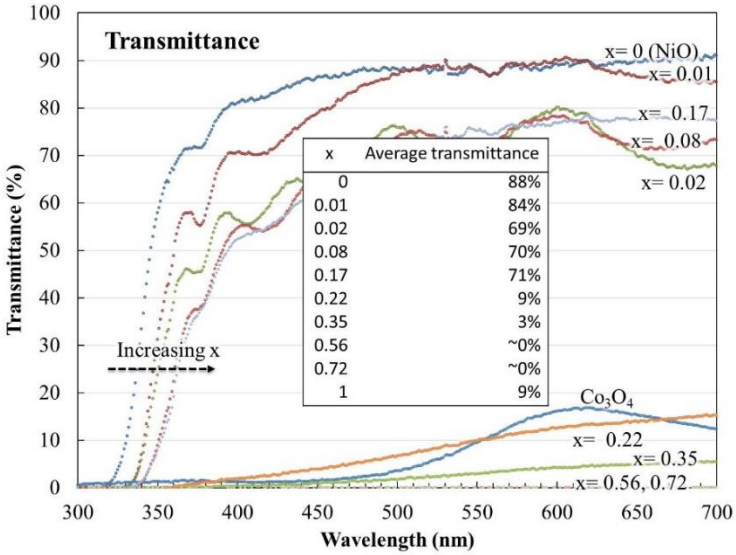

Figure 6.7 Transmittance spectra of the $Co_xNi_{1-x}O$ samples. The highest transmittance of 88% was obtained for the 800-nm-thick x=0 (NiO) film. The incorporation of cobalt decreased the transmittance and caused red shift (towards higher wavelength) of the fundamental absorption edge.

A shift of fundamental absorption edge towards lower wavelength (redshift) was observed with increasing cobalt composition, which is related to a decrease in optical bandgap. The optical bandgaps of the films were approximated using the classical relation for near edge optical absorption in semiconductors.

$$\alpha h\nu^2 = A(h\nu - E_g),$$

where A is a constant, α is the absorption coefficient, and hν and Eg represent the incident photon energy and the semiconductor bandgap energy, respectively. Plots of $(\alpha h\nu)^2$ against (hν)

for the $Co_xNi_{1-x}O$ films are presented in inset of Figure 6.8. The bandgap decreased from 3.7 eV to 2.35 eV with increasing cobalt composition. The relation between cobalt composition and optical band gap can be approximated by Vegard's law:

$$E_{g,\,Co_xNi_{1-x}O} = \mathrm{x}\,E_{g,\,Co_3O_4} + (1-x)E_{g,NiO} - b\,x\,(1-x),$$

where E_g is the bandgap of the respective materials and b is the bowing parameter, a measure of the non-linearity of the bandgap as a function of composition. Although phase separation occurred for cobalt composition x=0.35, 0.56, and 0.72, which makes the use of Vegard's law unusual in this case, the approximation is well suited and useful for further compositional design of CoNiO, especially by the current growth method. The optical bandgap and cobalt composition was well fitted by a bowing parameter of 3.5, as shown in Figure 6.8. It should be noted that the bandgaps of x=0.56 and x=0.72 films were not shown because of undefined absorption edges due to low transmittance. However, the approximated bandgap for x=0.35 where phase separation occurs could be determined and was found to follow Vegard's law. The incorporation of cobalt into NiO to form $Co_xNi_{1-x}O$ was therefore able to decrease the bandgap of NiO considerably. This result indicates that selective UV-region response materials based on NiO can be manufactured using the present APMOVPE system by controlling the cobalt composition.

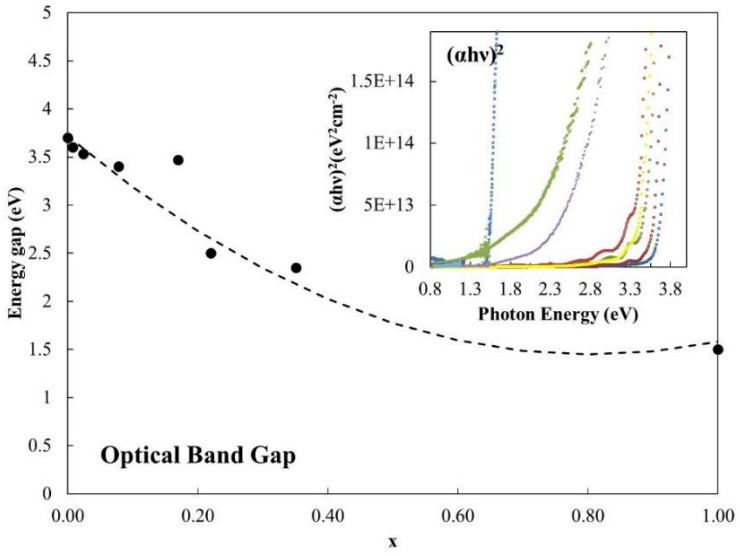

Figure 6.8 Approximated bandgap energy as a function of cobalt composition follows Vegard's law with bowing parameter 3.5. Data points for x=0.56 and x=0.72 are not available since these films are not transparent. Inset shows the plot of $(\alpha h\nu)^2$ to $(h\nu)$.

6. 2. 4 Electrical property

Four-point-probe measurements were conducted at room temperature to investigate the resistivity of the samples as a function of cobalt composition (Figure 6.9). The resistivity of the films was found to decrease from 960 Ωcm to 0.006 Ωcm with increasing cobalt composition from x=0 to x=0.72. However, the resistivity did not change much from x=0 to x=0.08.

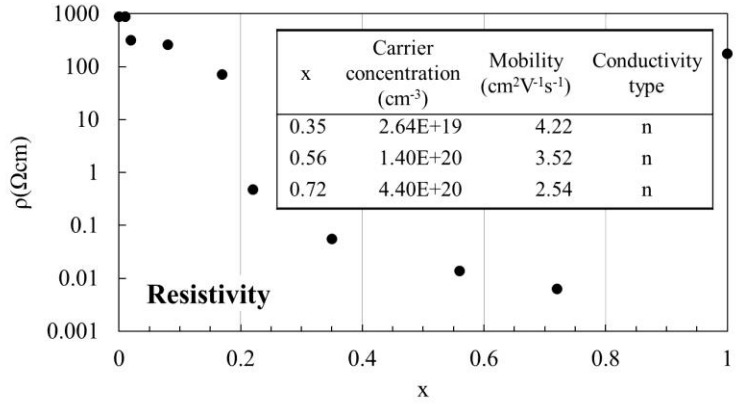

Figure 6.9 Change in resistivity of the films with cobalt composition. The resistivity decreased from 960 to 0.006 Ωcm with increased cobalt composition from x=0 to x=0.72

The effect of the cobalt composition on the resistivity can be explained by the carrier generation process in $Co_xNi_{1-x}O$. Although stoichiometric NiO is an insulator, it is well known that defects play major role in the conductivity of NiO. As-deposited NiO may contain native defects of excess oxygen which create cation deficiencies on NiO lattice sites that cause the generation of holes, as expressed by the following Kröger–Vink notation.

$$\frac{1}{2}O_2(g) \leftrightarrows v''_{Ni} + O_o^{\mathrm{X}} + 2h^+$$

Two holes are generated to maintain charge neutrality. Consistently, defects in NiO may also reverse its conductivity type. It is reported that NiO may obtain n-type conductivity by certain treatments such as post deposition annealing, ultraviolet irradiation, and varied oxygen pressure,[3,4,17] which cause oxygen deficiency. The defect reaction can be expressed as follows, assuming complete ionization.

$$\mathrm{O_O^X} \leftrightarrows \mathrm{v_O^{\bullet\bullet}} + 2\mathrm{e}' + \frac{1}{2}\mathrm{O_2(g)}$$

In the case of cobalt incorporation into NiO films, it is reported that cobalt ions exist in the nickel lattice as Co^{2+} and Co^{3+}.[6,7] While the substitution of homovalent cobalt (Co^{2+}) for nickel in the lattice may not result in any carrier generation, incorporation of aliovalent Co^{3+} may generate carriers according to the following Kröger–Vink notation.

$$Co_2O_3 \leftrightarrows 2Co_{Ni}^{\bullet} + 2O_0^X + 2e' + \frac{1}{2}O_2(g)$$

Two electrons are generated for every two trivalent cobalt ions substituting nickel in the lattice. Therefore, the decreasing resistivity observed with increasing cobalt composition is caused by increased carrier generation in $Co_xNi_{1-x}O$. This is well in agreement with the Hall

measurement results (inset of Figure 6.9) of the $Co_xNi_{1-x}O$ samples with x=0.35, 0.56, and 0.72, which exhibit n-type conductivity. It is surmised that trivalent cobalt in $Co_xNi_{1-x}O$ alloy behaved as a donor. We note that caution is needed in interpreting the Hall results owing to possible magnetic influence of the sample. It has been reported that although Co_3O_4 and NiO are p-type semiconductors, the conductivity of $Ni_{1-x}Co_xO_{4/3}$ was not clear, with Hall measurements showing both p- and n-type conductivity in the same sample.[18] Indeed, in our Hall measurements only three samples exhibited consistent n-type conductivity, while the conductivity type of the rest of the samples could not be determined.

The effect of the Co concentration on the resistivity can be explained by the result of the structural analysis. For the Co concentrations up to 7.9 %, the CoO is epitaxially grown on some NiO grains without affecting NiO. Stoichiometric CoO is highly resistive but becomes conductive if it has Co deficiency, like stoichiometric NiO. Therefore, the carrier concentration and mobility are not much affected by the Co doping. However, when the Co concentration is as high as 35.1 %, $NiCo_2O_4$ alloys are formed. In the alloy, Co is ionized to Co^{3+}. A trivalent Co replacing a divalent Co provides a free electron as a donor. Indeed, the Hall measurement shows that the sample with a Co concentration of 35.1 % has the n-type conductivity with a carrier concentration of 6.15×10^{19} cm^{-3} and a mobility of 2.4 $cm^2V^{-1}s^{-1}$. These values are comparable to previously reported n-type NiO by other workers.[3]

6. 3 Conclusions

Successful growth of $Co_xNi_{1-x}O$ with a wide cobalt composition range of x=0.01 to x=0.72 has been achieved using APMOVPE. All the films grown had a preferred orientation towards $[111]_{NiO}$ with a twinned structure. Cobalt was well incorporated in the NiO structure up to x=0.08, $Co_xNi_{1-x}O$ alloys were formed from x=0.17 to x=0.22, and phase separation of NiO and $Co_xNi_{1-x}O$ occurred when $x \geq 0.35$. Films grown without any nickel were found to be composed of Co_3O_4. The bandgap of the $Co_xNi_{1-x}O$ films decreased with increasing cobalt composition, and controllable bandgap engineering in the UV region was demonstrated. The resistivity of the films also decreased with increasing cobalt composition, reaching a minimum of 0.006 Ωcm. Based on Hall measurements, some of the samples exhibited n-type conductivity and this has been related to the existence of trivalent cobalt as a donor in the NiO structure.

References

[1] T. Dutta, P. Gupta, A. Gupta, and J. Narayan, Journal of Applied Physics **108**, 083715 (2010).

[2] W.-L. Jang, Y.-M. Lu, W.-S. Hwang, and W.-C. Chen, Journal of the European Ceramic Society **30**, 503 (2010).

[3] M. Tyagi, M. Tomar, and V. Gupta, Journal of Materials Research **28**, 723 (2013).

[4] P. Gupta, T. Dutta, S. Mal, and J. Narayan, Journal of Applied Physics **111**, 013706 (2012).

[5] K. Uchida, K. Yoshida, D. Zhang, A. Koizumi, and S. Nozaki, AIP Advances **2**, 042154 (2012).

[6] G. Natu, P. Hasin, Z. Huang, Z. Ji, M. He, and Y. Wu, ACS Applied Materials & Interfaces **4**, 5922 (2012).

[7] Y. Gou, X. Liang, and B. Chen, J. Alloys Compd. **574**, 181 (2013).

[8] J.A. Dean, *Lange's Handbook of Chemistry* (McGraw Hill Book Co., New York, NY, 1985).

[9] N. Mironova-Ulmane, A. Kuzmin, I. Sildos, and M. Pärs, Central European Journal of Physics **9**, 1096 (2011).

[10] H.C. Choi, Y.M. Jung, I. Noda, and S.B. Kim, The Journal of Physical Chemistry B **107**, 5806 (2003).

[11] G. Calin, M. Irimia, C. Scarlat, M. Purica, F. Comanescu, and F. Iacomi, in *Semiconductor Conference (CAS), 2010 International* (2010), pp. 387–390.

[12] C.F. Windisch Jr, G.J. Exarhos, and S.K. Sharma, Journal of Applied Physics **92**, 5572 (2002).

[13] C.F. Windisch, K.F. Ferris, G.J. Exarhos, and S.K. Sharma, Thin Solid Films **420**, 89 (2002).

[14] H. Zhou, L. Chen, V. Malik, C. Knies, D.M. Hofmann, K.P. Bhatti, S. Chaudhary, P.J. Klar, W. Heimbrodt, C. Klingshirn, and others, Physica Status Solidi (a) **204**, 112 (2007).

[15] V. Hadjiev, M. Iliev, and I. Vergilov, Journal of Physics C: Solid State Physics **21**, L199 (1988).

[16] Y.H. Kwon, S.H. Chun, and H.K. Cho, Journal of Vacuum Science & Technology A **31**, 041501 (2013).

[17] R. Molaei, R. Bayati, and J. Narayan, Cryst. Growth Des. **13**, 5459 (2013).

[18] C.F. Windisch, G.J. Exarhos, K.F. Ferris, M.H. Engelhard, and D.C. Stewart, Thin Solid Films **398**, 45 (2001).

[19] R. Mossanek, I. Preda, M. Abbate, J. Rubio-Zuazo, G. Castro, A. Vollmer, A. Gutiérrez, and L. Soriano, Chemical Physics Letters **501**, 437 (2011).

[20] T. Dutta, P. Gupta, A. Gupta, and J. Narayan, J. Phys. D. Appl. Phys. **43**, 105301 (2010).

[21] J. Haber and L. Ungier, J. Electron Spectros. Relat. Phenomena **12**, 305 (1977).

[22] H. Rooksby and M. Vernon, British Journal of Applied Physics **17**, 1227 (1966).

CHAPTER 7

MOVPE growth of iron doped NiO

Nickel oxide is well known as a wide bandgap material with high transparency and conductivity which makes it suitable for various device applications i.e. transparent conducting oxides, UV LEDs, and sensors. However, its functionalities are still limited by understanding of its doping mechanism, hence the lack of n-type NiO. The substitution of Fe ions into the Ni lattice may elucidate the mechanism of doping in NiO for different ionization states, namely Fe^{+2} Fe^{+3}, etc. The Fe^{+3} substitution of Ni^{2+} may introduce electrons which will alter the conductivity of NiO. Furthermore, the addition of iron into NiO forms $Ni_{1-x}Fe_xO$, which was reported as a diluted magnetic semiconductor exhibiting ferromagnetism at room temperature, makes NiO more attractive.[1–4] This chapter comprises the growth and characterization of NiO with Fe using Al_2O_3(001) and MgO(100) substrates. The effects of the substrate and Fe concentration on the structure, optical, and electrical properties are analyzed in detail.

7. 1 Experimental details

$Ni_{1-x}Fe_xO$ thin films were grown for 3 hours at 500°C in an atmospheric-pressure MOVPE system with a typical growth time of 3 hours. Allyl(cyclopentadienyl) nickel ($C_8H_{10}Ni$) and Bis(methylcyclipentadienyl)iron ($(CH_3C_5H_4)_2Fe$) were employed as the precursors for Ni and Fe, respectively. Two type of substrates were used for the growth: Al_2O_3(001) and MgO(100). The Fe concentrations in the films were varied by adjusting the Fe precursor flow rates to 15, 30, and 50 sccm while keeping the same Ni precursor flow rate of 100 sccm. These samples for 15, 30, and 50 sccm are referred to as Fe-1, Fe-2 and Fe-3, respectively. The Fe concentrations of the

films Fe-1, Fe-2 and Fe-3 were determined by wavelength dispersive x-ray spectroscopy (WDS) and were shown in Table 7.1. The difference between the Fe incorporations for two types of substrates is not much significant to discuss.

Table 7.1 Fe concentrations (at. %) of the films with respect to the substrates as indicated by WDS

Substrate	Fe-1 (Fe at. %)	Fe-2 (Fe at. %)	Fe-3 (Fe at. %)
MgO	1.4	2.1	4.8
Al_2O_3	1.3	2.6	3.8

To investigate the structural properties of the samples, various configurations of X-ray diffraction (XRD) measurements with Cu Kα radiation (λ = 1.54 Å) were performed. The crystal structure was investigated by θ-2θ and ω-2θ scans. Surface images obtained by field-emission scanning electron microscopy (FE-SEM) were taken to study the morphology of the samples. The effects of the Fe concentrations on the transparency in the visible wavelength range were studied by optical transmittance measurement using a UV-vis-NIR spectroscopy system. The obtained spectra were also analyzed to estimate bandgaps of the films with different Fe concentrations. The resistivity of all samples was measured using a four-point prober and a Hall measurement system with the van der Pauw resistivity measurement. All of the measurements were carried out at room temperature.

7. 2 Results and discussions

7. 2. 1 Crystal structure and epitaxial relationship

Figure 7.1 shows the XRD patterns for films grown on MgO substrates. Single crystal film was formed for undoped NiO as shown in the lowermost pattern of Figure 7.1 (a). As indicated by multi-diffraction peaks in the rest of XRD patterns of Figure 7.1 (a), all the Fe-doped NiO

films grown on MgO substrates were polycrystalline. Diffraction peaks of the NiO (222) and NiO (400) were observed in Figure 7.1 (a) with the NiO (400) peak having the strongest intensity. This suggests that all the films grown on the MgO substrate consist of the NiO phase with the [100] preferred growth orientation. The ω-2θ scan plots in Figure 7.1 (b) show a shift of NiO (400) peak position toward the higher diffraction angle with the increased Fe concentration. This shift indicates that the lattice constant decreases with the increased Fe concentration. The effective ionic radii of the Fe^{2+} (0.61 Å) and Fe^{3+} (0.55 Å) in the octahedral coordination are smaller than that of the Ni^{2+} (0.69 Å).[5] Therefore, the Ni substitution by Fe decreased the lattice constant.

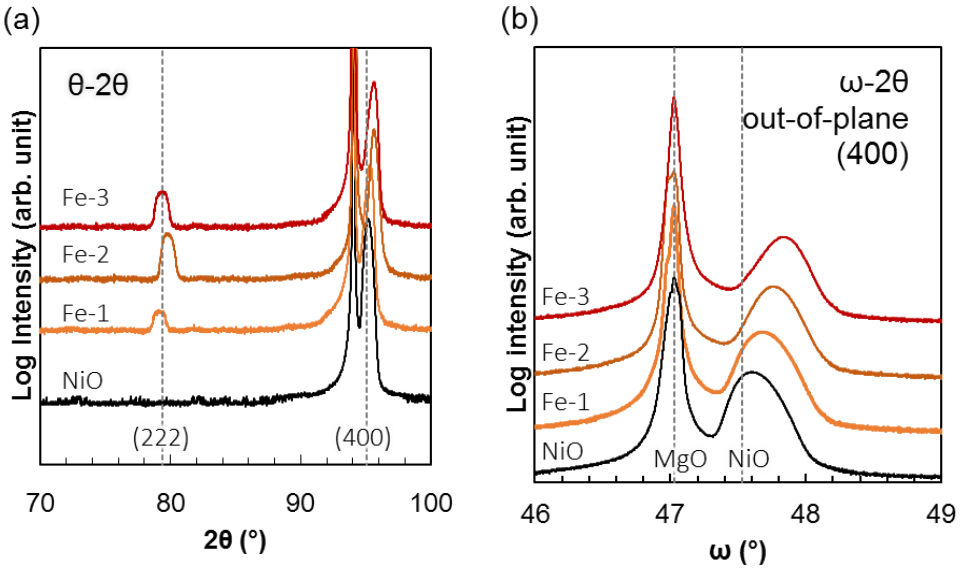

Figure 7.1 X-ray diffraction patterns of films grown using the MgO substrates (a) in the θ-2θ mode and (b) in the ω-2θ mode.

For the films grown on the Al_2O_3 substrates, the NiO phases with the [111] preferred growth orientation are observed in Fe-1, as indicated by a strong-intensity peak of NiO(111) at 37° in Figure 7.2 (a). In Fe-2 and Fe-3, the NiO-related diffraction peaks as well as the spinel $NiFe_2O_4$-related diffraction peaks are observed. The diffraction peak of the $NiFe_2O_4$ appears as a shoulder of the NiO(200) peak. It seems that both NiO and $NiFe_2O_4$ phases are present in the NiO films

with higher Fe concentrations. The ω-2θ scan plots in Figure 7.2 (b) show that the NiO(111) peak position do not shift with the increased Fe concentrations. This indicates that the lattice constant is not affected by incorporation of Fe with concentrations which means that Fe does not substitute Ni. A difference in Ni substitution by Fe between MgO and Al_2O_3 substrates may be explained by different stresses during the growth. The NiO films grown on Al_2O_3 substrates experienced a compressive stress due to a smaller Al_2O_3 lattice constant, while the NiO films grown on MgO substrates experienced a tensile strain due to a larger MgO lattice constant.

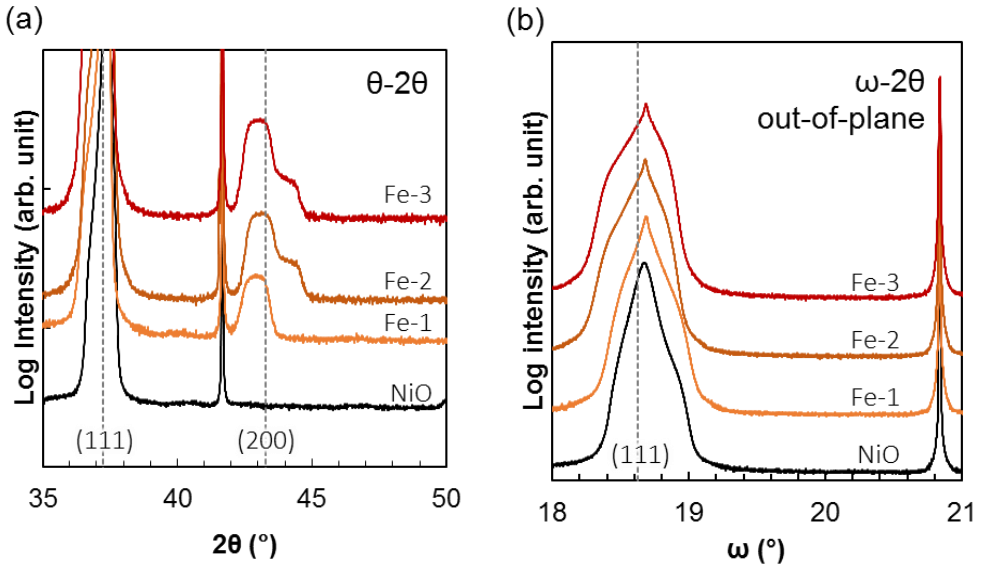

Figure 7.2 X-ray diffraction patterns of films grown using the Al_2O_3 substrates (a) in the θ-2θ mode and (b) in the ω-2θ mode.

The effect of different Fe concentration on the preferred orientation of the films is evaluated based on the orientation factor or texture coefficient which is defined as follows.[6–8]

$$F_{abc} = \frac{P - P_0}{1 - P_0}$$

$$P_0 = \frac{\sum I_{R,abc}}{\sum I_{R,hkl}}, P = \frac{\sum I_{abc}}{\sum I_{hkl}}$$

where F_{abc} is orientation factor for plane of interest (abc), P_0 is the ratio of the sum of intensities of family of planes (abc) to the sum of intensities of all planes for a textured sample, P is the same ratio for a randomly oriented sample. An F_{abc} of 1 indicates a complete preferred orientation into (abc) while F_{abc} of 0 or less indicates no texturing into (abc). The ICDD database for NiO (#47-1049) and the obtained XRD θ-2θ patterns between 30° to 100° were used to determine P_0 and P, respectively. The values for F_{111} and F_{100} were found to be less than 0 for films grown on MgO and Al_2O_3, respectively. On MgO and Al_2O_3, the films were grown with preferred orientation into NiO [100] and NiO [111], respectively, as indicated by F_{100} and F_{111} in Figure 7.3. It was also observed that the effect of Fe concentration on the texture is less significant for films grown on Al_2O_3. This is possibly because Fe does not substitute Ni in films grown on Al_2O_3, which is consistent with previous discussions.

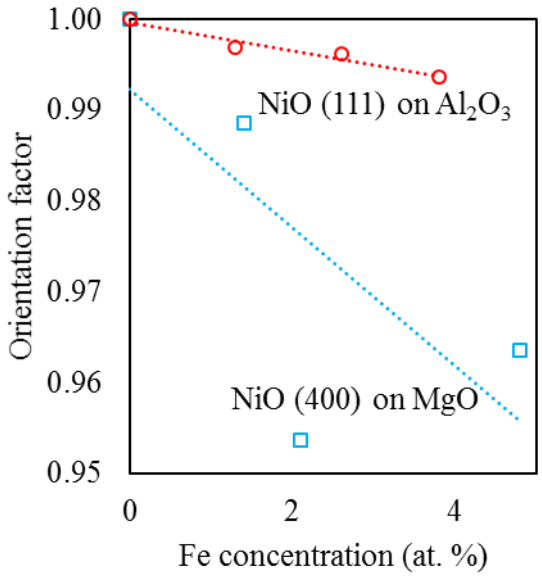

Figure 7.3 Fe concentration and substrate dependence of the orientation factor. Dashed lines are linear trend lines for each substrates and are intended as visual guides.

Although the $NiFe_2O_4$-related diffraction peaks are absent in the XRD pattern of the films grown on MgO substrates and those are absent in the XRD pattern of Fe-1 on an Al_2O_3 substrate,

their Raman spectra clearly show presence of $NiFe_2O_4$ phase (Figure 7.4). The Raman peaks of $NiFe_2O_4$ were reported at 483, 574, and 703 cm^{-1}.[4,9] It seems that $NiFe_2O_4$ nanoparticles are contained in all of the NiO films grown on the MgO substrates and even in the film with a very low Fe concentration on the Al_2O_3.

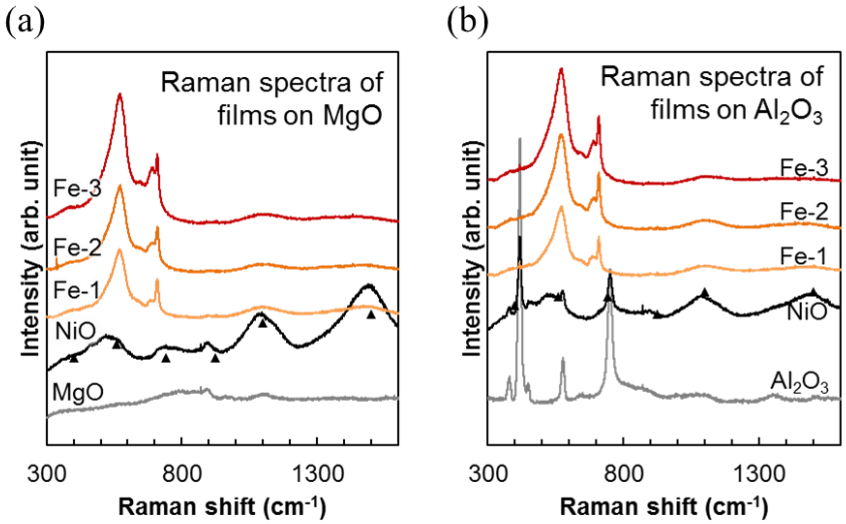

Figure 7.4 Raman spectra of the $Ni_{1-x}Fe_xO$ films grown on (a) MgO and on (b) Al_2O_3 substrates.

7. 2. 2 Surface morphology

The SEM images of surface morphologies of the samples are shown in Figure 7.5. The layer-by-layer growth was expected for undoped NiO on MgO substrates because of a small lattice misfit (<1%)[10], and single-crystalline NiO films with smooth surface morphology were reported by other deposition methods.[11,12] However, the surface of undoped NiO in Figure 7.5 has facets of mixed regular tetrahedrons and pyramids. They may have been formed by dislocations generated when the film thickness surpassed the critical thickness (film thickness is ~0.48 μm).[13] The surface morphology of Fe-1 is not much different from that of the undoped NiO. In contrast to the film grown on an MgO substrate, coalesced regular tetrahedrons were seen in undoped NiO grown on the Al_2O_3 substrate, suggesting typical growth along the [111] direction on a

hexagonal substrate.[13–16] A higher incorporation of Fe disturbs the growth of NiO and causes smaller domains of NiO and $NiFe_2O_4$ phases for both substrates.

The grain size decreases with the increased Fe concentration. The grain size in Fe-1 and Fe-2 on the MgO substrates appear to be larger than those on Al_2O_3 substrates. The growth seems to be disturbed by an incorporation of Fe with higher concentrations, and the phases of NiO and $NiFe_2O_4$ grow three dimensionally on both types of substrates. This is consistent with the XRD result. The presence of impurities may disturb the nucleation process, i.e. the so called filling of the neck or the grain growth in the area between the coalescing islands.[17] This results in incomplete coalescence, which is indicated by smaller grain sizes.

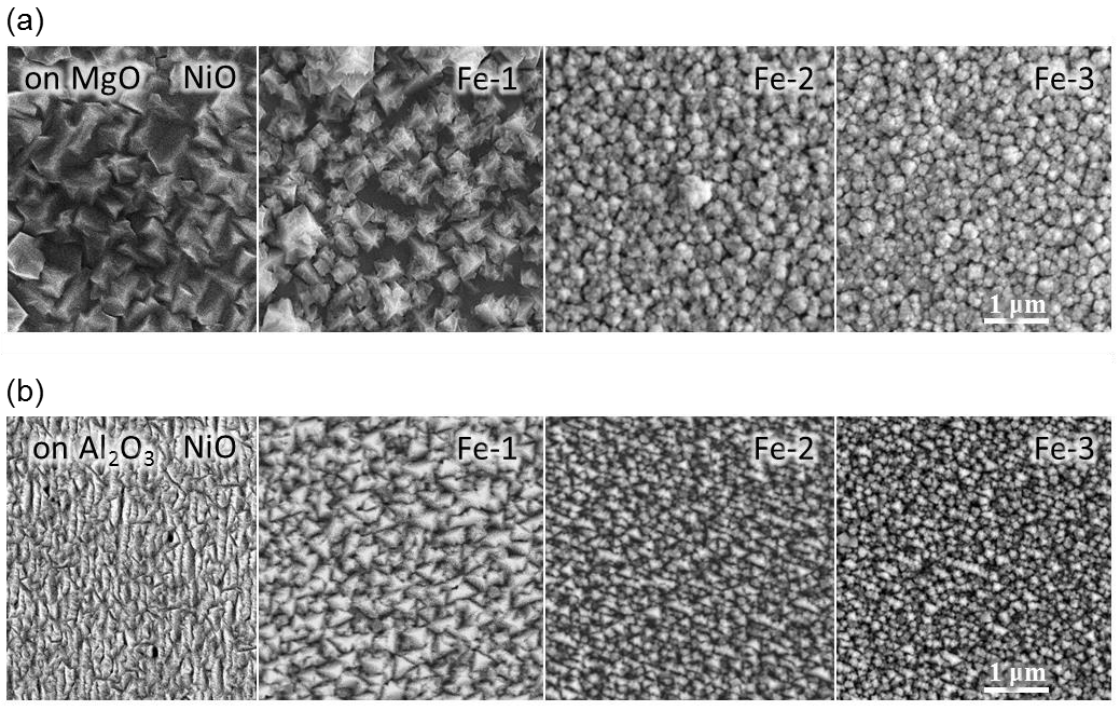

Figure 7.5 FE-SEM images of the film surface grown (a) on MgO and (b) on Al_2O_3 substrates. The white scale bars represent 1 µm length.

7. 2. 3 Optical and electrical properties

The optical transmittance spectra of the $Ni_{1-x}Fe_xO$ samples in the wavelength range 200–800 nm at room temperature are shown in Figure 7.6. The transmittances of films grown on MgO substrates (Figure 7.6 (a)) decreased with the increased iron concentration, while the transmittances of those grown on Al_2O_3 substrates (Figure 7.6 (b)) were not significantly affected by the iron concentration. In the figures, typical transmittances of single crystal NiO films are shown as black open circle. Table 7.2 summarizes the transmittance-measurement results and film thicknesses.

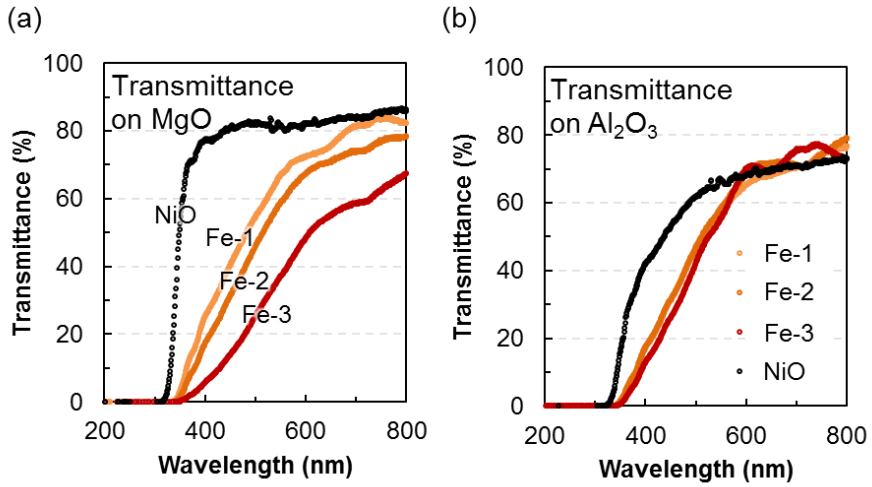

Figure 7.6 Transmittance spectra of the $Ni_{1-x}Fe_xO$ samples grown on (a) MgO substrate and (b) Al_2O_3 substrate.

These transmittance results are well explained by the structural and compositional analyses made for the results of the XRD and Raman spectroscopy. Fe substituted Ni in the films grown on MgO substrates, and the substitution resulted in the altered lattice constant. This may have caused the decreased transmittance. In films grown on Al_2O_3 substrates, Fe did not substitute Ni but formed $NiFe_2O_4$ nanoparticles. Therefore, the Fe incorporation did not cause any change in the lattice constant or the transmittance.

Table 7.2 Average transmittance in the visible wavelength region (390-700 nm) and thickness for different Fe concentrations in each substrates.

Film	MgO substrate		Al_2O_3 substrate	
	Visible transparency (%)	Thickness (μm)	Visible transparency (%)	Thickness (μm)
Fe-1	59.5	0.58	50.9	0.63
Fe-2	52.3	0.57	50.1	0.64
Fe-3	34.5	0.62	52.5	0.63

The optical bandgaps were extracted from the transmittance spectra for each Fe concentration using the following equation,

$$\alpha h\nu^2 = A\left(h\nu - E_g\right)$$

where A is a constant, α is the absorption coefficient, and hν and Eg represent the incident photon energy and the semiconductor bandgap energy, respectively. Plots of $(\alpha h\nu)^2$ vs. (hν) for the $Ni_{1-x}Fe_xO$ films are shown in Figure 7.7. Figure 7.7 (a) shows a significant decrease of the bandgap from 3.5 eV to 3.3 eV with the increased Fe concentration for the films grown on MgO substrates. The decrease of bandgap is consistent with bandgaps of iron oxide compounds which were reported to be ~l, ~2.2, and ~0.1 eV for wustite (FeO), hematite (Fe_2O_3), and magnetite Fe_3O_4, respectively.[18–20] The change in the bandgap energy is much less significant for the films grown on Al_2O_3 substrate, as seen in Figure 7.7 (b).

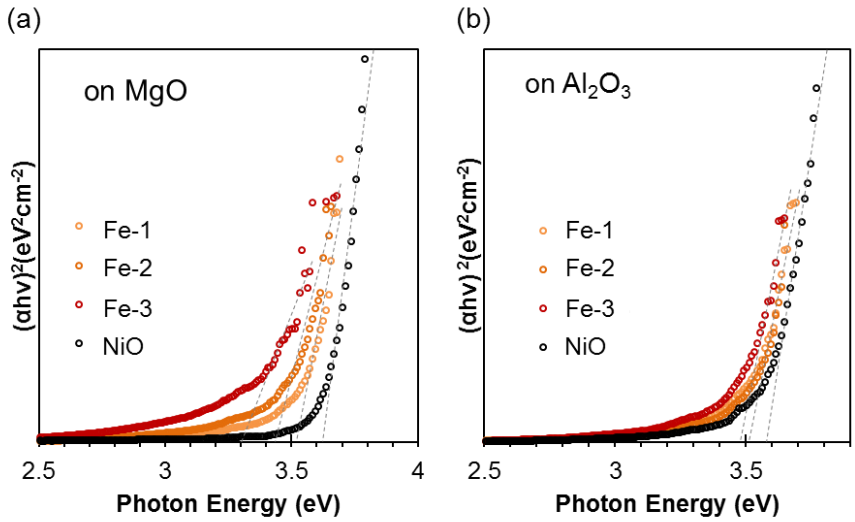

Figure 7.7 Estimated bandgap energy for $Ni_{1-x}Fe_xO$ samples grown on (a) MgO substrate and (b) Al_2O_3 substrate.

Four-point-probe measurement was carried out at room temperature to study the resistivity of the sample as a function of Fe concentration. The resistivities of the Fe-doped NiO films were out of the measurement range for all Fe concentrations and both types of substrates. The effect of Ni substitution by Fe on the resistivity may be caused by deteriorated crystal quality from single-crystal for undoped NiO to polycrystal for Fe-doped NiO films. The increased resistivity can also be related to a defect-related carrier compensation which is speculated as follows. It is well accepted that the as-deposited NiO film contains native defects of excess oxygen, which create cation deficiencies on the NiO lattice and produce holes. It is likely that substitution of Ni by Fe^{3+}causes annihilation of holes and hence increases the resistivity. This process is described by the following reaction.

$$Fe_2O_3 + 2h^{\bullet} \leftrightarrows 2Fe_{Ni}^{\bullet} + 2O_0^X + \frac{1}{2}O_2(g)$$

As shown above, two holes are annihilated for every two trivalent Fe ions substituting Ni.

7. 3 Conclusions

$Ni_{1-x}Fe_xO$ thin films were grown by MOVPE on two types of substrates: Al_2O_3 (001) and MgO (100). The introduction of iron affected the growth of NiO in a different way for the substrates to be used. The NiO films were grown in the [111] direction on Al_2O_3(001) substrates. In the films, Fe did not substitute Ni but formed nanocrystals of $NiFe_2O_4$. This was clearly observed by XRD and Raman measurements. Consistently, the transmittance and estimated bandgap were not affected by the Fe concentration. In contrast to the films grown on Al_2O_3 substates, Iron substituted Ni in the films grown on MgO(100) substrates. The Ni substitution by Fe in the NiO lattice decreased the transparency and optical bandgap energy with the increased Fe concentration. It also increased the resistivity by crystal quality deterioration or possible defect-related carrier compensation i.e. annihilation of preexisting holes.

References

[1] P. Mallick, C. Rath, R. Biswal, and N. Mishra, Indian Journal of Physics **83**, 517 (2009).

[2] J. Wang, J. Cai, Y.-H. Lin, and C.-W. Nan, Applied Physics Letters **87**, (2005).

[3] Y.-H. Lin, J. Wang, J. Cai, M. Ying, R. Zhao, M. Li, and C.-W. Nan, Physical Review B **73**, 193308 (2006).

[4] S. Liu, J. Jia, J. Wang, S. Liu, X. Wang, H. Song, and X. Hu, Journal of Magnetism and Magnetic Materials **324**, 2070 (2012).

[5] J.A. Dean, *Lange's Handbook of Chemistry* (McGraw Hill Book Co., New York, NY, 1985).

[6] C. Wang, B. Cheng, S. Wang, H. Lu, Y. Zhou, Z. Chen, and G. Yang, Thin Solid Films **485**, 82 (2005).

[7] C.Z. Yuan, Z.W. Min, and L. Jiang, Materials and Structures **21**, 329 (1988).

[8] F. Lotgering, Journal of Inorganic and Nuclear Chemistry **9**, 113 (1959).

[9] J. Landon, E. Demeter, N. İnoğlu, C. Keturakis, I.E. Wachs, R. Vasić, A.I. Frenkel, and J.R. Kitchin, Acs Catalysis **2**, 1793 (2012).

[10] B. Warot, E. Snoeck, P. Baulès, J. Ousset, M. Casanove, S. Dubourg, and J. Bobo, Applied Surface Science **177**, 287 (2001).

[11] K. Oka, T. Yanagida, K. Nagashima, H. Tanaka, and T. Kawai, Journal of Applied Physics **104**, 013711 (2008).

[12] Y. Kokubun, Y. Amano, Y. Meguro, and S. Nakagomi, Thin Solid Films (2015).

[13] T.M. Roffi, S. Nozaki, and K. Uchida, J. Cryst. Growth **451**, 57 (2016).

[14] A. Wang, J.A. Belot, and T.J. Marks, Journal of Materials Research **14**, 1132 (1999).

[15] T.M. Roffi, K. Uchida, and S. Nozaki, J. Cryst. Growth **414**, 123 (2015).

[16] C. Mocuta, A. Barbier, G. Renaud, Y. Samson, and M. Noblet, Journal of Magnetism and Magnetic Materials **211**, 283 (2000).

[17] P.B. Barna and M. Adamik, in *Science and Technology of Thin Films* (World Scientific Publishers New Jersey, 1995).

[18] F. Schrettle, C. Kant, P. Lunkenheimer, F. Mayr, J. Deisenhofer, and A. Loidl, The European Physical Journal B **85**, 1 (2012).

[19] B. Gilbert, C. Frandsen, E. Maxey, and D. Sherman, Physical Review B **79**, 035108 (2009).

[20] L. Blaney, Lehigh Review **15**, 33 (2007).

CHAPTER 8

Conclusions and outlook

In this study the growth of high quality NiO by MOVPE has been established. Growth of single crystalline NiO film was achieved by optimization of important growth parameters including the precursor ratio, the type of substrate, and the growth temperature. The effects of each growth parameters on the film properties were investigated and discussed.

The increase of precursor ratio (O_2/Ni) has improved the supersaturation level which enhance nucleation and grain growth as indicated by the more oriented structure and less variation of interplanar spacing. Furthermore, the improved crystallization in high O_2/Ni ratio leads to growth of more uniform films with smoother surface as confirmed through AFM measurement. It was also found that the increase of O_2/Ni ratio decreased the porosity of the film which decreased the resistivity by means of grain boundary scattering. The possibility of having a more non-stoichiometric film is also considerable in growth using high O_2/Ni ratio. Improved transmittance confirms the better crystallinity of the films.

The use of different substrates showed significant effects on the growth of NiO thin films by MOVPE. Epitaxial NiO(111) films were grown on Al_2O_3(001) and MgO(111) substrates, while NiO(100) films were grown on MgO(100) substrates. On MgO(100) and Al_2O_3 substrates, single-crystalline NiO(100) and NiO(111) were obtained at 500 °C, while on MgO(111) substrates, single-crystalline NiO(111) was obtained at 600 °C. For all of the substrates employed, the growth rate of the films was optimized at 400 °C, which can be accounted for by the full decomposition of the precursor. For each substrate, selection of the growth temperature is

important for optimizing the trade-off between growth rate and crystal quality. The formation of twin defects in NiO showed a dependency on the substrate material. The use of MgO substrates has prevented the formation of twin structure commonly found in growth using Al_2O_3 substrates. The growth temperature dependence of twin defect formation was observed in NiO(111) grown on MgO(111), in which twin defects were found only in films grown at 400 °C. Comparison between the twinned NiO(111) on Al_2O_3 and on MgO(111) showed that even a small non-uniformity of the Al_2O_3 surface can lead to the growth of twinned domains because of the native atomic arrangement of Al_2O_3. Different trends in resistivity with respect to crystal quality were observed.

The mechanism of doping and its role in the control of the carrier transport and conductivity of the NiO thin film have been studied by cobalt and iron doping. The heterovalent ions of Co^{3+} and Fe^{3+} were found to affect the electrical property of the film. The defect-controlled carrier generation in NiO is used to explain the difference in film resistivity upon doping. It is found that cobalt doping decreased the resistivity of NiO and films with high cobalt concentration possessed n-type conductivity. Films lowly doped with cobalt did not show degradation in crystallinity with single phase of NiO whereas higher cobalt doping causes the occurrence of multiphase of NiO, and nickel-cobalt-oxide compounds. Conversely, iron doping induced an increase of resistivity even at very low doping concentration. Iron doping was also found to inhibit the grain growth of NiO which resulted in polysrystalline films. The effect of different substrate materials was also confirmed in Fe-doped NiO films.

Continuous development in metal oxides and especially NiO is important in uncovering the fundamental aspects as well as application of novel devices, i.e. transparent electronics and ReRAM. In the future, efforts should be focused on further growth optimization, development of

NiO-related device process, and device fabrication of NiO. Growth optimization in MOVPE can be carried out, for example, by using buffer layer and two step growth, among others. Complete device process for NiO should be developed to allow the fabrication of devices based on NiO and other metal oxides. Novel devices with interesting performance can be expected from the development of NiO.

Appendix

A) Interplanar spacing

NiO (bunsenite)

PDF #47-1049 Cubic			a= 4.1771 Å λ=1.540598		
d	Int	hkl	2θ	psi relative to (111)	psi relative to (200)
2.412	61	111	37.25	0.00	54.74
2.089	100	200	43.28	54.74	0.00
1.4768	35	220	62.88	35.26	45.00
1.2594	13	311	75.42	29.50	25.24
1.2058	8	222	79.41	0.00	54.74
1.0443	4	400	95.06	54.74	0.00
0.9583	3	331	106.99	22.00	46.51
0.934	7	420	111.12	39.23	26.57

$NiCo_2O_4$

PDF #20－781 Cubic (spinel type)			a= 8.11 Å λ=1.540598	
d	Int	hkl	2θ	psi relative to (111)
4.69	14	111	18.91	
2.869	25	220	31.15	35.26
2.447	100	311	36.70	29.50
2.342	10	222	38.40	
2.029	25	400	44.62	54.74
1.656	8	422	55.44	
1.562	30	511,333	59.10	38.94
1.434	45	440	64.98	35.26
1.372	2	531	68.31	
1.23	16	533,622	77.55	
1.171	4	444	82.27	
1.136	2	711, 551	85.39	
1.084	6	642	90.57	
1.056	25	553, 731	93.68	
1.014	14	800	98.87	

α-Al_2O_3 (Corundum)

PDF #46 - 1212 Rhom. (Hex)			a= 4.7587 Å, c= 12.9929 Å λ=1.540598	
d	Int	hkl	2θ	psi relative to (111)
3.4797	45	012	25.58	57.61
2.5508	100	104	35.15	38.24
2.3795	21	110	37.77	90.00
2.1654	2	006	41.67	0.00
2.0853	66	113	43.35	61.22
1.9643	1	202	46.17	72.40
1.7401	34	024	52.55	57.61
1.6016	89	116	57.49	42.31
1.5467	1	211	59.73	83.16
1.511	14	018	61.30	21.51
1.4045	23	214	66.52	64.38
1.3737	27	300	68.21	90.00
1.336	1	125	70.41	59.06
1.2756	2	208	74.29	38.24
1.2392	29	1010	76.86	90.00
1.2343	12	119	77.22	31.25
1.1932	1	217	80.41	50.00
1.1897	2	220	80.70	90.00
1.16	1	306	83.21	57.61
1.1472	3	223	84.35	74.64
1.1386	<1	131	85.14	84.97
1.1257	2	312	86.35	80.02
1.1242	3	128	86.50	46.20
1.099	9	0210	88.99	
1.0827		006(2)	90.70	

Co_3O_4

PDF #42-1467 Cubic			a= 8.083719 Å λ=1.540598	
d	Int	hkl	2θ	psi relative to (111)
4.667	19	111	19.00	0
2.858	34	220	31.27	35.2644
2.437	100	311	36.85	29.4962
2.334	9	222	38.54	0
2.021	19	400	44.81	54.7356
1.6501	8	422	55.66	
1.5557	29	511, 333	59.36	0
1.429	34	440	65.24	35.2644
1.3664	2	531	68.63	
1.2782	2	620	74.12	

1.2328	7	533	77.34	
1.2187	4	622	78.41	
1.1668	2	444	82.63	0
1.1319	1	711	85.77	
1.0802	3	642	90.98	
1.0524	9	731	94.10	
1.0105	3	800	99.33	
0.9527	2	660	107.91	
0.9334	6	751, 555	111.23	0
0.9273	2	662	112.34	
0.9038	2	840	116.92	

$NiFe_2O_4$

PDF #54-964 Cubic (spinel)		a= 8.33673 Å λ=1.540598	
d	Int	hkl	2θ
4.811		111	18.43
2.946	29	220	30.31
2.513	100	311	35.70
2.407		222	37.33
2.084		400	43.39
1.9128		331	47.50
1.7021		422	53.82
1.6042		511	57.39
1.4738	46	440	63.02
1.4092		531	66.27
1.3186		620	71.49
1.2717		533	74.56
1.2569		622	75.59
1.2033		444	79.61
1.1142		642	87.47
1.0855		731	90.41
1.0423		800	95.30
0.9827		660	103.23
0.9626		751	106.30
0.9564		662	107.30
0.9321		840	111.46

B) Visualization of crystal alignment between NiO and Al_2O_3

Crystal models of NiO and Al_2O_3

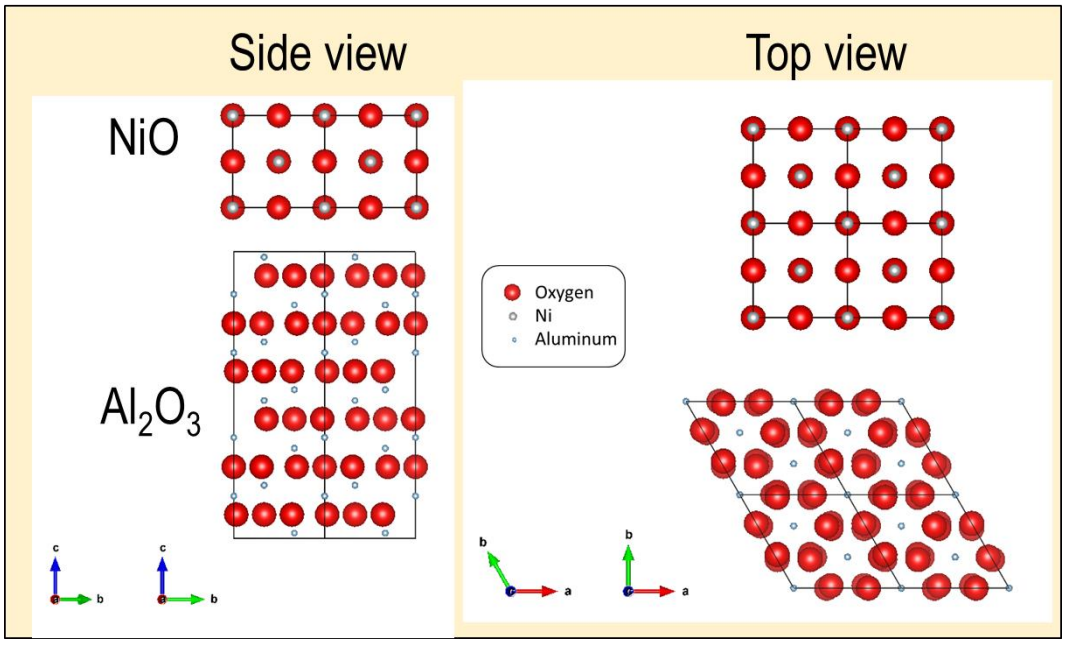

Alignment of the out of plane COR is $[111]_{NiO}||[001]_{Al2O3}$ based on the XRD θ-2θ scan.

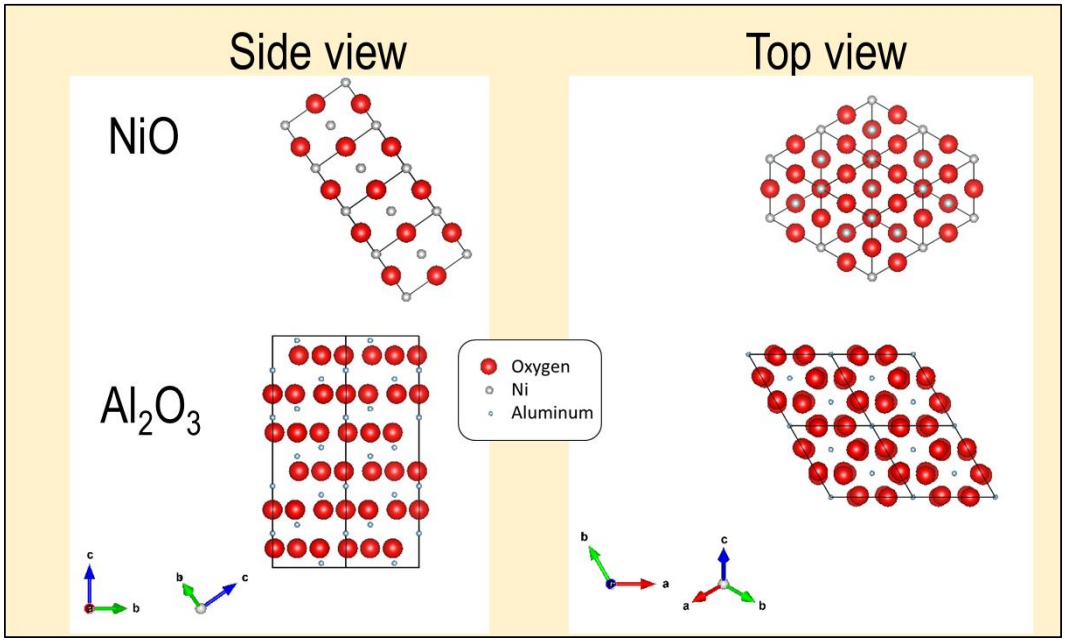

Alignment of the out of plane COR is $[116]_{NiO}||[200]_{Al2O3}$ based on the XRD φ scan.

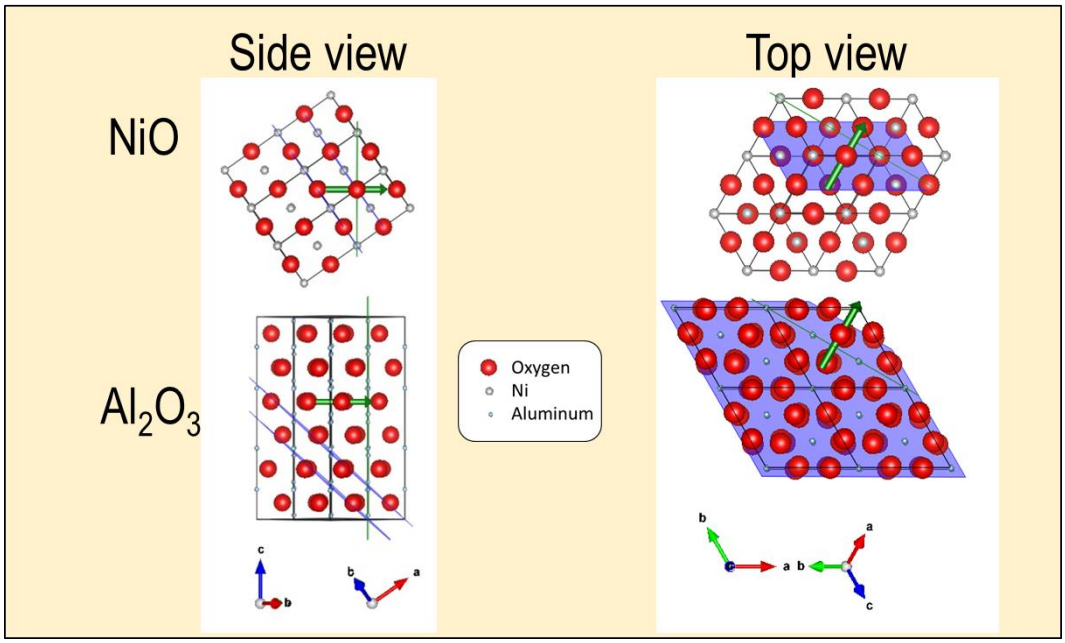

C) Energy-dispersive and wavelength-dispersive spectroscopy

The energy-dispersive spectroscopy (EDS) and the wavelength-dispersive spectroscopy (WDS) are an analytical technique used for the elemental analysis of a material. Both use the characteristic X-ray which is generated from a sample bombarded with electrons. The X-ray spectrum generated is then used to analyze the elemental constituents of the sample. The EDS used in this study is coupled with SEM, while the WDS is coupled with EPMA. In both method, a high energy electron beam is focused on the sample being studied, ejecting electrons in its core shell and leaving holes. The hole in the core shell is subsequently replaced by electrons from the outer higher-energy shell that releases energy corresponding to energy difference between the shells. The number and energy level released in the form of X-ray are measured and analyzed.

The EDS contains a detector that absorbs the energy of incoming X-ray by ionization and produce an electrical charge bias proportional to the energy of the X-ray. The energy spectrum is simultaneously obtained allowing a quick elemental characterization. The WDS commonly comprises of several analytical crystal with different lattice spacing to cover detection of various chemical elements. The characteristics X-ray is measured a single wavelength at a time which requires a longer measurement time compared to EDS. The resolution, however is better by an order. This study employed EDS for detection of cobalt and nickel in the growth of $Co_xNi_{1-x}O$ films. The composition of iron and nickel in the growth of $Ni_{1-x}Fe_xO$ was determined based on the WDS measurement.

D) Four-point probe measurement

Four-point probe measurement is employed to measure resistivity of material, bulk or thin films.[7] A distinct feature of four-point probe from the conventional two-probe is the separation of current source and voltage measurement so that wire and contact resistance is minimized and can be excluded from the measurement results. The schematic of four-probe measurement is shown in the following figure. In this study, the distance between probes, s, is 1 mm. The measurements were carried out at a point in the middle of the sample (3.3 mm from end to end).

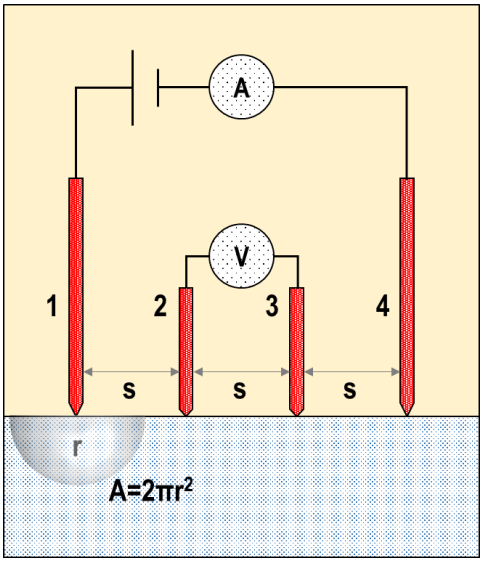

Four-point probe schematic

The expression of resistivity obtained from the four-point probe is derived as follows (D.K. Schroder, *Semiconductor Material and Device Characterization*, John Wiley & Sons, 1998). The current is assumed to flow out radially from infinitesimal probe tip. From the Ohm's law:

$$V = IR \; and \; \varepsilon = J\rho = -\frac{dV}{dr}$$

Using the current density,

$$J = \frac{I}{A} = \frac{I}{2\pi r^2}$$

Then solving for the potential distribution in terms of radius of the sphere,

$$\frac{I\rho}{2\pi r^2} = -\frac{dV}{dr}$$

$$\int_0^V dV = -\frac{I\rho}{2\pi}\int_\infty^r \frac{1}{r^2}\,dr$$

We obtain the voltage due to a single probe.

$$V = \frac{I\rho}{2\pi r}$$

Similarly, the voltage due to two probes is expressed as

$$V = \frac{I\rho}{2\pi r_1} - \frac{I\rho}{2\pi r_2}$$

Using the above equation, with s the distance between probes (1 mm), the voltage obtained in the four-point probe setting is expressed as follows.

$$V = \frac{I\rho}{2\pi s} \rightarrow \rho = 2\pi s F \frac{V}{I}$$

F is the correction factor comprises the sample thickness, the lateral dimensions, and the edge placement. For a thin film with t, the thickness, much smaller than the distance between probes, the correction factor F is:

$$F = \frac{\frac{t}{s}}{2\ln\left[\frac{\sinh\left(\frac{t}{s}\right)}{\sinh\left(\frac{t}{2s}\right)}\right]}$$

For t<<s, sinh(x)≈x,

$$F = \frac{\frac{t}{s}}{2\ln(2)}$$

The resistivity of thin film, obtained based on the current to voltage measurement in a four-point probe setup is therefore:

$$\rho = \frac{\pi}{\ln(2)} t \frac{V}{I}$$

E) Hall effect

Hall Effect is the voltage difference occurred in a conductor material transverse to an electric current in the conductor and a magnetic field perpendicular to the current. For semiconducting material, this effect can be used to indicate semiconductor type, density, and mobility of carriers.

The Hall Effect measurement consists of the following steps.

1. Carriers drift due to applied current

The carrier drift velocity is given by

$$v = \frac{I}{n.A.q}$$

$I: current\ (A), n: carrier\ density (m^{-3})$
$A: Cross\ sectional\ Area\ (m^2)$
$v: carrier\ drift\ velocity \left(\frac{m}{s}\right)$
$q: carrier\ particle\ charge (C)$

2. Carriers are accumulated to one side of the slab due to magnetic field

When a magnetic field perpendicular to the current is applied, carriers are accumulated to one side of the slab due to the Lorentz force.

$$\overrightarrow{F_L} = q.\vec{v}\ x\ \vec{B}$$

$\vec{B}: magnetic\ flux\ density\ ({}^{Wb}/_{m^2} = Tesla)$

Substituting v,

$$\overrightarrow{F_L} = \frac{\vec{I}}{n.A}\ x\ \vec{B}$$

3. Hall voltage is measured

The accumulated electrons generate an electric field whose force opposes the Lorentz force equally.

$$F_C = F_L$$

$$\varepsilon . q = \frac{I . B}{n . A} \rightarrow \varepsilon = \frac{I . B}{n . A . q}$$

ε: $Electric\ field\ (N/C)$

The Hall coefficient R_H is defined as

$$R_H = \frac{1}{n . q}$$

Substituting R_H, ε becomes

$$\varepsilon = \frac{R_H . I . B}{A}$$

The measured voltage different is the Hall voltage.

$$V_H = w . \varepsilon$$

When V_H positive, the material is p type semiconductor, and vice versa when $V_H$negative, the material is n type semiconductor.

Substituting ε,

$$V_H = \frac{w . I . B}{n . q . A}$$

With the surface A constructed of the width and depth, $A = w . d$,

$$V_H = \frac{I . B}{n . d . q}$$

And with $n_s$being carrier sheet density $n_s = n.d(m^{-2})$,

$$n_s = \frac{I.B}{V_H.q}$$

$$R_H = \frac{V_H.t}{I.B}$$

The Van der Pauw technique is commonly employed along with the Hall Effect to achieve more accurate result. In this configuration, four electrodes are placed in the corners of a square shaped sample. The technique uses reciprocal and reversed polarity theorem to accurately measure material's resistivity. It lies on Van der Pauw formula where

$$e^{-\pi R_{12,34}/R_s} + e^{-\pi R_{23,41}/R_s} = 1 \quad | \quad R_s: Sheet\ Resistance$$

By solving the formula for R_s, the sheet resistance of material can be obtained.

The following notation is used in this study. I_{ab} represents a positive current from contact a to b, V_{cd} represents a DC voltage between contact c and d, and $R_{ab,cd} = \frac{V_{cd}}{I_{ab}}$. The Van der Pauw technique consists of the following steps (M.A. Tupta, *High Resistivity and Hall Voltage of Semiconducting Materials*, Keithley Instruments, Inc., 2005).

1. Vertical Resistance, R_{vert}
    a. Flow current from 1 to 2 → I_{12}, measure the voltage difference V_{34}, then calculate the resistance $R_{12,34}$
    b. Flow current from 3 to 4 → I_{34}, measure the voltage difference V_{12}, then calculate the resistance $R_{34,12}$

$$R_{vert} = \frac{R_{12,34} + R_{34,12}}{2}$$

2. Horizontal Resistance, R_{hor} (reciprocal measurement)

    a. Flow current from 2 to 3 → I_{23}, measure the voltage difference V_{41}, then calculate the resistance $R_{23,41}$

    b. Flow current from 4 to 1 → I_{41}, measure the voltage difference V_{23}, then calculate the resistance $R_{41,23}$

$$R_{hor} = \frac{R_{23,41} + R_{41,23}}{2}$$

So that the formula becomes

$$e^{-\pi R_{vert}/R_s} + e^{-\pi R_{hor}/R_s} = 1$$

Reversed bias measurement is carried out to obtain a more accurate result. This is conducted by inversing the current flowed into the contacts. In short, one obtains

$$R_{vert} = \frac{R_{12,34} + R_{21,43} + R_{34,12} + R_{43,21}}{4}$$

And

$$R_{hor} = \frac{R_{23,41} + R_{32,14} + R_{41,23} + R_{14,32}}{4}$$

Finally, the formula to obtain sheet resistance is

$$e^{-\pi R_{vert}/R_s} + e^{-\pi R_{hor}/R_s} = 1$$

$$R_s = \frac{\pi}{\ln 2} \frac{(R_{vert} + R_{hor})}{2} f$$

$$\rho = R_s / d$$

f is a correction factor which is a function of $R = \frac{R_{vert}}{R_{hor}}$ as given in the following literature (L.J. van der PAUW, Philips Technical Review **20**, 220, 1958).

The principle of the Van der Pauw technique is applied in the Hall measurement. The current and magnetic field are reversed in the following manner.

1. Positive magnetic field (positive z)
   a. Flow current from 2 to 4 → I_{24}, measure the voltage difference $V_{13,P}$, reciprocally
   b. Flow current from 1 to 3 → I_{13}, measure the voltage difference $V_{42,P}$

   Then by inversing the current,
   c. Flow current from 4 to 2 → I_{42}, measure the voltage difference $V_{31,P}$, reciprocally
   d. Flow current from 3 to 1 → I_{31}, measure the voltage difference $V_{24,P}$

2. Negative magnetic field (negative z)
   a. Flow current from 2 to 4 → I_{24}, measure the voltage difference $V_{13,N}$, reciprocally
   b. Flow current from 1 to 3 → I_{13}, measure the voltage difference $V_{42,N}$
   c. Flow current from 4 to 2 → I_{42}, measure the voltage difference $V_{31,N}$, reciprocally
   d. Flow current from 3 to 1 → I_{31}, measure the voltage difference $V_{24,N}$

3. Analysis to obtain resistivity, carrier concentration, and mobility

   By using $V_{13} = V_{13,P} - V_{13,N}$, $V_{24} = V_{24,P} - V_{24,N}$, $V_{31} = V_{31,P} - V_{31,N}$, and $V_{42} = V_{42,P} - V_{42,N}$, the Hall voltage is obtained as follows.

$$V_H = \frac{V_{13} + V_{24} + V_{31} + V_{42}}{8}$$

Since $V_H = \frac{I.B}{n_s.q}$, the sheet density is

$$n_s = \frac{I.B}{|V_H|.q}$$

The resistivity of semiconducting material is given by

$$\rho = \frac{1}{q(n\mu_n + p\mu_p)} \qquad \mu_p, \mu_n: hole\ and\ electron\ mobility\ \left(m^2/_{V.s}\right)$$

For doped semiconductors, only the majority carrier is put into consideration

$$\rho = \frac{1}{qn\mu_n}$$

Noting that sheet resistance $R_s = \frac{\rho}{d}$ and sheet density $n_s = n.d$

$$R_s = \frac{1}{qn_s\mu_n}$$

Solving for mobility,

$$\mu_n = \frac{1}{qR_sn_s}$$

F) Optical transmittance

Optical transmittance measurement is carried out to probe the semiconductor's band-gap as well as material transparency. Semiconductors are transparent to photons whose energies are below their band-gaps and absorbent to photons whose energies are higher than their band-gaps. Photons with higher energy than band-gap are strong enough to excite electrons from the valence band to the conduction band. Therefore, the transmittance spectra may indicate the band-gap energy of semiconductors. In the experiments, baseline measurement was performed on the substrate, so that substrate effect is minimized.

Transmittance T is defined as

$$T(\lambda) = \frac{I_T(\lambda)}{I_O(\lambda)}$$

I_T : Transmitted
I_O : incident

An example of transmittance measurement is shown in the following figure.

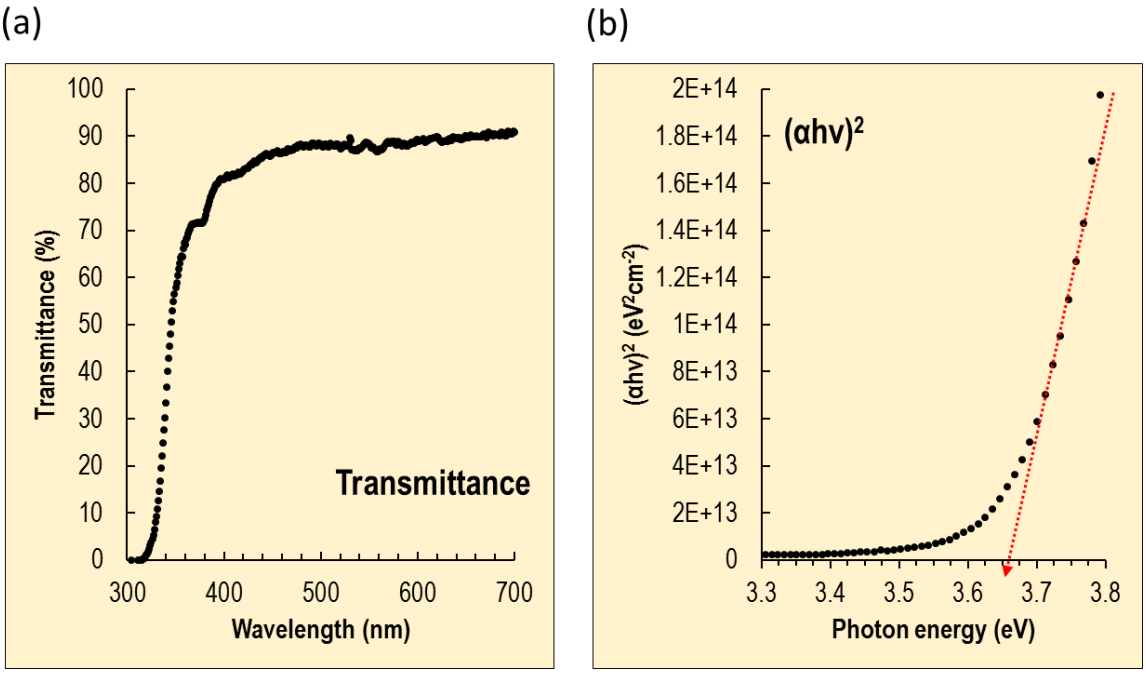

Example of (a) transmittance measurement and (b) bandgap estimation

For bandgap estimation, the transmittance data was normalized at the transparent region in order to neglect Fresnel reflections. Absorption coefficient α can be determined from transmittance according to the following relation

$$\alpha(\lambda) = -\frac{1}{d}\ln(T(\lambda))$$

Absorption coefficient is related to energy-gap according to the classical relation for near edge optical absorption in semiconductor.

$$\alpha h\nu = A\left(h\nu - E_g\right)^n$$

Where α is the absorption coefficient, h is Planck's constant, ν is frequency, E_g is the semiconductor band gap, A is a constant, and n is a constant that determine type of transition. n equal to $\frac{1}{2}$ for direct allowed, n equal to $\frac{3}{2}$ for direct forbidden, n equal to 2 for indirect allowed, n equal to 3 for indirect forbidden. Extrapolation of these curves to photon energy axis gives estimation for the band gaps (J. Tauc, et. al. Physica Status Solidi (b) **15**, 627, 1966). An example of a direct bandgap estimation is shown in the following figure.

G) Raman Spectroscopy

Raman spectroscopy uses inelastic light scattering from monochromatic source, usually a laser to probe molecular vibrational modes. When a laser is incident on a material, it may be reflected, absorbed, or scattered in some manner. The scattering radiation is the one used in Raman. The scattered radiation includes not only those with same wavelength as incident light (Rayleigh scattering) but also those with higher (Anti stokes Raman scattering) or lower (Stokes Raman scattering) wavelength. The scattering with change of wavelength is the one specifically probe in Raman Spectroscopy. The following figure (Wikipedia) illustrates the energy level and kinds of scattering. Scattering with change in wavelength is only a small portion of total scattered light which is approximately $1x10^{-7}$ of the scattered light. However, this provides chemical and structural information of the material.

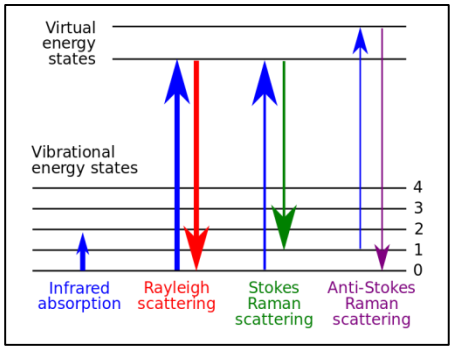

Energy level diagram and scattering modes

H) Thickness variation

The thickness of samples used in the chapters in this study was obtained by SEM observations of the film's cross-section. The aim of thickness measurement is to estimate the thickness of the center area of the sample which are used in the characterization. First, the samples are cut, then three points of the front, middle, and back sides (with respect to the flow of materials) are measured. These three points lie within ~0.5 cm of the samples from the midpoint parallel to the gas flow direction. The values for NiO samples are shown in the following table.

Thickness values based on observation by SEM

Sample	Point 1 (µm)	Point 2 (µm)	Point 3 (µm)	Average thickness (µm)	Standard deviation (µm)
O_2/Ni ratio 0.5k	1.35	0.84	0.53	0.9	0.41
O_2/Ni ratio 1k	1.67	1.18	1.13	1.3	0.29
O_2/Ni ratio 2k	0.68	1.99	1.89	1.5	0.73
O_2/Ni ratio 5k	0.96	0.90	0.8	0.9	0.08
On MgO (100) 300 °C	0.51	0.47	0.27	0.4	0.13
On MgO (100) 400 °C	2.16	1.4	1.24	1.6	0.49
On MgO (100) 500 °C	1.11	0.77	0.71	0.8	0.22
On MgO (100) 600 °C	0.30	0.22	0.14	0.2	0.08
On MgO (111) 300 °C	0.52	0.38	0.37	0.4	0.08
On MgO (111) 400 °C	1.43	1.41	1.33	1.4	0.05
On MgO (111) 500 °C	0.71	0.68	0.63	0.7	0.04
On MgO (111) 600 °C	0.38	0.18	0.05	0.2	0.17
On Al_2O_3 300 °C	0.17	0.07	NA	0.1	0.07
On Al_2O_3 400 °C	1.28	1.18	1.11	1.2	0.09
On Al_2O_3 500 °C	0.66	0.66	0.65	0.7	0.01
On Al_2O_3 600 °C	0.36	0.30	0.21	0.3	0.08

Typical cross section SEM images are shown below.

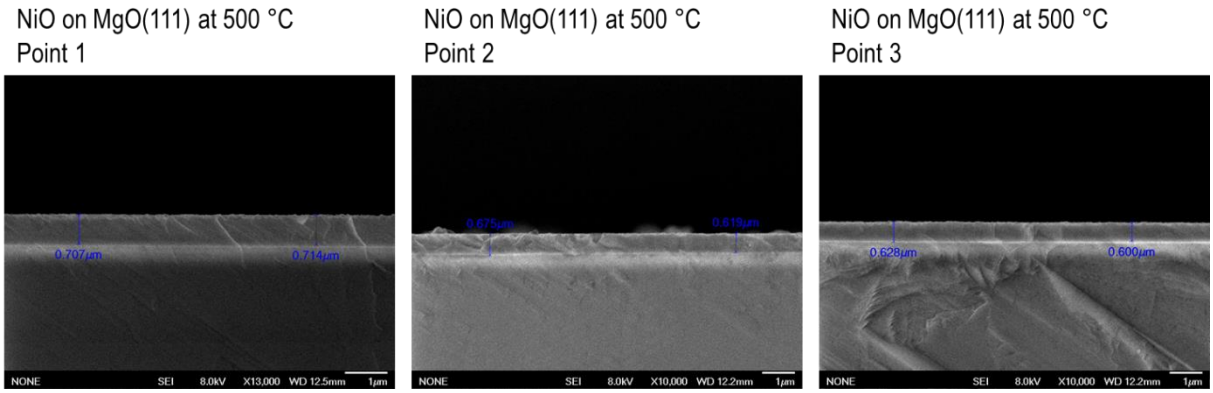

Cross section SEM images of NiO sample grown on MgO(111) substrate at 500 C